Carnegie Mellon University
MELLON COLLEGE OF SCIENCE

THESIS

SUBMITTED IN PARTIAL FULFILLMENT OF THE REQUIREMENTS
FOR THE DEGREE OF

DOCTOR OF PHILOSOPHY IN THE FIELD OF PHYSICS

TITLE: "Towards a magnetic proximity effect in a van der Waals heterostructure."

PRESENTED BY: Devashish Gopalan

ACCEPTED BY THE DEPARTMENT OF PHYSICS

Benjamin Hunt	8/21/19
BENJAMIN HUNT, CHAIR PROFESSOR	DATE

Scott Dodelson	8/21/19
SCOTT DODELSON, DEPT HEAD	DATE

APPROVED BY THE COLLEGE COUNCIL

Rebecca Doerge	9/04/19
REBECCA DOERGE, DEAN	DATE

Towards a magnetic proximity effect in a van der Waals heterostructure

by

Devashish P. Gopalan

Submitted in partial fulfillment of the
requirements for the degree of
Doctor of Philosophy
at
Carnegie Mellon University
Department of Physics
Pittsburgh, Pennsylvania

Advised by Professor Benjamin M. Hunt

August 28, 2019

Abstract

The advent of new two-dimensional materials, and the ability to create van der Waals heterostructures has further intensified research interest in graphene. At the heart of these heterostructures is the proximity effect, where one material synergistically inherits the properties of the material adjacent to it. The capabilities of graphene can thus be greatly enhanced by tailoring in new properties whilst preserving its excellent implicit properties. Of considerable interest is the creation of a long range magnetic order in graphene by means of a magnetic proximity effect from an adjacent two-dimensional magnet. Such a system has industrial applications in the field of low power logic and memory devices. It is also of curiosity to scientists as it harbours novel topological states, and could help understand the manifestation of phenomena such as magnetism in two dimensions. Here we fabricate devices made out of heterostructures of graphene and two-dimensional magnets. We characterize the electronic and magnetic properties of such devices using electronic transport, capacitance and optics. The majority of efforts have been directed towards creating clean interfaces, and preserving the magnetic materials, which are extremely chemically sensitive to ambient conditions. We demonstrate the presence of interfacial physics in these devices that lead to the enhancement in the magnetic order of the two-dimensional magnet.

Contents

List of Tables

List of Figures

Chapter 1

Van der Waals materials and heterostructures

One of the greatest hallmarks of physics has been our ability to create desired physical properties in systems. The world continues to operate precisely because of our ability to tune material characteristics, elicit the desired response, and harness those properties to our advantage. The entire semiconductor industry, and the revolution of computers was made possible due to scientists being able to precisely control the transport of electrons. Very often, completely distinct regimes of physical properties are completely inter-dependent, and combine together for important applications. For example, magnetic resonance imaging scanners in hospitals utilize magnetic fields as large as 7 Tesla. This large amount of magnetism is achieved via coils made out of superconducting wires through which a large current is flown. These advances in superconductivity themselves have been dependent on progress made in the field of low temperature physics.

A relatively convenient technique to drastically modify the physical properties is to alter the dimensionality of the system. "Van der Waals" (vdW) materials are one such system. A vdW material possesses a layered structure, with each layer weakly bonded to the adjacent one with a vdW attractive force. Thus, vdW materials can be cleaved down in thickness, until we are left with a sheet that is literally one atom thin. The confinement of electrons to a two dimensional (2D) plane leads to novel, emergent physical phenomena.

The first, and the most famed of vdW materials is graphene, a single atom thin sheet of carbon atoms in a hexagonal arrangement. Graphene is derived by cleaving down graphite (pencil lead), and has an astonishing range of superlative electrical, chemical, and mechanical properties. For example, electrons in graphene behave as massless particles, free to conduct electricity due to the absence of a bandgap. The natural confinement of electrons to a 2D plane gives rise to the quantum Hall effect (QHE) under the application of an out of plane magnetic field, which prior to graphene's discovery required engineering of quantum wells to create a 2D electron

gas.

Today, vdW materials harboring all breadths of physics exist. This makes it possible to study most physical phenomena in the 2D limit. Additionally, we can fabricate vertical vdW heterostructures of different 2D materials. These vdW heterostructures allow us to not only study interfacial physics between two materials, but also combine materials in a synergistic fashion.

In this thesis, chapter 1 is used to motivate the field of vdW materials, and their heterostructures. Chapter 2 pertains to a project where we grew large area vdW heterostructures [1]. In chapter 3 we leverage multi-dimensionality and study the electronic properties of a three dimensional (3D) superstructure grown out of 2D "fuzzy" graphene along a one dimensional (1D) Si nanowire template[2]. In chapter 4 we motivate the need for creating a vdW heterostructure made out of graphene and 2D magnets. This project is the bulk of the thesis, and experimental results are discussed in chapter 5 before concluding the thesis in chapter 6. The author of this thesis was also involved in the studies of 2D superconductivity. While we do not discuss that project in great detail here, we refer the interested reader to ref. [3].

We begin here by briefly reviewing the history of graphene and other 2D materials. We discuss some of the major results from 2D materials that are semiconductors, superconductors, and magnets. At the end of the chapter, we will motivate the creation of vdW heterostructures.

1.1 The history of graphene

The history of graphene dates back as far as 1859 when a British chemist, Sir Benjamin Brodie heated graphite in mixtures of concentrated nitric and sulphuric acids[4]. He termed the resultant product "graphic acid", which upon the addition of water in some cases would create a colloidal solution. He identified the obtained compounds as having chemical formulae of $C_{11}H_4O_5$, $C_{22}H_2O_4$, $C_{66}H_4O_{11}$, and he termed the building block of these compounds the name "graphon", a new form of carbon, along with hydrogen and oxygen atoms. It is now believed that what Brodie had managed to synthesize were crystals of graphite oxide[5]. That is, a structure similar to graphite but with the layered planes containing hydroxyl and epoxide functional groups in addition to carbon atoms. (Fig. 1.1b)

It would be over a century before further light on Brodie's work would be shed. In 1962, Ulrich Hofmann and Hans-Peter Boehm looked at droplets of graphite-oxide under a transmission electron microscope (TEM) and identified some of the flakes as being monolayers of graphene-oxide (Fig. 1.1b). The word "graphene" would not be coined until 1986 by a team led by Boehm [7]

On the theoretical side, P. R. Wallace calculated in 1947 the band structure of "a monolayer of graphite", simply to build towards calculating the band structure of bulk graphite. Beyond that, graphene was simply a toy model that theorists were

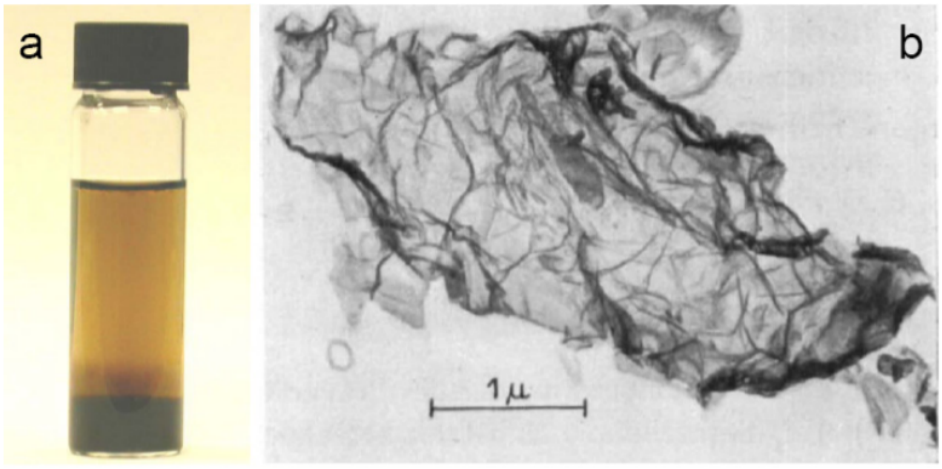

Figure 1.1: The first study of graphite oxide
(a) Solution of graphite oxide similar to one that Brodie may have observed. (b) TEM image of ultra-thin graphite oxide flakes as observed by Hofmann and Boehm in 1962[6]. From [5]

interested in due to parallels between graphene and (2+1)- dimensional quantum electrodynamics. It was widely believed that graphene as a material couldn't possibly exist in a stable form, due to the Mermin-Wagner theorem[8, 9]. The theorem argued that in a perfectly ordered crystal in two dimensions, thermal fluctuations would be infinitely large and destroy any form of long range order. The conditions required by the Mermin-Wagner theorem however, are rather strict and quite easy to circumvent. For example, in graphene, the slightest of ripples in the structure of suspended graphene are sufficient to suppress the thermal fluctuations, and make graphene a stable "nearly perfect" 2D crystal[10].

The major experimental breakthrough in graphene research came in 2004, when using the scotch tape exfoliation technique, Andre Geim and Konstantin Novoselov succeeded in isolating and characterizing atomically thin films of carbon atoms[11]. Furthermore, they were able to fabricate electronic devices out of these isolated few layer graphene flakes and characterize their electrical properties. The technique would next be extended to single layer graphene[**?** 12]. The graphene age had begun.

1.2 Two dimensional materials

1.2.1 Graphene

Graphene is a single atom thin sheet of carbon atoms arranged in a honeycomb lattice. The electrons in graphene as a result, are confined purely to a two dimensional plane unlike in bulk 3D materials. The band structure of graphene reveals a linear dispersion

relation with the conduction and valence bands touching at the high symmetry ***K*** and ***K'*** points in the Brillouin zone. In contrast, a traditional bulk semiconductor has a quadratic dispersion relation, with a non-zero band gap between the conduction and valence bands.

Ambipolar transport in graphene

Geim and Novoselov's original paper demonstrated ambipolar transport characteristics in graphene[11]. Their graphene device (like many others that would follow) was fabricated on a 300 nm thick SiO_2 on doped Si substrate (SiO_2/Si). The combination of an insulating oxide along with a doped, conducting Si substrate allows one to use a capacitive electric field effect to tune graphene's carrier density. By the application of a large positive (negative) gate voltage to the Si, the Fermi level can be tuned such that it lies firmly inside the conduction (valence) band, corresponding to a large number of electrons (holes) in the graphene. Roughly, the corresponding 3D values of electron and hole densities that can be achieved this way are $\sim \pm 10^{21} cm^{-3}$. This is quite incredible. A single graphene device can be tuned to behave similar to highly n and p doped Silicon, and anything in between. Indeed, by adjusting the gate voltage such that the Fermi level lies at the charge neutrality point (CNP), i.e. the point at which the conduction and valance bands touch, Geim and Novoselov demonstrated a nearly 100 fold increase the device's resistance[11].

To summarize, the carrier density is a parameter that can:
(1) Be easily tuned in vdW materials by electrostatic gating
(2) Greatly affect the underlying properties of the 2D material

Both of these points were demonstrated in graphene right at the onset.

1.2.2 Hexagonal boron nitride

Hexagonal boron nitride (h-BN) possesses a structure similar to graphene with weakly vdW bonded atomic sheets with atoms arranged in a honeycomb lattice within a sheet. Unlike graphene which has identical C atoms, h-BN has distinct B and N atoms in the A and B (or vice versa) sublattices respectively. An immediate result of this distinction is that h-BN is a wide band gap insulator with a band gap of ~ 6 eV.

Due to its atomic flatness, inertness and insulating behavior, h-BN is an ideal substrate material for graphene [13]. A comparison of the surface of a graphene device on h-BN (g-BN) vs SiO_2/Si (g-Si) was carried out by J. Xue et al.[14]. They demonstrate (Fig. 1.2 a) through atomic force microscopy (AFM) that the surface of the g-BN device (rms roughness $\sim$ 30 pm) was over 7 times smoother than the g-Si device ($\sim$ 225 pm). Additionally, they map the surface potential by tracking the spatial variation of the Dirac point energy in the two devices. Due to the roughness of the SiO_2/Si, there exist charge traps in the g-Si device, which lead to surface potential fluctuations of the order of $\pm 100 meV$ (Fig. 1.2 b). By comparison, the atomically

flat h-BN surface gives rise to a much smoother surface potential profile on the g-BN device (Fig. 1.2 c).

Due to the roughness, charge traps and surface potential fluctuations, the mobilities in graphene on SiO_2/Si devices are usually limited to $\sim$ 10,000 cm^2/V.s at 2 K. Mobilities of graphene on h-BN devices on the other hand, are usually greater than 100,000 cm^2/V.s.

Boron nitride is also an effective encapsulating material (sandwiching an air sensitive material between 2 flakes of h-BN), a uniform tunnelling barrier due to its atomic flatness and an excellent gate dielectric material with its dielectric constant of $\kappa \approx 4$.

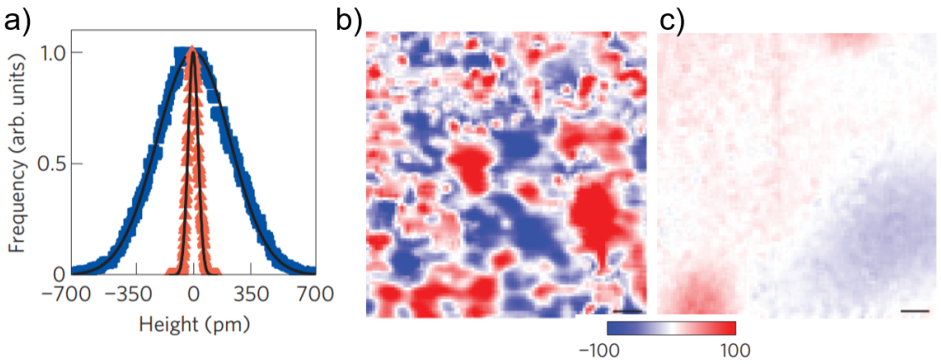

Figure 1.2: Surface potential mapping of graphene devices on Si and h-BN (a) Surface roughness from AFM of a graphene device on SiO_2/Si (blue) vs h-BN (orange). Surface potential of graphene device on (b) SiO_2/Si and (c) h-BN. Scale bars are 10 nm. From [14].

1.2.3 2D superconductors

Transition metal dichalcogenides (TMDs) are materials with the crystal formula MX_2, where M is a transition metal atom, and X is a halogen atom[15]. Similar to graphene and h-BN, TMDs possess a layered vdW structure. Each "monolayer" is actually three atomic layers thick corresponding to X-M-X planes respectively. Metallic TMDs, such as 2H-$NbSe_2$ and 2H-TaS_2 are known instrinsic superconductors in their bulk 3D form[16, 17]. Here the prefix 2H refers to the stacking arrangement in which the transition metal atoms in successive monolayers lie on top of one another.

Upon exfoliation, the critical temperature (T_c) of $NbSe_2$ reduces from 7 K in bulk, to 3 K in the monolayer limit [16, 17, 3]. In TaS_2, the opposite trend in observed. While bulk TaS_2 has a T_c of 0.5 K, monolayer TaS_2 has an elevated T_c of 3 K[3, 18]. The layer dependence of T_c and the reversal of the trend in the two materials are intriguing. The trend in $NbSe_2$ could be explained by suppressing Cooper pair formation due to the reduction of interlayer interactions, and the increased significance of substrate interactions as the material is thinned down. In TaS_2, the repulsive Coulomb

interaction associated with the Anderson-Morel pseudo-potential is enhanced due to the 5d orbitals associated with Ta[18]. This particular interaction is quite insignificant in $NbSe_2$ which could explain the opposite trends in T_c. Another explanation for the deviation in TaS_2 could be qualitatively explained by the competing charge density wave state that exists in bulk form, and weakens as TaS_2 is thinned down[18].

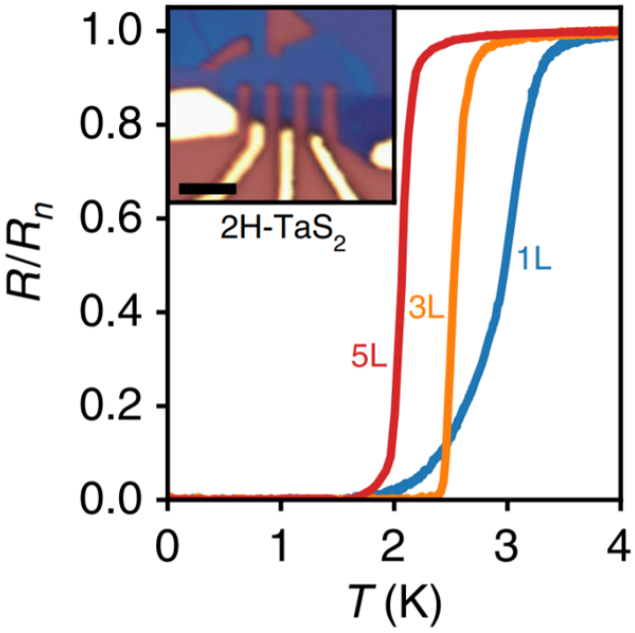

Figure 1.3: Layer dependent superconductivity in TaS_2
R-T profiles for three different thicknesses of 2H-TaS_2. Inset is an optical image of a representative device. Scale bar is $4\mu m$ From [3]

Another interesting phenomenon common to these 2D superconductors is the robustness of superconductivity under magnetic fields oriented parallel to the plane of the material ($H^{||}$)[16, 17, 3]. Due to the 2D nature of these layers, the electron momenta **k** are in the in-plane direction. Additionally, crystal symmetries (out-of-plane mirror symmetry and in-plane inversion symmetry) give rise to an in-plane crystal field **E**. Lastly, these materials possess a significant spin orbit interaction due to the presence of the heavy transition metal atoms. The combination of these factors results in a large spin orbit field in the out-of-plane direction $\mathbf{H_{so}} = \lambda_{\mathbf{so}} \cdot (\mathbf{E} \times \mathbf{k})$. The spins of the two electrons that form a Cooper pair are strongly pinned to the up and down directions due to this large spin orbit field.

Under $H^{||}$, the mechanism for destruction of superconductivity is Pauli paramagnetism at a critical field H_P. Briefly, $H^{||}$ increases the energy of the system by a Zeeman effect $\propto 2\mu_B H^{||}$ where μ_B is the Bohr magneton. At $H^{||} = H_P$, this Zeeman energy exceeds the superconducting gap and destroys superconductivity. In "Ising" superconductors such as $NbSe_2$ and TaS_2 however, the critical field $H^{||}_{c2}$ can be sig-

nificantly larger than H_P because of the large spin orbit field pinning the spins in the out-of-plane direction. Indeed, we found that $H_{c2}^{||}$ for monolayer TaS_2 and $NbSe_2$ were 65.6 T and 43.6 T respectively, in contrast with $H_P = 5.5$ T for both[3].

While the author of this thesis was a part of the team that studied these 2D superconductors, we will not discuss this subject any further in this thesis. We refer the reader to ref. [3] for further details on this study. It is quite clear though that vdW materials make it possible to study conventional 3D physical phenomena in the 2D limit. Additionally, the thickness of the material is a parameter that we can easily control to tune the properties of the system, such as T_C or $H_{c2}^{||}$ as demonstrated here.

1.2.4 2D magnets

Whilst a relatively new field, materials with ferromagnetic order down to the monolayer limit have now been demonstrated. Theoretically, the Mermin-Wagner theorem dictates that diverging thermal fluctuations should destroy any long range order in isotropic, two-dimensional ferromagnets[9]. Similar to the existence of graphene, an easy work around exists. If there exists a magnetic anisotropy, these thermal fluctuations can be suppressed[19].

Two 2D magnetic systems were simultaneously reported in 2017: $Cr_2Ge_2Te_6$ and CrI_3 [19, 20].$Cr_2Ge_2Te_6$ is a transition metal trichalcogenide (TMTC) where each "monolayer" is 5 atomic layers thick (Te-Ge-Cr-Ge-Te). Cr atoms are arranged in-plane in a honeycomb lattice, with the Ge_2Te_6 ligands oriented perpendicular to the Cr plane at the centres of the hexagons (Fig. 1.4).CrI_3 is a trihalide, with Cr atoms arranged in a honeycomb lattice in-plane, and octahedrally coordinated to I atoms (Fig. 1.5a). A monolayer of CrI_3 comprises three atomic planes (I-Cr-I) as seen in Fig. 1.5b.

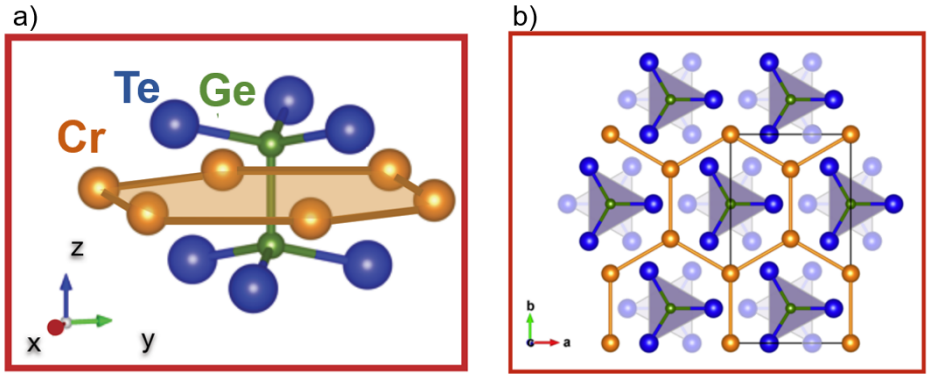

Figure 1.4: Crystal structure of a monolayer of $Cr_2Ge_2Te_6$
(a) Side view (b) Top view of a monolayer of $Cr_2Ge_2Te_6$. Adapted from [21].

Both the studies on $Cr_2Ge_2Te_6$ and CrI_3were conducted using an optical characterization technique called Kerr microscopy, which utilizes the magneto-optic Kerr

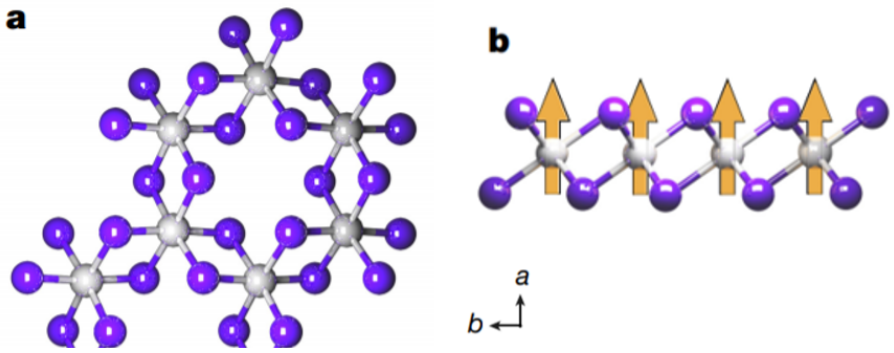

Figure 1.5: Crystal structure of a monolayer of CrI_3
(a) Top view and (b) Side view of a CrI_3 monolayer. From [20]

effect (MOKE). Briefly, linearly polarized light was shone on the sample's surface at a small angle of incidence. The polarization of light reflected from the magnetic surface is different, and was measured. The difference in the polarization between the reflected and incident light termed Kerr rotation (θ_K) is proportional to the sample's magnetization to first order. With a sensitivity of 100 , both groups were able to measure the magnetization of $Cr_2Ge_2Te_6$ and CrI_3 down to the bilayer and monolayer limit respectively. Those results are discussed briefly here.

Bulk $Cr_2Ge_2Te_6$ has a Curie temperature (the critical temperature at which a material spontaneously magnetizes) T_c= 68 K. In bilayer $Cr_2Ge_2Te_6$ $T_c$was lowered to $\sim$ 30 K. Similarly, bulk CrI_3 has a T_c= 61 K, which reduces to 45 K in the monolayer limit[20, 22]. The observations reported by B. Huang et al., are illustrated in Fig. 1.6.

Fig. 1.6a shows that the Kerr rotation for monolayer CrI_3 has a hysteretic behavior as the external magnetic field is varied. This is a tell-tale signature of ferromagnetism in the 2D monolayer limit. Interestingly, the Kerr signal vanishes to zero over a broad range of magnetic field values for bilayer CrI_3, a signature that bilayer CrI_3 is an anti-ferromagnet(Fig. 1.6b). Trilayer CrI_3 reverts back to a ferromagnet (Fig. 1.6c). These observations of B. Huang et al., indicate that while each layer of CrI_3 is ferromagnetically polarized, the adjacent layers themselves have an anti-ferromagnetic coupling between them. That is, in bilayer CrI_3, the top layer is in the ($\uparrow\uparrow\uparrow$) whilst the bottom CrI_3 layer is in the ($\downarrow\downarrow\downarrow$) configuration or vice versa[20, 23].

In conclusion, magnetism is yet another example of a physical phenomenon which exists in 2D. By controlling the layer number of the material, we can control the critical temperature, as well as the magnetic ground state of the system. Beyond $Cr_2Ge_2Te_6$ and CrI_3, there is now a broad family of 2D magnets with different magnetic ground states (ferromagnets, anti-ferromagnets, helical spin texture, spin glass) and electrical properties (metallic and insulating)[24]. In this thesis, we will primarily be concerned with three 2D magnets: CrI_3, $CrSiTe_3$, and α-$RuCl_3$. CrI_3, whose

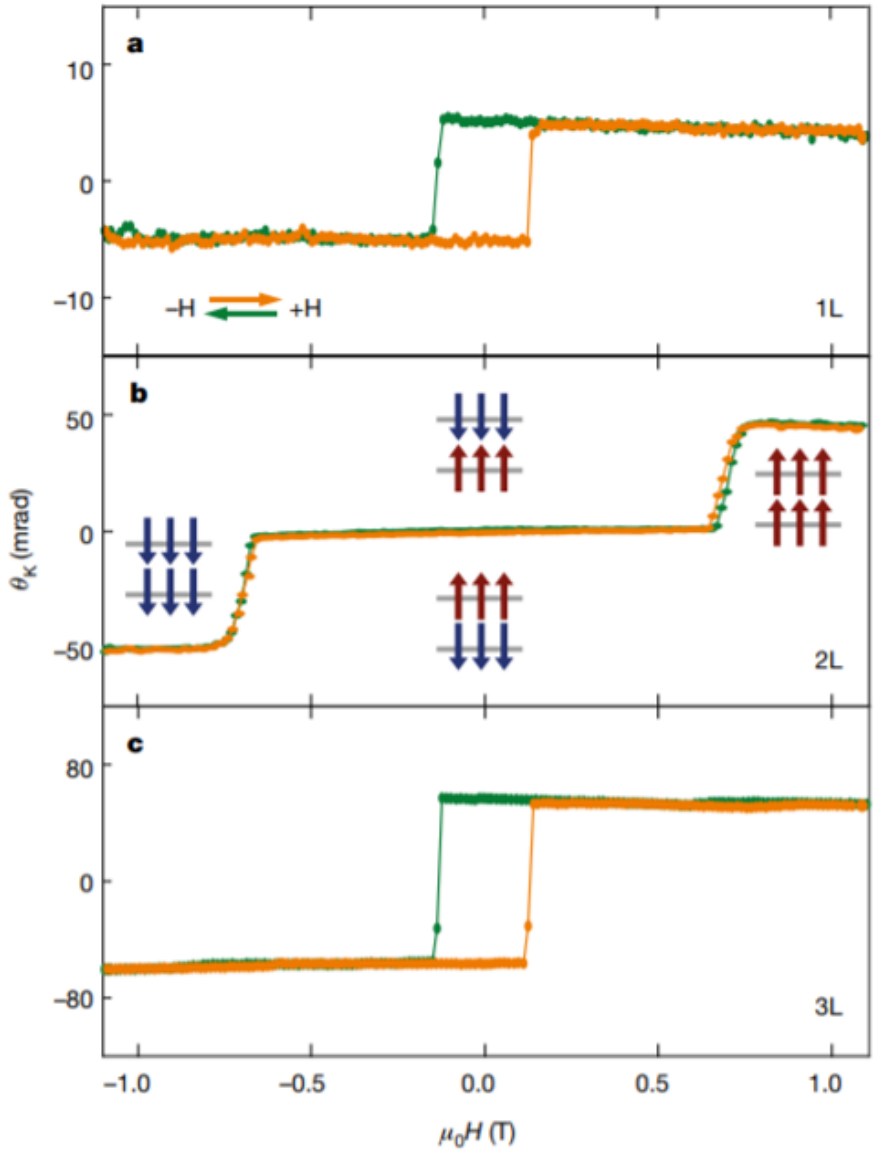

Figure 1.6: Ferromagnetism in one, two, three layers of CrI_3
Kerr rotation angle versus external magnetic field for (a) Monolayer (b) Bilayer (c) Trilayer CrI_3. Temperature is 5 K. Figure from [20]

magnetic properties were just discussed, is electrically insulating. $CrSiTe_3$ is closely related to $Cr_2Ge_2Te_6$ (or $CrGeTe_3$) and is another ferromagnetic insulator with a bulk $T_c$of 33 K and an out-of-plane easy axis[25, 26]. α-$RuCl_3$(henceforth referred to as $RuCl_3$) is electrically insulating, but exhibits multiple phases magnetically. Depending on the stacking order, $RuCl_3$ undergoes an anti-ferromagnetic transition at a Neel temperature $T_N = 14$ K (ABC stacking) or 7 K (AB stacking). Above T_N, $RuCl_3$ is

a Kitaev spin liquid, i.e. the spins have an Ising interaction that depends on the direction of the chemical bond connecting them[27].

1.3 Van der Waals heterostructures

In his visionary 1959 lecture "There's plenty of room at the bottom", Richard Feynman poses the question,

"*What could we do with layered structures with just the right layers?*"

Van der Waals heterostructures are the system that come the closest to achieving this possibility. We have already seen the broad range of physical properties that vdW materials harbor. By mixing and matching distinct materials in a chosen desired sequence, we can create superstructures which have synergistic properties. For example, two monolayers of graphene separated by a 3-4 layer thick h-BN flake give rise to a novel "beyond CMOS" transistor device with highly non-linear I-V characteristics. This device is discussed in section 1.3.3[28]. Similarly, a solar cell can be created by combining semiconducting WSe_2 and MoS_2[29].

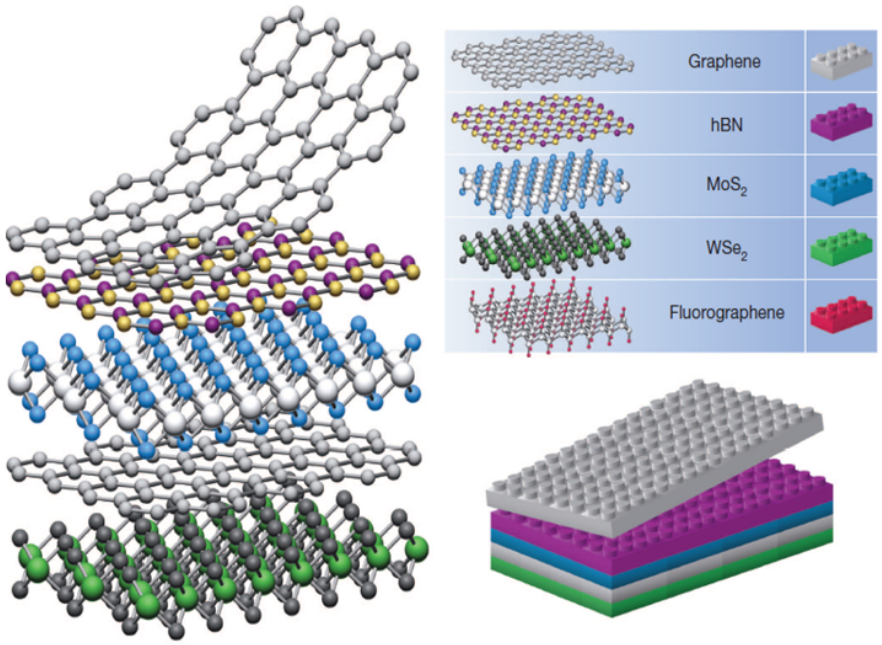

Figure 1.7: Van der Waals heterostructures
Stacking vdW heterostructures is similar to stacking different lego blocks layer by layer. However, vdW stacking allows for lattice mismatches and non zero twist angles between successive material layers. Figure from [30]

The "stacking" technique to fabricate vdW heterostructures has several advantages. First, the cleanliness and quality of the vdW heterostructures fabricated this way is exceptionally high, and on par with molecular beam epitaxy (MBE). However, unlike MBE, vdW stacking succeeds even when there is a large lattice mismatch in the constituent vdW materials.

1.3.1 Proximity effects in van der Waals heterostructures

A *proximity effect* occurs when one vdW material inherits the properties of the material next to it, simply by being in close proximity of it. An example of a proximity effect is when graphene is placed on top of hBN with small to zero misrotation between the layers. Putting graphene on hBN leads to an electrostatic sublattice potential on the graphene lattice. This sublattice potential changes the energy of the A and B sublattices differently, which leads to the opening of a band gap in graphene. This effect was demonstrated experimentally by three research groups in 2013 [31, 32**?**].

There are other proximity effects that have been demonstrated in heterostructures of graphene. Proximity induced spin orbit coupling (SOC) is achieved by using TMDs MoS_2, WS_2, and WSe_2[33, 34, 35]. Magnetic proximity effects have been attained in graphene with the use of non-vdW magnets EuS and YIG[36, 37]. The latter additionally also induces a proximity SOC, which leads an anomalous Hall resistance in the graphene devices[37]. These results pertaining to proximity SOC and proximity magnetism are discussed in more detail later in section 4.2.

1.3.2 Twist angle in van der Waals heterostructures

An extra degree of freedom in such vdW heterostructures is the misrotation "twist angle" between successive vdW materials. This can drastically alter the properties of the vdW heterostructure. In a graphene on hBN heterostructure, the twist angle between graphene and h-BN impacts the long range moiré lattice periodicity and the resultant superlattice potential (graphene and h-BN have a 2% lattice mismatch at zero degree twist angle). By controlling the twist angle, this band gap can be engineered roughly between 8 meV and 25 meV [31].

When two monolayers of graphene are stacked such that the twist angle is precisely 1.1°, strong electron-electron correlations drive the system into a phase space of states that include Mott insulator behavior, unconventional superconductivity, and unconventional magnetism[38, 39, 40, 41]. Neither of the two constituents that go into making this superstructure (i.e. graphene) are Mott insulators, or superconductors or magnets. This very clearly demonstrates how van der Waals heterostructures can be made such that the end product is greater than the sum of its constituents.

1.3.3 Graphene-Insulator-Graphene junction

As another example of a vdW heterostructure, the graphene-insulator-graphene (GIG) junction is discussed. The GIG junction motivated a chemical vapor deposition (CVD) project which is covered in Chapter 2. The GIG junction comprises of two monolayers of graphene that are separated by a thin h-BN flake that acts as a tunneling barrier[28]. For most optimal tunneling characteristics through the tunnel barrier, 3 or 4 layers thick h-BN flakes work the best. The graphene-hBN-graphene GIG junction is connected to a global Si^{++} back gate, on which a gate voltage V_g is applied. Additionally, a bias voltage V_b is applied between the bottom and top graphene electrodes. Thus, by changing both V_b and V_g simultaneously, the chemical potential (and hence, carrier density) of both graphene electrodes can be tuned.

The device working principle is based on tunneling current between the two graphene electrodes through the h-BN. In order for tunneling to take place, there must exist filled states in the top (bottom) graphene and empty states in the bottom (top) graphene. Additionally, the tunneling process must conserve momentum.

For now, let us focus on tunneling where the two states have matching momentum, and ignore indirect processes such as phonon assisted tunneling. When the device is under biased or over biased (Fig. 1.8a and b respectively), only a small number of states satisfy the momentum conserving tunneling criterion (circled). This results in a small tunneling current. At a particular bias voltage equal to the chemical potential difference, a large number of states are available to participate in tunneling (Fig. 1.8c). At this resonant condition, a large tunneling current results. The calculated I-V characteristics are shown in Fig. 1.8d. At the resonant condition there is a sharp maximum in current, leading to non-linear I-V characteristics and negative differential resistance.

Experimentally, the functionality of this device has been demonstrated by Britnell et al., using exfoliated vdW crystals[42, 43]. As can be seen in Fig. 1.9, there is good agreement between theoretical predictions and experimental observations of the device's I-V characteristics, at different V_g values. A note with regards to phonon assisted indirect tunneling: This is a relatively weaker effect, and does not significantly alter the device characteristics. The effect of this effect is a linear background that is visible in the experimental data of Fig. 1.9c but is missing in the earlier theoretical calculation shown in Fig. 1.9a and has since been explicitly confirmed with further calculations [44].

1.4 Concluding remarks

VdW heterostructures are a powerful system to study novel physical phenomena in two dimensions. VdW materials exhibiting a broad range of physics exist now, giving rise to an even larger number of possible heterostructures that can be assembled. Beyond the sequence of layer by layer materials, the physical properties can be further

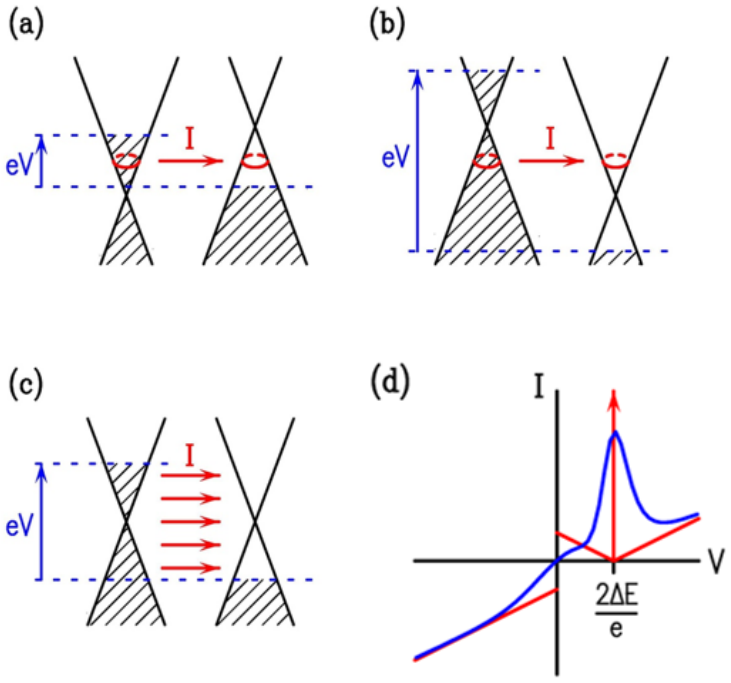

Figure 1.8: Working principle of a GIG junction
Energy bands of the two graphene sheets when the device is (a)Under-biased (b) Over-biased (c) In resonant condition. (d) Calculated I-V characteristics of device. At the resonant condition, the current is maximized, leading to a non-linear I-V profile. Adapted from [28]

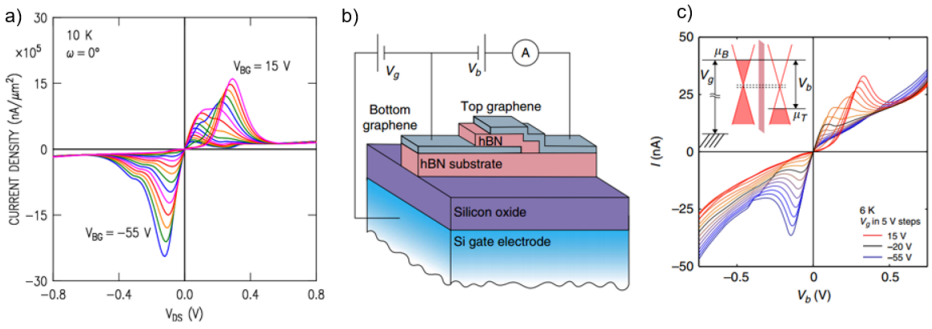

Figure 1.9: I-V characteristics of a GIG junction
(a) Theoretical I-V calculations at various back gate voltages (b) Schematic illustrating structure of device (c) Experimental data observed by Britnell et al., [43] Adapted from [43, 44]

engineered by varying the material thickness, proximity effects, tuning carrier density by means of electrostatic gating, and changing the twist angle between layers. The

end result is a large, highly controllable playground of physics at our disposal.

Chapter 2

Large scale chemical vapor deposition of van der Waals heterostructures

The vdW heterostructures discussed in chapter 1 have all been fabricated utilizing exfoliated flakes that are of length scales $\sim 10\mu$m. While this creates the highest quality devices, the technique is not scaleable for technological applications which require much larger length scales $\sim$1cm. In this chapter we discuss a project pertaining to the CVD growth of h-BN on graphene on copper covered surfaces, which would be a step towards realizing novel devices such as the GIG junction on an industrial length scale.

2.1 Introduction

A large number of growth studies have been conducted over the past decade for various 2D materials including graphene and h-BN, with metal substrates being often employed[45, 46, 47]. The presence of the metal is generally acknowledged to provide some catalytic activity for the decomposition of the precursor molecules and the subsequent formation of the graphene or h-BN films[48, 49]. Indeed, for single monolayer of h-BN, this growth mode was elucidated in the early works of Nagashima et al. and Auwärter et al[50, 51, 52].

For application in electronic devices, thin films of 2D materials must be removed from those substrates and then transferred onto an insulating material[53, 54]. For heterostructures, containing thin layers of different materials, the number of steps needed to build up the structure can be relatively large. Possible contamination induced by the transfer process, for each transfer step, might then be deleterious to the electrical properties of the final device[55, 56]. For this reason, a number of authors have investigated the growth of different 2D layers, one on top of the other, with the goal of epitaxially forming a heterostructure[57, 58].

For the case of graphene and h-BN, prior studies have been performed for both graphene on h-BN and h-BN on graphene[59, 57]. The former is somewhat more common, since h-BN itself has been demonstrated to be a relatively ideal, insulating substrate for growth (or transfer) of 2D layers[13]. Nevertheless, some work involving h-BN on graphene has been reported[60]. In principle, the ability to deposit h-BN layers on graphene, and then follow that by a subsequent graphene deposition, could lead to the formation of large-area GIG tunneling junctions that were discussed in sec. 1.3.3.

2.2 Growth procedure

2.2.1 Graphene growth on Cu

Graphene growth was achieved using atmospheric pressure chemical vapor deposition (APCVD) on ultra-flat copper substrates. To prepare these substrates, bulk oxygen-free electronic grade ultra-pure (99.99%) copper rods were used as starting material. These 30 cm copper rods, 25.4 mm in diameter, were then machined down to 1.2 mm thick slices, using conventional machining tools and single point diamond turning. Before graphene growth, these substrates were annealed for 8 hours at 1000°C, in 70 sccm of 2.5 vol % H_2/Ar mixture. During the growth process, the substrates were subsequently annealed at 1050°C for 1 hour under 186 sccm flow of 2.5 vol % H2/Ar mixture. 14 sccm of 0.1 vol % CH4/Ar mixture was then introduced for 1.5 hours as the precursor gas. This procedure has shown to produce large continuous 1 ML thick graphene domains[61, 62]. The ultra-flat copper substrates used for this process were shown to have a root mean square surface roughness of 2 nm, resulting in graphene that is 50 times smoother than graphene obtained on standard 25 μm thick copper foils[61]. The samples were then characterized using low energy electron diffraction (LEED) and microscopy tools prior to h-BN growth.

2.2.2 h-BN growth on graphene on Cu

h-BN growth was carried out in a high-vacuum deposition system, with base pressure of 10^{-9} Torr. After degassing, the samples were exposed to 10^{-4} Torr of borazine, $(BH)_3(NH)_3$, for 30 minutes. During borazine exposure, the sample was heated to temperatures of 900°C or 1000°C. As will be discussed later, the surface morphology is governed by the growth temperature. In brief, the samples prepared at 900°C mainly retain the 1-ML-graphene coverage of the starting substrate, as well as forming some h-BN islands, whereas for the samples prepared at 1000°C the original graphene is nearly all converted to a mixed h-BN/graphene (h-BNC) alloy.

2.3 Characterization techniques

Immediately following borazine exposure, the samples were transferred in situ to a large area LEED system (Omicron SPECTALEED), which also allowed in-situ measurement of Auger electron spectroscopy (AES). Further characterization was performed by removing the samples from the growth system and transferring them through air to an Elmitech III low-energy electron microscope. This system also contains a VG Scientific Clam 100 hemispherical analyzer which was employed for ex-situ AES measurements (5 keV electrons). Additional characterization was performed with a JEOL 2100F transmission electron microscope (TEM) with electron beam energy of 200 keV, utilizing a GIF Tridiem 863 system for electron energy loss spectroscopy (EELS) and mapping. Prior to this measurement, the BN/graphene films were separated from the Cu substrate and transferred onto a TEM grid.

2.3.1 Fingerprinting vdW heterostructures with low energy electron reflectivity

The main tool we employ to characterize our grown films is a low energy electron microscope (LEEM)[63]. In LEEM, electrons with energies of 20 keV are excited from an electron gun. Using electromagnetic fields, these electrons are decelerated to energies of 0-20 eV, and focused on the sample surface. The reflected "backscattered" electrons (and not the secondary electrons unlike in scanning electron microscopy) travel back through the electromagnetic lenses and are picked up by the detector. Because of the low energies of the electrons involved, LEEM is a powerful surface sensitive technique. Additionally, by continuously acquiring a series of images as the electron energy is changed from 0 to 20 eV, we can extract a low energy electron reflectivity (LEER) spectrum. LEER spectra provide a unique fingerprint of the local electronic structure of the surface being probed, thereby yielding chemical information about the surface composition[64].

As an illustration, LEER spectra obtained from different surfaces that have been recently studied are shown in Fig. 2.1. All of these surfaces are described in detail in separate publications[65, 66]. Figs. 2.1(a) - 2.1(c), are from an earlier study of h-BN on epitaxial graphene on SiC[66]. For the first two spectra, acquired from 1 and 2 monolayers of graphene, they reveal one or two distinct minima, respectively, in the low energy range of $0 - 5$ eV. Such spectra for epitaxial graphene are well understood based on recent studies[67, 68, 69]. The reflectivity minima arise from interlayer states, which are plane-wave type states that form in the spaces between graphene layers. In general n layers of a 2D material will have $n-1$ spaces between the layers. Hence, combinations of interlayer states are formed and these lead to $n-1$ minima in a LEER spectrum. For the specific case of epitaxial graphene on SiC, there is an additional underlying graphene-like layer on the surface, the so-called buffer layer[70]. An interlayer state is also formed between that layer and the graphene ones above.

Hence each minimum in the LEER spectra corresponds to one graphene layer, as first deduced by Hibino et al.[69].

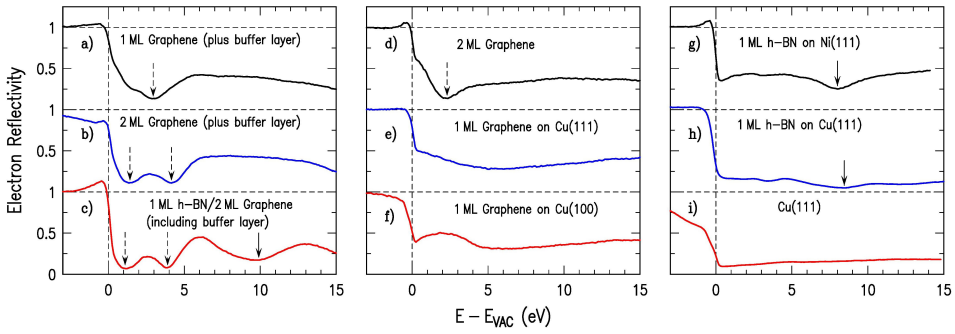

Figure 2.1: LEER spectra for graphene and h-BN films
LEER spectra for combinations of 1 ML graphene, 2 ML graphene, and 1 ML h-BN on different substrates, as labeled. Panels (a)-(d) are on SiC. Panels (e)-(i) are on metallic substrates.

When h-BN is present on the surface, then the situation changes. The interlayer states and associated reflectivity minima still exist in the 0 – 5 eV range from graphene. Additionally, the h-BN produces an additional minimum located at 8 – 9 eV. This additional minimum is formed from a specific band structure feature of the h-BN that, again, is well understood based on recent work[65, 66]. This feature can be seen in Fig. 2.1(c), as well as Figs. 2.1(g) and 2.1(h) for h-BN on Ni and Cu, respectively, and it permits identification of h-BN on the surface (In Figs 2.1(g) and 2.1(h), a very small oscillation in the reflectivity is also apparent at about 4 eV, and, like the minimum at 8 – 9 eV, this small feature is also characteristic of the h-BN)[65].

Now considering the situation when graphene or h-BN resides directly on a metal surface, then as previously discussed, an interlayer state can form between the 2D layer and the surface so long as the separation between the two is sufficiently large, $>\sim 3\mathring{A}$[68]. The energy of this interlayer state varies inversely with the separation. For single-layer graphene on Cu(111) and Cu(100) surfaces, as seen in Figs. 2.1(e) and 2.1(f), the broad minima centered at about 6 eV arise from this interlayer state. For Fig. 2.1(d), with 2 ML of graphene, the dominant feature is simply the distinct interlayer state arising from the space between the two graphene layers, and the underlying interlayer state (from the graphene-Cu space) is scarcely visible. Finally, for Fig 2.1(f) an additional feature is visible, a plateau extending from about 0 – 4 eV. This feature arises from the band structure of the underlying Cu(100) substrate, which has a bandgap in its energy spectrum for electrons propagating in the (100) direction.

2.4 Results

2.4.1 Graphene on Cu samples

Typical LEEM and LEER results obtained from the surface after APCVD of graphene are shown in Fig. 2.2. The LEEM image of Fig. 2.2(a) reveals predominantly bright contrast, with a fine array of stripes extending over the entire surface. Such stripes are known to arise from faceting of the metal surface underlying the graphene, having been reported previously for Cu(100) surfaces[68, 71]. The facets arise because the surface normal vector happens to be slightly different than some particular low-index face, which is not surprising in our case since a low-index crystal face in the starting rod of material is not expected to be precisely aligned along the rod direction. Hence, during the APCVD growth of graphene, the underlying Cu surface adopts a faceted orientation, e.g. for a face that is vicinal to (100) it forms (100) and (410) facets[71].

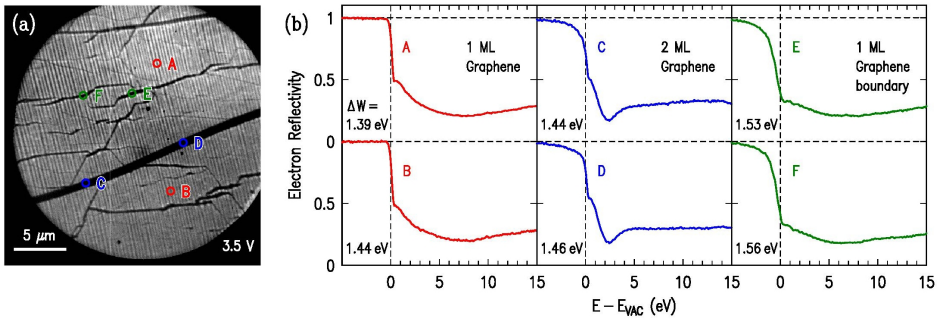

Figure 2.2: Low energy electron characterization of APCVD-grown graphene on Cu (a) LEEM image of APCVD-grown graphene on Cu, acquired with sample voltage of 3.5 V. (b) Reflectivity spectra, extracted from the points indicated in the image. The ΔW values list the work function difference between the corresponding surface location and the LEEM electron emitter.

The LEER spectra of Fig. 2.2(b) allow us to draw some qualitative conclusions about the Cu orientation. Most of the surface is seen to be covered with a single monolayer of graphene, as is apparent from the single broad minimum (centered near 7 eV) seen in spectra A and B. (The data of Fig. 2.1(e) is from a separate location on the same sample, and shows the same broad minimum). A similar broad minimum has been seen in prior studies for graphene on a Cu surface with known (111) orientation[68]. In contrast, as shown in Fig. 2.1(f), a Cu(100) surface has a plateau in the reflectivity over 0 – 4 eV, a feature that is clearly not evident in the spectra of Fig. 2.2(b)[68]. On this basis, we can be confident that the surface does not contain (100)-oriented facets, and its behavior is similar to that seen previously for (111) facets, but no further conclusions can be drawn concerning the precise orientation of the Cu.

A notable feature in the LEEM image of Fig. 2.2(a) is the wide, dark strip extending nearly horizontally across the surface area. LEER spectra of this area, shown by C and D of Fig. 2.2(b), reveal the characteristic minimum near 2 eV associated with a single interlayer state between two graphene layers. Hence, this area of the surface is covered with two ML of graphene. We also commonly observe 2-ML areas on the surface in the form of hexagonal areas, as revealed in the additional LEEM images presented below. Another feature that is apparent in the LEEM images are the somewhat irregular dark lines (appearing as "cracks") extending over the surface. Detailed reflectivity measurements on those regions, E and F of Fig. 2.2(b), reveal 1 ML graphene with spectra very similar to those of A and B. The similarity of their spectra indicates that these "crack" areas consist, predominantly, of 1 ML graphene. Two possible origins for these irregular "crack" areas can be envisioned: they might be a grain boundary of the Cu substrate beneath them, or that they might arise from grain boundaries of the graphene itself. The former possibility can be excluded by further consideration of the images. A change in grain orientation of the metal substrate is invariably accompanied by the change in contrast in the LEEM image over the entire grain (not just at the boundary)[68]. Hence, it appears that these "crack" features arise from grain boundaries of the 1-ML graphene film.

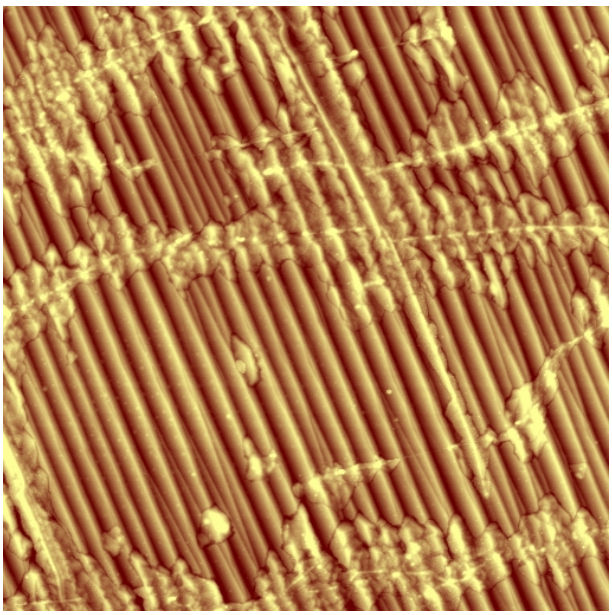

Figure 2.3: AFM image of as grown graphene on Cu
10x10 μm^2 AFM image of as-grown graphene on Cu. Surface height is shown by a color scale (dark to bright) with a range of 50 nm. Faceting of the surface is clearly seen, with the facets extending along an in-plane direction of about 20° counter-clockwise from vertical. Narrow, bright lines that cross the facets are also apparent, and are attributed to grain boundaries in the graphene.

The occurrence of grain boundaries in the graphene, as well as faceting of the underlying copper are further confirmed by examining the sample with AFM. The AFM image in Fig. 2.3 clearly shows the facets of the Cu surface underlying the graphene, and it also shows a network of narrow lines, ∼50 nm in width, most of which are nearly horizontal in this particular image. We associate these lines with the same grain boundaries seen in the LEEM images. The AFM image clearly reveals that the Cu facets are continuous in terms of both in-plane direction and out-of-plane surface orientation when one of the grain boundaries is crossed. Such continuity is not expected if the boundaries arise from grain boundaries in the underlying copper, which would in general lead to different in-plane and out-of-plane facet orientations on either side of the boundary. Hence, we confidently assign the boundaries to grain boundaries in the graphene layer itself.

Returning to spectra E and F of Fig. 2.2(b), we note that their transition to unity reflectivity, for energies below 0 eV, is much more gradual than for spectra A and B. This type of gradual transition is a signature of a surface area having larger work function than the surrounding areas[72]. Based on the method described in [1], we calculate ΔW, the work function difference between the electron emitter and the specific point on the surface. We see that on average, the work function of the 2-ML graphene areas are very slightly higher than those of the 1-ML areas, and the work function of the graphene domain boundaries are higher still.

The precision in the relative work function determination is $\pm 0.01\ eV$ for sharp transitions to unity reflectivity, and $\pm 0.05\ eV$ for gradual transitions. Inhomogeneity in the energies of incident electrons, arising from either detailed lens alignments or stray electric fields within the LEEM can give rise to an error as large as $\pm 0.10\ eV$, which is visible in Fig. 2.2b between points A and B. We eliminate effects of such inhomogeneity by considering values acquired from closely spaced points on the surface. We determine that the work function of the 2-ML graphene is $0.06 \pm 0.03\ eV$ greater than that of the 1-ML graphene, and the work function of the domain boundaries in the 1-ML graphene is $0.15 \pm 0.05\ eV$ greater than that for the pristine 1-ML material. As we shall see, these changes are all relatively small compared to when h-BN is incorporated into the graphene.

2.4.2 Borazine exposure to graphene surface at 900°C

Figure 2.4 shows in-situ LEED patterns obtained from an APCVD-grown graphene sample before and after exposure to borazine, with the sample held at 900°C during the 30 minute exposure. Prior to borazine exposure, Fig. 2.4(a), we observe six symmetric spots shown around a central (0,0) spot. These six spots correspond to the primary graphene (1,0) reciprocal lattice points. We do not observe any clear diffraction spots associated with the Cu surface, due to its vicinal nature as discussed in section 2.4.1.

After borazine exposure, Fig. 2.4(b), we observe the emergence of a circular ring

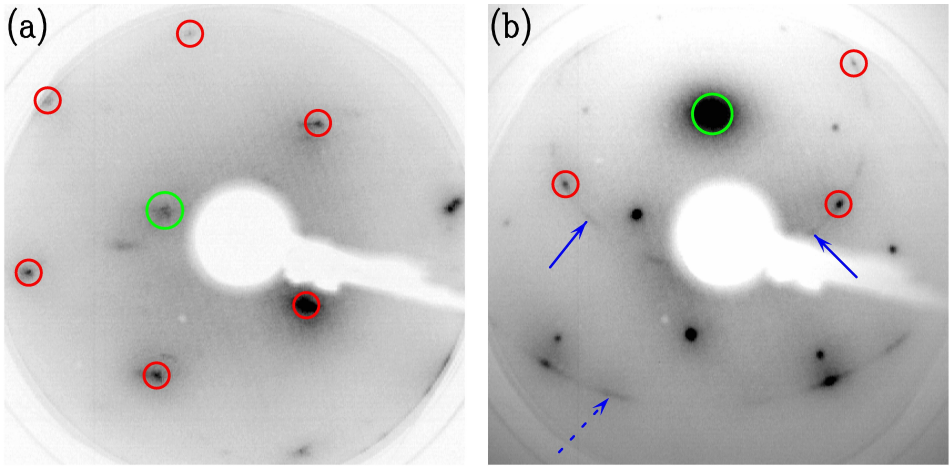

Figure 2.4: Electron diffraction patterns before and after borazine exposure (a) LEED pattern acquired from APCVD-grown graphene sample on Cu. (b) LEED pattern acquired from the same sample after exposure to borazine at 900°C. Both patterns are acquired with electron energy of 100 eV. Small red circles indicate the (1,0) primary graphene diffraction spots, and the large green circles indicate the (0,0) origins of the patterns. Solid blue arrows in (b) indicate the streak arising from the primary h-BN diffraction, and the dashed arrow indicates the streak from higher order diffraction.

of intensity (labelled by two solid blue arrows) at nearly the same wavevector as the graphene (1,0) spots. (This diffraction pattern is shifted as a whole slightly upwards due to an intentional non- zero angle of incidence of the incoming electrons). Such a ring of intensity is indicative of h-BN, based on previous work conducted on an SiC substrate[66]. The radius of the ring is nearly the same as the graphene (1,0) wavevector magnitude because the lattice constants of h-BN and graphene are nearly identical (1.6% lattice mismatch[57]). The fact that we observe a ring of intensity instead of a hexagonal pattern with threefold symmetry (that is, six spots alternating between high and low intensities) implies that the h-BN domains are oriented in a random rotational distribution.

We also observe another larger circular ring of intensity around the (0,0) spot arising from rotationally disordered (1,1) diffraction of the h-BN (wavevector radius of $\sqrt{3}$ times that of the primary diffraction). Similarly, the two distinct diffraction spots seen along this ring arise from graphene (1,1) diffraction. Several additional diffraction spots (with wavevectors not equal to those of h-BN or graphene diffraction) appear in this pattern, presumably from the underlying Cu, but again, such spots vary from place to place on the sample surface and are difficult to use for determining surface orientation since they do not, in general, arise from a single low-index crystal face.

LEEM and LEER results from the 900°C exposed samples are displayed in Fig. 2.5.

The LEEM image in Fig. 2.5(a) reveals the underlying copper surface to be nearly identical to that of the as-grown graphene sample in Fig. 2.2. That is, the majority of the surface shows a bright contrast with an array of stripes arising from faceting of the copper surface. The LEER spectra for points A and B in Fig. 2.5(b) reveal 1 ML of graphene on top of Cu surface, very similar to those of Figs. 2.1(e) and 2.2(b). We find that the majority of the sample is still covered with 1 ML graphene. In addition, three 2-ML graphene domains are observed in the image, as revealed by spectra C and D, with the domains being $\sim 5\ \mu m$ in extent.

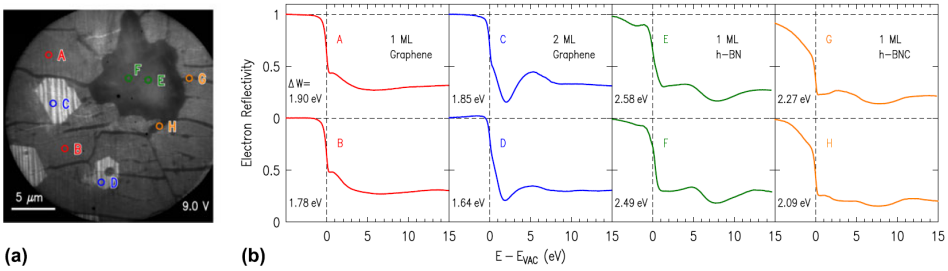

Figure 2.5: LEEM and LEER characterization of a 900°C borazine exposed sample (a) LEEM image of graphene sample exposed to borazine at 900°C, acquired with sample voltage of 9.0 V. (b) Reflectivity spectra extracted from the points indicated in the image.

One contrasting feature, unseen in the samples prior to borazine exposure, is the appearance of a dark contrast "island", 10 μm in size. Reflectivity spectra from this island, E and F, reveal a clear minimum near 8 eV, indicative of the band structure of h-BN as discussed above in connection with Fig. 2.1(g) and 2.1(h). However, we do not observe any minimum arising from an interlayer state in the 0 – 5 eV range, demonstrating that we have just a single layer of 2D material on the surface. Hence, the 1-ML h-BN is grown on top of bare Cu, rather than on top of 1 ML of graphene. We note that, unlike the areas covered with graphene, we do not observe any faceting of the copper surface underneath the h-BN. The h-BN coverage seems to inhibit the faceting of the surface, and suggests that the occurrence of the faceting is dependent on the coverage of the surface. We also note that the work function of the h-BN area is found to be $\sim 0.6\ eV$ larger than that of the surrounding graphene.

Another subtle difference from the as-grown graphene samples has to do with the set of dark "cracks" in the LEEM image. For the as-grown graphene samples in Fig. 2.2, we found that these areas consisted of domain boundaries in the graphene film, but with LEER spectra still characteristic of single ML graphene. In these 900°C exposed samples, however, the LEER spectra G and H are significantly different. Most notably, there is not a broad minimum near 6 eV as was seen in the 1 ML graphene areas. There is a minimum found at 8 eV, but this minimum is shallower than what was obtained from h-BN covered regions. In fact, the LEER spectrum appears to be a superposition of the reflectivity spectrum from that of graphene and h-BN, which

could suggest an h-BNC alloy mixture on the surface. Additionally, the observed work functions of these apparent h-BNC areas are intermediate between the h-BN and the graphene. The absence of an interlayer state in the 0-5 eV range implies that this layer is 1 ML thick. Further results from characterization of surfaces held at 1000°C during borazine exposure as well as from AES and EELS measurements discussed later, support this identification of h-BNC alloy formation on the surface.

2.4.3 Borazine exposure to graphene surface at 1000°C

In-situ LEED patterns obtained from the samples after exposure to borazine at 1000°C do not show any noticeable difference from the patterns acquired from the as-grown graphene. Most importantly, unlike the samples exposed to borazine at 900°C, we do not observe any circular streaks passing near the graphene (1,0) spots. Neither do we observe any additional hexagonal spots at nearly the same distance from the (0,0) spot that could have arisen from h-BN. This implies that there are not any h-BN islands on the surface of these 1000°C exposed samples, in contrast to the results for the 900°C exposed surfaces.

LEEM and LEER data from the 1000°C exposed samples is shown in Fig. 2.6. In the LEEM image of Fig. 2.6(a), the majority of the surface exhibits a relatively dark contrast. LEER spectra obtained from this region, A and B of Fig. 2.6(b), are consistent with those seen earlier in the 900°C exposed samples in Fig. 2.5 that were identified as 1 ML h-BNC alloy. However, in contrast to the 900°C exposed samples where this alloy mix was observed only in the narrow crack areas, for the 1000°C exposed samples such spectra are found over nearly the entire surface. Also, the copper surface underneath the h-BNC does not show any faceting, which once again suggests that the faceting is coverage dependent, and is being inhibited by the presence of BN on the surface.

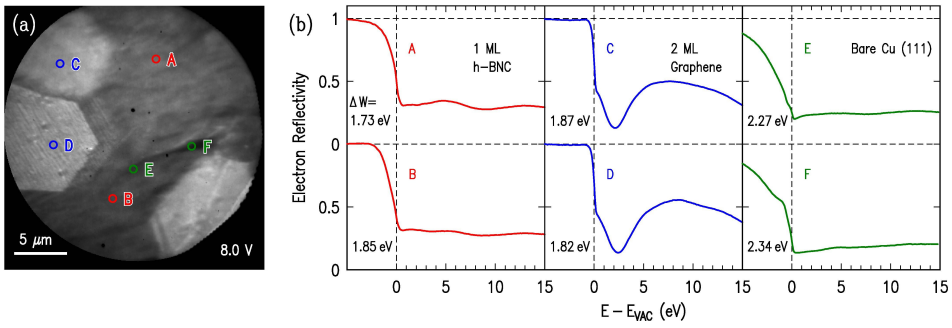

Figure 2.6: LEEM and LEER characterization of a 1000°C borazine exposed sample (a) LEEM image of graphene sample exposed to borazine at 1000°C, acquired with sample voltage of 8.0 V. (b) Reflectivity spectra extracted from the points indicated in the image.

As usual, we observe hexagonal 2-ML graphene domains on the surface (reflectivity

spectra C, D). In general, these regions covered with 2 ML graphene do not appear to get modified upon exposure to borazine. Lastly, over a small minority of the surface, we observe irregular dark voids (points E, F of Fig. 2.6(a)). Reflectivity spectra from these areas reveal that these regions are relatively featureless, indicative of bare (or possibly oxidized) Cu. That is, it appears that in these regions the original graphene has been etched away, possibly due to the presence of hydrogen in the chamber from the borazine.

2.4.4 Electron energy loss spectroscopy results

We utilize electron energy loss spectroscopy (EELS) and Auger electron spectroscopy (AES) to quantify the BN coverage of our samples. EELS results from a sample prepared at 1000°C are displayed in Figs. 2.7 and 2.8. Figure 2.7(a) shows an image of the film, lying across a circular aperture of the TEM grid. Selected-area electron diffraction of this area of the film is shown in Fig. 2.7(b), revealing the hexagonal pattern of the BN/graphene. Figure 2.8(a) shows an image of another area of the film. In this case the film is seen to be folded over onto itself. EELS mapping of the B, C, and N K-edges are displayed in Figs. 2.8(b) – 2.8(d), respectively. All elements are seen to be present in the film. Quantification of the B and N concentration indicates a 1:1 stoichiometric mixture, within about ∼10%. Careful examination of the B and N EELS maps reveals that the elements are inhomogeneously arranged, with domains of size 0.1 – 0.3 μm that contain little or no BN (these dark-contrast domains are most clearly seen in the maps of the B, since it has a much larger EELS cross-section than N does), with the remainder of the film containing more BN. The C content is seen to be relatively uniform over the film, so that the domains with little or no BN are essentially pure graphene whereas the areas with significant BN consist of h-BNC alloy.

2.4.5 Auger electron spectroscopy

Typical AES curves from samples exposed to borazine at 900°C and 1000°C are displayed in Figs 2.9(a) and 2.9(b), respectively. These samples reveal KLL peaks arising from B, C and N atoms, as well as LMM Cu peaks. The amount of B, C and N in these samples is estimated from respective peak-peak intensities, comparing to a reference sample consisting of 0.3 ML of h-BN grown on epitaxial graphene on SiC, as displayed in Fig. 2.9(c)[65]. It can be seen quite clearly that the B and N intensities in the latter spectrum are much stronger than those observed in Figs. 2.9(a) and 2.9(b). By comparing peak ratios in the respective spectra, we find that the ratio of B to N concentrations in our borazine-exposed samples is 1:1, within our experimental errors of about ∼10%. Considering the ratio of the BN to the graphene, a concentration ratio cannot be directly deduced based on comparison to the reference, since that sample also contains C in the underlying SiC. However, as an estimate, we can use

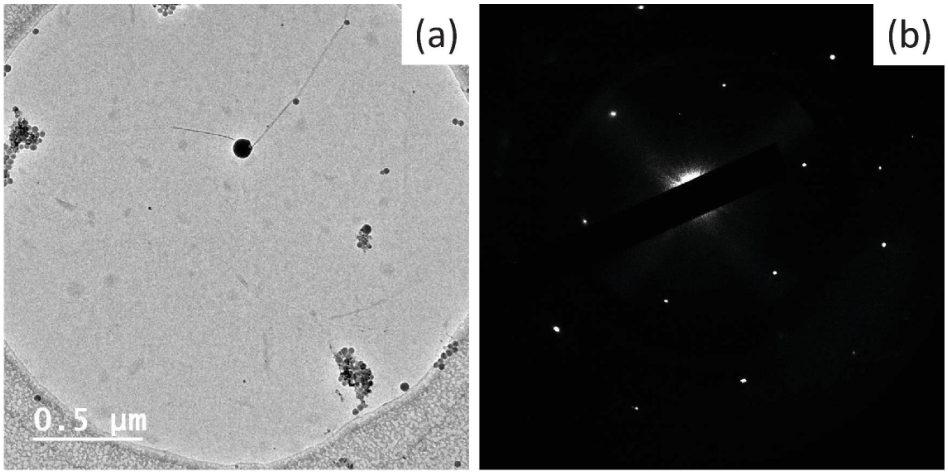

Figure 2.7: TEM characterization of h-BN-graphene film
(a) TEM image of h-BN-graphene film, and (b) selected-area electron diffraction pattern.

just the B:C and N:C intensity ratios from Figs. 2.9(a) and 2.9(b), converting those to concentration ratios employing tabulated values for the energy dependent relative elemental sensitivity[73]. In this way, we obtain a BN coverage on both the 900°C and 1000°C exposed samples of ~ 0.1.

We have also performed in-situ AES measurements on our samples immediately after borazine exposure. Those spectra reveal an additional prominent feature not found in the ex-situ spectra, namely, a much stronger B:N concentration ratio (about 6:1) for both the 900°C and 1000°C samples. This boron peak intensity was, however, found to be reduced to 1:1 after the samples were air transferred and then heated in vacuum to 300°C for 20 minutes prior to ex-situ AES. We believe the excess boron seen in the in-situ AES is atomic boron that had dissolved into the bulk of Cu at the growth temperatures and then precipitated out when the sample was cooled, as reported in prior work[74]. Since the samples are transferred (and/or stored) in air, the atomic boron readily oxidizes to volatile boron oxides and then desorbs during the heating prior to the ex-situ AES measurements.

2.5 Discussion

After atmospheric pressure graphene growth on Cu substrate, we have investigated the exposure of graphene-on-Cu samples to borazine, in a high vacuum environment. Depending upon the growth temperature, the BN has been observed to occur either as isolated h-BN islands (900°C growth), or in a mixed phase of 1 ML h-BNC alloy (both 900°C and 1000°C growths). The observation of isolated h-BN islands is a feature that is common for growth on epitaxial graphene on SiC. It has been recently

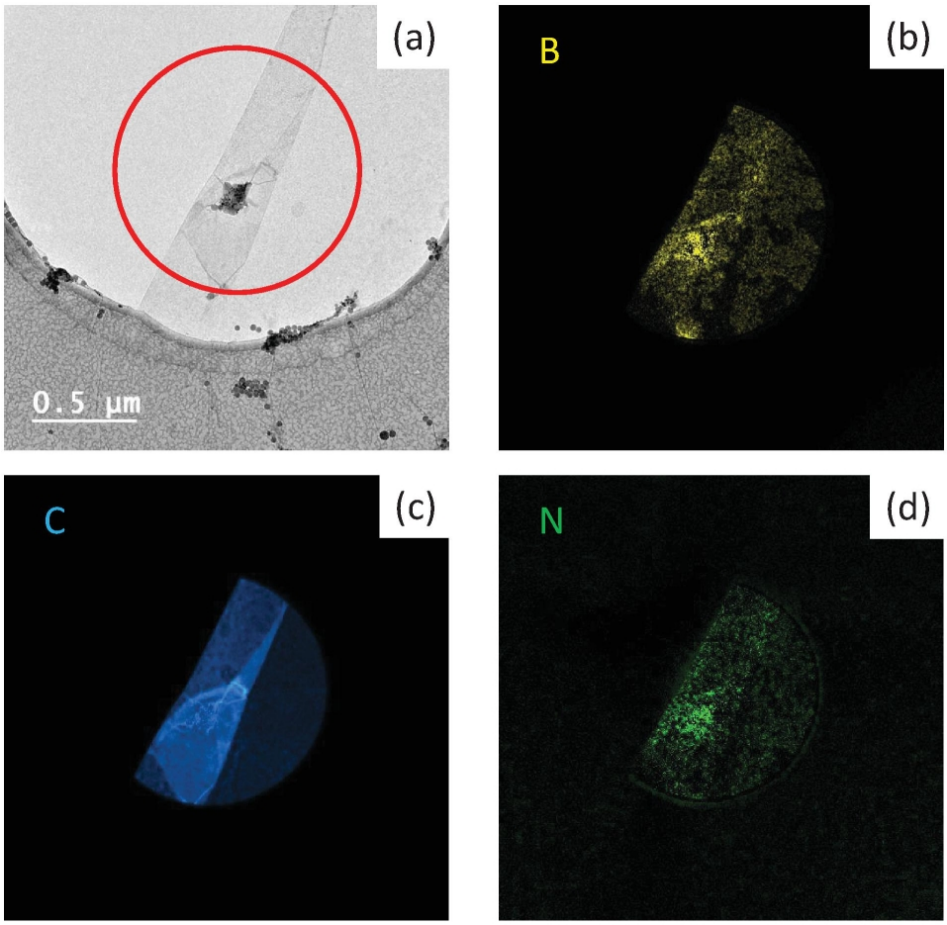

Figure 2.8: EELS mapping on h-BN-graphene film
(a) TEM image of graphene/BN film, along with (b) – (d) EELS mapping of B, C, and N, respectively, of the region indicated by a circle in (a).

determined that for the case of epitaxial graphene on SiC, borazine exposure results in $\sim 2\ \mu m$ sized grains of h-BN islands that grow by substituting for the graphene surface. The carbon atoms in this case are pushed underneath the h-BN, above the SiC[66]. The growth temperature in this work, 1100°C, is somewhat higher, which may play a role in the differing results (especially if the relevant activation energy barriers are relatively high). In any case, the present results for graphene on copper are interpreted based on the sequence of reactions depicted in Fig. 2.10.

It has been shown that the catalytic activity of metals such as Cu and Ni plays an important role in the decomposition of borazine[50, 51, 74]. As a result, we believe that the decomposition of borazine initiates at graphene domain boundaries, where it has direct access to the underlying Cu (Fig. 2.10(a)). Once the borazine molecules decompose on the surface, B and N atoms are available to be substituted for graphene at these domain boundaries, where substitution is energetically favorable. The onset

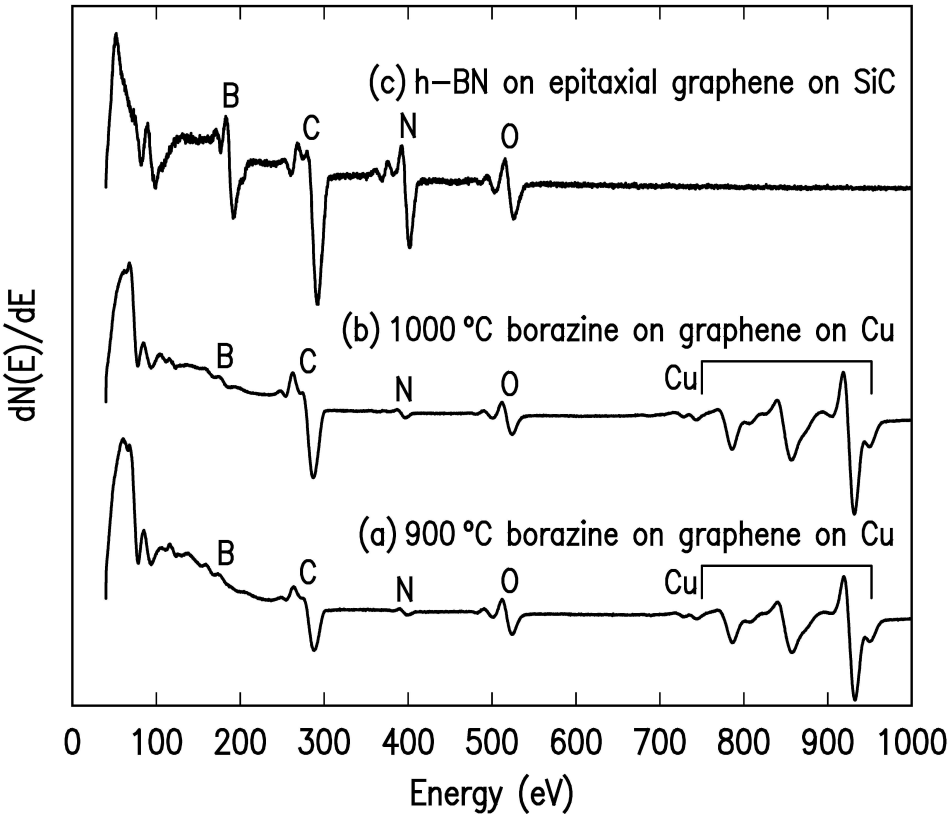

Figure 2.9: Auger characterization of h-BN-graphene films
Ex-situ AES obtained from (a) 900°C exposed samples, (b) 1000°C exposed samples and (c) h-BN film grown on epitaxial graphene on SiC.

of this substitution is shown in Fig. 2.10(b). Hydrogen atoms can desorb and leave as H_2. Fig. 2.10(c) illustrates multiple processes. Firstly, the presence of H atoms on the surface can facilitate further BN incorporation into the surface layer by etching away some of the graphene and forming methane[75]. In addition, it has been shown by Kidambi et al. that in our temperature range, boron also tends to dissolve into bulk Cu, precipitating out only when cooled down[74]. If needed, the B atoms can also intercalate into the graphene/Cu interface before dissolving in the bulk Cu[76]. N atoms on the other hand have a low solubility in Cu, which leads to the excess N atoms on the surface desorbing and leaving the system as N_2. We believe that these processes account for the high 6:1 B:N ratio that is observed in our in-situ AES measurements, since the nitrogen arises only from the surface whereas there are two boron sources: directly from the surface and that originating from the bulk Cu. This scenario is illustrated in Fig. 2.10(d). Once the samples are taken out of high vacuum and stored in air, the atomic boron, which has precipitated out from the Cu bulk, readily reacts with oxygen forming highly volatile boron oxides. Hence, we observe a B:N ratio of nearly 1 in the ex-situ AES measurements.

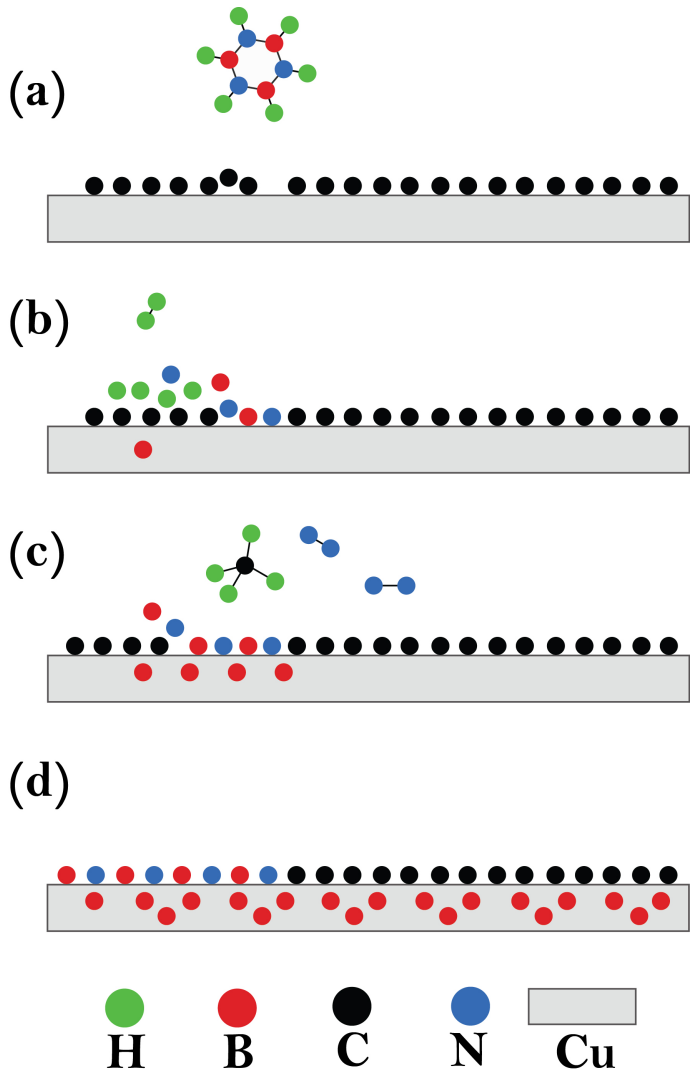

Figure 2.10: Schematic view of surface at different stages in the h-BNC growth process (a) Borazine molecule near a graphene domain boundary. (b) Borazine decomposition introduces BN at this domain boundary. (c) Additional BN is added where graphene is etched by H atoms, and B atoms dissolve into bulk of Cu. (d) Multiple cycles lead to BNC alloy on surface and atomic boron in the bulk of Cu, which precipitates out after sample is cooled.

While we observe a uniform 1 ML h-BNC coverage for the 1000°C exposed samples, the h-BNC alloy is found to be carbon dominated, implying that substitution of C atoms by BN is very limited. We speculate that this limitation is imposed by the availability of H atoms on the surface, i.e. those that do not desorb as H_2, and can thus etch the graphene. On the 900°C exposed samples, the fact that we observe primarily 1 ML graphene once again suggests that temperature is a crucial factor in

the growth dynamics. We find isolated μm-size h-BN domains on bare copper, but not on top of graphene. This observation reiterates the catalytic role of the underlying copper, and suggests that for h-BN growth, the graphene needs to be etched off by H atoms first to expose the underlying copper.

2.6 Concluding remarks

A large area growth of a vdW heterostructure of h-BN on graphene was attempted. The first step was APCVD of graphene on Cu substrates using methane as precursor. The second step was low pressure CVD of h-BN on graphene on Cu using borazine as the precursor gas. The APCVD-grown graphene samples on Cu were exposed to borazine at two different temperatures of 900°C and 1000°C. The samples were characterized using LEED, LEEM, EELS and AES measurements. At 1000°C, the surface was modified to yield a ML of h-BNC alloy. At a relatively low temperature of 900°C, however, the as-grown graphene retained its 1-ML characteristics over the majority of the surface. Isolated μm-size h-BN islands formed over a small portion of the sample surface, and h-BNC alloy was observed near grain boundaries of the original graphene layer. At neither temperature was h-BN growth observed on top of graphene (i.e. it only occurred directly on copper), indicating the importance of copper's catalytic activity in the growth process.

Chapter 3

Electron transport in multi-dimensional fuzzy graphene nanostructures

3.1 Introduction

As we have shown so far, atomically thin 2D materials posses a range of superlative electronic properties. In addition to electronics, they also posses electrochemical properties that facilitate applications in sensing, energy conversion, and storage. For example, graphene's exceptional surface-area-to-volume ratio (theoretically up to 2630 m^2g^{-1})[77] and catalytically active edges[78, 79] have spurred immense interest in creating three-dimensional (3D) nanostructures for applications in sensing,[80] energy conversion, and storage.

Efforts to synthesize graphene-based 3D nanostructures have resulted in polycrystalline graphene flakes arranged in complex networks[81, 82, 83]. Electron transport mechanisms in 2D single-crystal graphene films have been extensively studied with regard to the material's structure (e.g. edge termination,[84, 85] defect type and density,[86] crystallinity,[87, 88, 89] flake orientation and layer stacking[39]).

However, the underlying mechanisms cannot be directly extrapolated to polycrystalline 3D nanostructures due to the added dimensionality and intricate morphology. Thus, integrating a 3D arrangement of graphene flakes into functional electronic devices and developing a fundamental understanding of electron transport in such structures at a microscopic level remains an open challenge.

In this chapter, we report on electron transport mechanisms in a new multi-dimensional graphene-based nanostructure: nanowire templated-3D fuzzy graphene (NT-3DFG). The synthesis of this novel 3D geometry of free-standing graphene was recently reported [83]. We will begin by briefly explaining the growth techniques to synthesize NT-3DFG but refer readers to ref.[83, 2] for detailed step by step descriptions. We will then discuss the structure and composition of NT-3DFG as derived

from various characterization techniques. Finally, we will report results electrical transport measurements on isolated NT-3DFG nanowires and discuss the origin of the observed phenomena.

3.2 Synthesis of NT-3DFG

As a first step, Si nanowires (SiNWs) were synthesized. This was achieved through a vapour-liquid-solid (VLS) growth process, using Au nanoparticles as catalyst. Briefly, 2 cm x 2 cm square Si wafers with 600 nm thick SiO_2 were cleaned and functionalized with Au nanoparticles by dispersing a colloidal solution on top and letting the solvent evaporate away. These functionalized substrates were then introduced into a custom built low pressure CVD system. At a pressure below $1 \times 10^{-5}\ Torr$, the sample was heated to $450°C$ and a gaseous mixture of H_2 (80 sccm) and SiH_4 (20 sccm) was introduced with $P = 40\ Torr$ for 100 min which led to the nucleation and growth of the SiNWs.

The next step was to synthesize 3D fuzzy graphene on the templated SiNWs. This was achieved through a plasma enhanced CVD process (PECVD). Two separate synthesis conditions were investigated with the synthesis temperature either $700°C$ (*Condition A*) or $1100°C$ (*Condition B*). The templated SiNW substrates were heated to the synthesis temperature at 0.5 Torr. Once at the synthesis temperature, 50 sccm of CH_4 precursor gas (5% CH_4 in Ar) was flown for 10 min. The sample was cooled down under 100 sccm Ar flow.

3.3 Structure and composition of NT-3DFG

A schematic illustrating what NT-3DFG looks like is shown in fig. 3.1a. The templated fuzzy graphene is composed of single or few layer free standing graphene flakes. These flakes form a dense structure surrounding the intrinsic SiNW (i-SiNW) core.

Fig. 3.1(b)-(c) show high resolution transmission electron microscopy (HRTEM) images of NT-3DFG synthesized under conditions A and B respectively. The i-SiNWs are conformally coated by carbon. Increasing the synthesis temperature from $700°C$ (Condition A) to $1100°C$ (Condition B) increases the graphene flake size and density, observed through the increase in NT-3DFG diameter from (120 ± 20) nm to (250 ± 20) nm, respectively. We attribute the increase in graphene flake size to the enhanced nucleation and growth rates as synthesis temperature is increased[90, 91].

Using EELS curves at different points, we conclude that surrounding the i-SiNW core, there is first a thicker "graphite like" shell. Outside of this graphitic shell, EELS curves are consistent with graphene, pointing to free standing graphene flakes. In the case of Condition A, the majority of the radial structure is composed of free-standing single-layer graphene, with a narrow, sparse graphitic shell proximal to i-SiNW core.

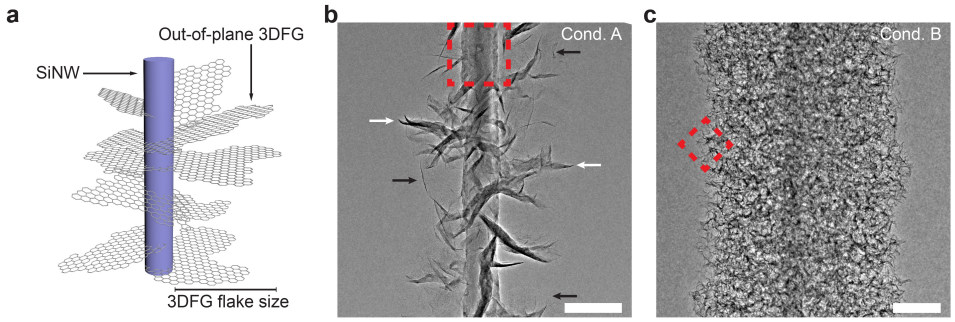

Figure 3.1: Morphology of NT-3DFG
(a) Schematic representing NT-3DFG composed of free-standing 3DFG flakes on a SiNW core. Representative HRTEM image of NT-3DFG synthesized under (b) Condition A and (c) Condition B. Scale bars are 100 nm. Black and white arrows denote single and multi-layer graphene flakes respectively.

In the case of Condition B, a thicker graphitic shell underneath single-to-few layer free-standing graphene flakes is observed. Synthesis under Condition B leads to a higher density of free-standing graphene flakes as well as a thicker graphitic shell compared to Condition A. Detailed EELS characteristics used to derive these results are available in fig. 2 of ref. [2].

3.4 Electron transport in NT-3DFG

To probe the electronic transport of NT-3DFG, we performed low-temperature four-terminal magneto-transport measurements on single NT-3DFG devices. We measured 3 devices each for Conditions A (devices A1, A2 and A3) and B (devices B1, B2, B3). All devices within a synthesis condition exhibited qualitatively identical behavior; here we focus our attention on devices A1 and B1 as representative devices for Conditions A and B, respectively (additional devices are presented in the Supplementary Information of ref. [2]).

We observe that the resistance of single NT-3DFG devices increases monotonically with decreasing device temperature (fig. 3.2b and fig. 3.2c). The resistance increases by a factor of 4.7 (0.25 $M\Omega$ at 300 K to 1.17 $M\Omega$ at 2 K) and 1.4 (18.14 $k\Omega$ at 300 K to 26.13 $k\Omega$ at 2 K) for devices A1 and B1 respectively. We note that electron transport in NT-3DFG occurs only through templated fuzzy graphene; no conduction was observed in i-SiNW devices. We explicitly confirm this by fabricating electronic devices out of only i-SiNW devices without any NT-3DFG synthesized on them.

We find that the net resistance of NT-3DFG, R(T), can be deconvolved into individual resistance components: R_0, a temperature-independent resistance, and R_{VRH}, a temperature-dependent resistance. Due to the presence of both free-standing graphene flakes and a graphitic shell in templated fuzzy graphene, we employ a par-

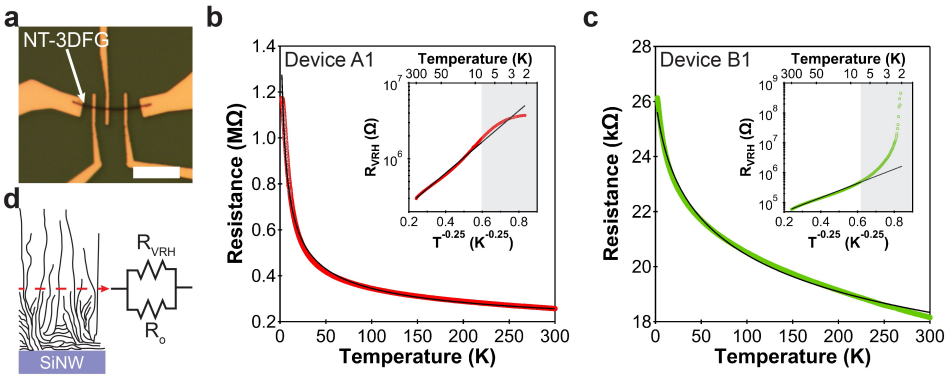

Figure 3.2: Electron transport in single NT-3DFG
(a) Optical image of a representative single NT-3DFG device. Scale bar is 5 μm. Resistance as a function of temperature acquired from single NT-3DFG devices (b) A1 and (c) B1. Empty red circles and solid black lines denote experimental data and parallel resistance electron transport model fit, respectively. Insets present VRH component of the measured four-terminal resistance (empty red circles) and theoretical VRH resistance determined from the parallel resistance model (black solid line) as a function of $T^{-0.25}$ (grey regions denote deviation from proposed model at low temperatures) (d) Schematic representing the cross section of NT-3DFG highlighting the origin of R_0 and R_{VRH}.

allel resistor model to describe the temperature-dependent transport. A schematic illustrating this electron conduction mechanism is presented in fig. 3.2d.

Electron transport in graphite exhibits metallic behavior due to the overlap between the valence and conduction bands[92]. Graphite's electrical resistivity is weakly dependent on temperature, whereas our devices show a much stronger temperature dependence. Therefore, we approximate the resistance contribution from the graphitic shell R_0 as being temperature independent.

The free-standing flakes in templated fuzzy graphene are in contact with each other along defect-rich edges. Transport in similar disordered graphene structures has been described by variable-range hopping (VRH) through localized states[93, 94, 95]. The temperature dependence of VRH leads to a resistance given by:

$$R_{VRH} = R_1 \, e^{(T_0/T)^{1/d+1}} \tag{3.1}$$

where, R_1, T_0 and d are a constant of proportionality, the Mott characteristic temperature, and the dimensionality of hopping, respectively[96]. We apply the VRH model along with a parallel resistance to describe the measured four-terminal resistance in NT-3DFG, leading to

$$R(T) = \frac{R_0 \, R_{VRH}}{R_0 \, + \, R_{VRH}} \tag{3.2}$$

where R_0 is a temperature-independent resistance from the graphitic shell and R_{VRH} is described by equation 3.1.

Based on a standard regression analysis, we find that 3D VRH (d = 3) best describes the temperature dependent transport in all NT-3DFG devices measured, although the quality of fit does not strongly depend on dimensionality (fig. 3.2b,c). The trend of increasing resistance with decreasing temperatures and successful fits using equation (3.1) suggests the presence of 3D hopping in the network of free-standing graphene flakes.

The extracted values for R_0 for devices A1 and B1 were 1.71 $M\Omega$ and 26.13 $k\Omega$ respectively. These values agree with previously reported resistivity magnitudes for graphitic structures. The difference in the magnitude of R_0 between Conditions A and B corroborates our conclusions of a sparser graphitic shell around the i-SiNW in Condition A as compared to Condition B. Additionally, the VRH component of the measured resistance fits well with the theoretical model down to ~7 K, below which other effects such as Coulomb interactions[97] cause deviation from the model defined by equation (3.2) (inset of fig. 3.2b and fig. 3.2c).

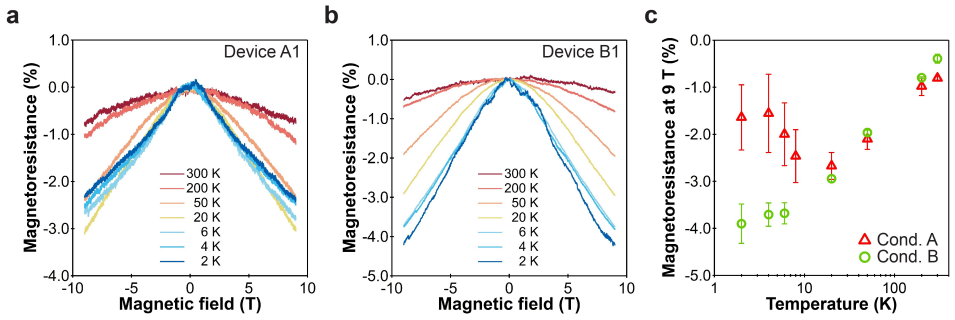

Figure 3.3: Magnetoresistance of single NT-3DFG
Magnetoresistance as a function of applied perpendicular magnetic field acquired from devices (a) A1 and (b) B1. (c) Magnetoresistance at 9 T as a function of device temperature. Data is presented as mean ± standard deviation (n = 3).

In the presence of magnetic fields up to ±9 Tesla perpendicular to the length of the nanowire, NT-3DFG exhibits negative magnetoresistance (MR) at all temperatures between 2 and 300 K (fig. 3.3a,b). We attribute the observed negative MR to a VRH-based mechanism in the free-standing graphene flakes.

VRH-based electron transport in the presence of a magnetic field can result in an anomalously large negative MR due to an orbital quantum interference effect, as first described by Ioffe and Spivak[98]. Physically, a long-distance hop comprises multiple parallel paths, each with intermediate scattering sites. In the absence of a magnetic field, these multiple paths interfere destructively, providing an extra contribution to the resistance. Introducing a perpendicular magnetic field suppresses this destructive interference, resulting in a negative MR[98, 99].

We note that this effect is physically distinct from often cited mechanism of weak localization[100] which is typically only relevant at low temperatures and low magnetic fields compared to what we observe in NT-3DFG devices[101, 102].

Although the predicted magnitude of negative MR associated with VRH can be quite large (up to $\sim 70\%$)[98], the observed MR is relatively weaker in our devices due to parallel conduction through the graphitic shell. Furthermore, we find that there is a distinction in the temperature dependence of the MR between the two synthesis conditions (fig. 3.3c). While Condition B devices show a progressively stronger negative MR at lower temperatures, Condition A devices show a maximum magnitude of negative MR at $\approx$20 K, below which the MR was observed to become weaker.

To understand this behavior, we consider the monotonic case first. As Condition B devices are cooled down, the VRH resistance component becomes extremely insulating relative to the resistance of the graphitic shell (R_{VRH}(2 K) = 1.66 $M\Omega$, R_{VRH}(300 K) = 61.59 $k\Omega$, and R_0 = 26.13 $k\Omega$ for device B1). The more insulating the VRH component, the stronger is the negative MR[98]. Hence, the observed negative MR becomes stronger upon cooling (fig. 3.3c).

In Condition A devices, the resistance is dominated by the VRH mechanism since R_0 is much greater than R_{VRH} over the majority of the measured temperature range (R_{VRH}(2 K) = 5.05 $M\Omega$, R_{VRH}(300 K) = 30.16 $k\Omega$ and R_0 = 1.71 $M\Omega$ for device A1). The combined negative MR at 9 T and 300 K from the VRH component is $\approx 1\%$.

As the temperature is lowered, R_{VRH} (T) increases, increasing the magnitude of negative MR up to $\approx 3\%$. However, at the lowest temperatures, R_{VRH} increases to $\approx 5M\Omega$, larger than the resistance of the graphitic channel R_0. Thus, the MR effect is obscured by the lower resistance path through the graphitic shell. Therefore, there is an intermediate temperature, T*, for which the negative MR effect is the strongest in the Condition A devices, as observed near 20 K in fig. 3.3c.

From the total measured MR at 2 K and 9 T for device A1, the VRH component of resistance is estimated to be R_{VRH}(9 T) $\approx$ 3.3 $M\Omega$. Although shunting through the graphitic shell reduces the magnitude of the measured MR, the MR resulting from pure VRH is expected to be significantly larger, MR(9 T) $\approx (3.3M\Omega - 5M\Omega)/5M\Omega = -34\%$.

For optimal synthesis conditions, it may be possible to reduce the formation of the graphitic shell, enabling magnetic field sensing applications with NT-3DFG dominated by VRH.

3.5 Concluding Remarks

We demonstrate synthesis of NT-3DFG, a polycrystalline 3D arrangement of 2D graphene flakes along a 1D SiNW. Using templated fuzzy graphene as a model, we establish the underlying electron transport mechanisms in complex multi-dimensional

graphene based nanostructures. Electron transport in templated fuzzy graphene occurs through parallel channels formed by the graphitic shell (metallic transport) and the free-standing graphene (VRH-based transport).

In addition, the material exhibits negative MR at all temperatures, irrespective of flake size and density, which we attribute to a VRH-based interference mechanism distinct from weak localization. While the observed MR magnitudes are on the order of -1% to -4%, parallel transport through the graphitic shell suppresses potentially large negative MR behavior in the free-standing graphene flakes. Our study opens new avenues for synthesizing and characterizing 3D arrangement of 2D materials to understand electron transport in multi-dimensional nanostructures.

Chapter 4

Magnetic proximity effect in graphene

Graphene's excellent electrical properties including a high carrier mobility have already been alluded to. As far as magnetic properties go, graphene is intrinsically non-magnetic. There are two primary motivations to create a long range magnetic order in graphene. Firstly from an applications standpoint, having a magnetic system that possesses excellent electrical properties has applications in spin based logic and memory devices[103]. Secondly from a fundamental physics standpoint, graphene has been predicted to host a higher temperature QAHE upon the addition of magnetism and spin orbit coupling. This chapter discusses the idea of magnetizing graphene via a proximity effect from a neighbouring vdW magnetic layer.

An obvious technique to magnetize graphene is to dope it with magnetic atoms such as iron or cobalt[104]. However when adsorbed, these adatoms tend to cluster on the graphene surface and act as scattering agents for the charge carriers. As a result, the electrical properties of graphene are severely degraded. An approach is needed to create magnetic order in graphene that preserves graphene's electrical properties.

The discovery of 2D vdW magnets and vdW heterostructures provides an alternative route towards magnetizing graphene by means of a magnetic proximity effect. We will discuss this in greater detail in section 4.1.4. But in brief, creating a vdW heterostructure of graphene and a vdW magnet would lead to (a direct or indirect) hybridization between graphene's π orbitals and the proximal transition metal magnetic d-orbitals. Prior results between graphene-hBN heterostructures have shown that such hybridization of graphene's π orbitals does not compromise graphene's electronic properties[31, 32].

4.1 The quantum anomalous Hall effect

4.1.1 Introduction to the quantum anomalous Hall effect

The quantum anomalous Hall effect (QAHE) is similar to the QHE in that electrons in bulk surface are localized while dissipation free current is carried along the sample edges. It is the final piece in the quantum Hall trio, also comprising the quantum spin Hall effect (QSHE)[105].

The QHE requires the presence of a large out of plane magnetic field. This magnetic field causes electrons in the bulk surface of the 2D layer to undergo closed cyclotron orbits, localizing the electrons. At the edges however, there exists a large, steep potential barrier between the 2D material and vacuum. The electrons would require an extremely high energy to overcome this work function in order to escape the 2D layer. Thus, the electrons reflect off of this large potential and traverse along the edges of the sample. These edge modes are chiral, in that the directions in which the electrons traverse (say clockwise) is same for both spin up and spin down electrons, and determined purely by the direction of the external magnetic field. This is shown in the left panel of fig. 4.1. Since the bottom edge (left propagating electrons) and top edge (right propagating) are spatially separated by a large distance $\sim \mu m$, it is highly unlikely that an electron will backscatter. Thus, these edge modes are protected against backscattering and carry dissipation free current.

The QSHE does not require an external magnetic field. The mechanism of the QSHE is discussed in more detail in sec. 4.1.3. Briefly, the QSHE requires the presence of spin orbit coupling (SOC), which is a coupling between an electron's spin and its momentum. The QSHE results in edge modes that are *helical*, that is electrons with opposite spins traverse along the edges in opposite directions, due to SOC. The QSHE is thus more susceptible to backscattering if the scattering event flips the spin of an electron.

The QAHE is similar to the QSHE in that it does not require an external magnetic field to create a bulk surface gap plus dissipation free edge modes. In addition to the SOC however, the sample possesses intrinsic magnetic order which breaks spin degeneracy. Thus, by positioning the Fermi level between the two Zeeman split spin bands, we can populate only one of the two spin bands. The result is *spin polarized* edge modes, whose direction of propogation is determined by the sample magnetization. Since there exist edge states with a single spin, they thus traverse in the same direction and are thus protected against backscattering, similar to the QHE.

The QAHE has now been experimentally realized in thin films of topological insulators $(Bi,Sb)_2Te_3$ that have been precisely doped with Cr or V atoms[106, 107]. The transport signature of the QAHE is shown in Fig. 4.2. At zero external field, the longitudnal resistance $\rho_{xx} = 0$ and the transverse resistance is quantized: $\rho_{xy} = \pm h/e^2$ similar to the $\nu = 1$ state in the QHE. A hysteresis loop is present at a coercive field

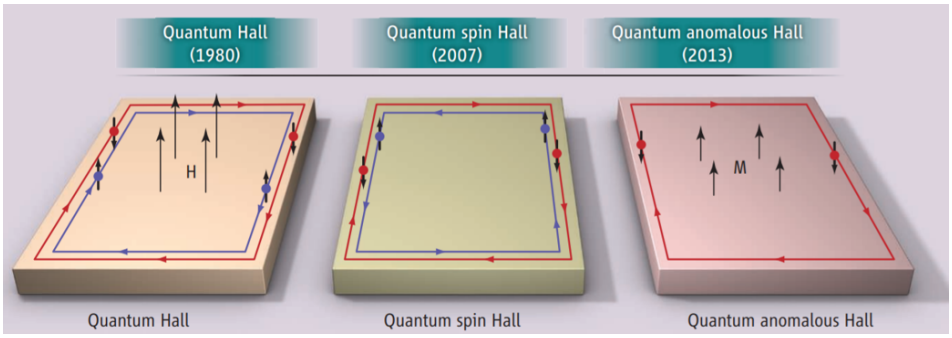

Figure 4.1: The quantum Hall trio
From left to right: The QHE, the QSHE, and the QAHE. From [105]

$\sim \pm 1$T at which the sample magnetization flips, giving rise to a peak in ρ_{xx} and a step up/down in ρ_{xy}. So far, this effect has only been observed at very low temperatures. The data shown in fig. 4.2 was procured at 25 mK. At higher temperatures, increased scattering from the magnetic Cr or V dopants makes the QAHE disappear. The Hall angle defined as $\theta_H = \arctan(\rho_{xy}/\rho_{xx})$ is 89.99° at 25 mK, and shrinks to 30° by 2.5 K.

To realize the QAHE at higher temperatures, an approach different from magnetic impurities is required to introduce magnetism into the system.

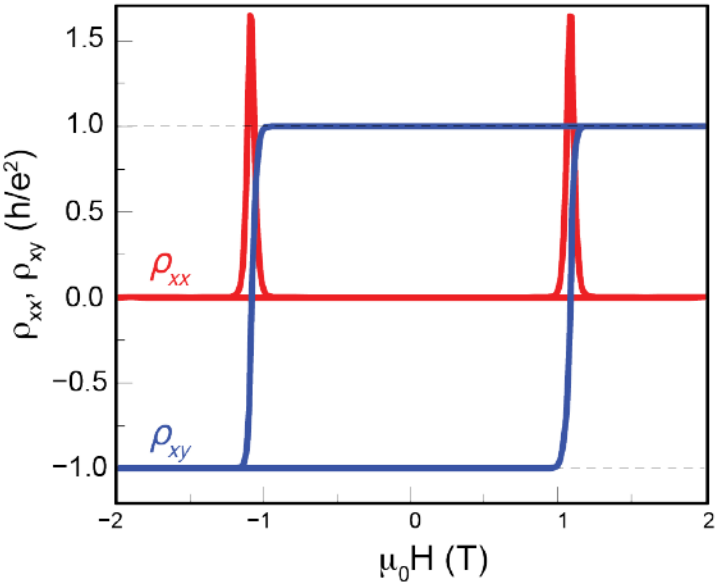

Figure 4.2: Experimental observation of the QAHE in V-doped $(Bi,Sb)_2Te_3$
ρ_{xx} is zero except for peaks at $B = \pm 1\ T$ where the magntization flips. ρ_{xy} is quantized to $\pm h/e^2$. Measurement was carried out at 25 mK. From [107]

4.1.2 Ingredients of the quantum anomalous Hall effect

Before introducing how the QAHE can be realized in graphene, we first introduce some of the ingredients that go into realizing the QAHE in graphene.

Magnetic exchange field

Let us consider the following system where we place graphene on top of a ferromagnetic monolayer. We turn on an external magnetic field **B**. For simplicity, just to introduce the magnetic exchange, the only exchange interactions we consider are those that involve one spin on graphene and the other spin on the ferromagnetic monolayer. We thus write the Hamiltonian for such a system as

$$\hat{H} = -\sum_{ij} J_{ij}\, \mathbf{S}_i \cdot \mathbf{S}_j \;+\; g\mu_B \sum_j \mathbf{S}_j \cdot \mathbf{B} \tag{4.1}$$

where the exchange constants J_{ij} are positive due to ferromagnetism and $\mathbf{S_i}$ and $\mathbf{S_j}$ indicate spins at sites i and j that are respectively on the ferromagnetic monolayer and graphene respectively. The first term is the energy associated with a Heisenberg exchange interaction, and the second term is the Zeeman energy due to the external magnetic field. We have ignored additional terms that arise from the ferromagnetic monolayer itself. We have also ignored exchange interactions that involve both spins being on graphene sites.

We can rewrite the first term by summing over all the sites i. We define an effective magnetic exchange field (MEF) that spins $\mathbf{S_j}$ on graphene experience.

$$\mathbf{B}_{MEF} = -\frac{2}{g\mu_B} \sum_i J_{ij}\, \mathbf{S}_i \tag{4.2}$$

which means we can rewrite equation 4.1 as

$$\hat{H} = g\mu_B \sum_j \mathbf{S}_j \cdot (\mathbf{B}_{MEF} + \mathbf{B}) \tag{4.3}$$

Thus, the MEF is a "pseudo magnetic field" that makes it easier to visualize the effect of a large number of spins from the ferromagnetic monolayer on a single graphene spin. It has no orbital effects that arise from an electron's charge such as Lorentz force scattering.

Spin orbit coupling

We consider two types of spin orbit effects here, namely the Ising SOC and the Rashba SOC. A third SOC, the Kane-Mele SOC will be introduced in the following section for graphene.

Ising SOC manifests in systems that have a broken in-plane inversion symmetry, resulting in an in-plane electric field **E**. In 2D materials, the electron momentum

$\mathbf{k}$ is naturally in-plane. We know from classical electrodynamics that an electron travelling with a velocity $\mathbf{v}$ in an electric field $\mathbf{E}$ experiences a magnetic field

$$\mathbf{B} = -\frac{\mathbf{v} \times \mathbf{E}}{c^2} \tag{4.4}$$

Thus, for the above system, there exists an effective *Ising* spin orbit field $\mathbf{B_{so}} \propto (\mathbf{E} \times \mathbf{k})$ that points in the out of plane direction. Ising SOC plays the role of pinning the electron spins perpendicular to the plane of the vdW material. An example of a material system where Ising SOC is at play is in intrinsic vdW superconductors $NbSe_2$ and TaS_2[16, 17, 3]. In these superconductors, the pinning of electron spins to the out of plane direction makes superconductivity very robust to in-plane magnetic fields.

Rashba SOC results from broken out of plane inversion symmetry, such as when a vdW material is placed on a substrate. This gives rise to an electric field term $\mathbf{E} = E\,\hat{\mathbf{z}}$. As a result, Rashba SOC plays the role of canting the electron spins in the *in-plane* direction. Thus, the Ising and Rashba SOC effects are competing effects.

4.1.3 Intrinsic spin orbit coupling in graphene

The simple tight binding Hamiltonian for graphene considering nearest neighbour hopping is given by

$$\hat{H} = -t \sum_{<ij>,\alpha} \hat{c}^{\dagger}_{i\alpha}\, \hat{c}_{j\alpha} \tag{4.5}$$

Here t is the hopping amplitude, $\hat{c}^{\dagger}_{i\alpha}$ ($\hat{c}_{i\alpha}$) operator creates (destroys) an electron at site i with spin α. $<>$ denotes that the sum is performed over sites i, j that are nearest neighbours. Solving this tight binding model for graphene yields the familiar dispersion relation at the $\mathbf{K}$, $\mathbf{K'}$ points with linear valence and conduction bands touching: $E(\mathbf{q}) = \pm\hbar v_F\,|\mathbf{q}|$. These bands are fourfold degenerate because of the spin (twofold) and valley (twofold) degeneracies.

A spin orbit term that can be added to the Hamiltonian whilst preserving spatial inversion and time reversal symmetries is the Kane-Mele SOC Hamiltonian[108]

$$\hat{H}_{KM} = \Delta_{KM} \sum_{i,\alpha} \hat{c}^{\dagger}_{i\alpha}(\hat{\sigma}_z\, \hat{\tau}_z\, \hat{s}_z)\, \hat{c}_{i\alpha} \tag{4.6}$$

$\hat{\sigma}_z$, $\hat{\tau}_z$, $\hat{s}_z$ are the usual Pauli matrices. $\hat{\sigma}_z = \pm 1$ describes states on graphene's $A(B)$ sublattice, $\hat{\tau}_z = \pm 1$ describes states on graphene's $K(K')$ valleys, and $\hat{s}_z = \pm\,1$ denotes electron spin pointing in the $\pm Z$ direction.

$\hat{\sigma}_z$ is odd under parity, but preserves time reversal symmetry. $\hat{\tau}_z$ is odd under both parity and time reversal. $\hat{s}_z$ is even under parity but odd under time reversal. As a result, $\hat{\sigma}_z\hat{\tau}_z\hat{s}_z$ preserves both parity and time reversal symmetry.

Adding this Kane-Mele SOC term to the Hamiltonian opens up a band gap $2\Delta_{KM}$ in the band structure with $E(\mathbf{q}) = \pm\sqrt{(\hbar v_F q)^2 \; + \; \Delta_{KM}^2}$

This energy gap has opposite sign for an electron at K vs K' point. Thus, traversing from K to K', there is a non-trivial band crossing which is topological in nature, giving rise to a quantized Hall conducance $|\sigma_{xy}| = \frac{e^2}{h}$. Similarly, this energy gap has the opposite sign for electrons with opposite spins. The group velocity $v_g = \frac{1}{\hbar}\frac{dE}{dk}$ implies that under an electric field, electrons with opposite spins will travel in the opposite directions as is illustrated in the middle panel of fig. 4.1. Thus, graphene implicitly houses the QSHE. Note that this gap is different from what would arise out of a term that is proportional to σ_z or s_z. These latter ones would open up a trivial insulating gap by breaking the sublattice or the spin degeneracy respectively.

However, the magnitude of this intrinsic Kane-Mele SOC is quite small $\sim 100\mu eV$. Additionally, the QSH gap is usually easily reduced or completely erased when graphene is placed on a substrate. Doing so adds a Rashba SOC term $\propto (\mathbf{s} \times \mathbf{p})$.

$$\hat{H}_R = \lambda_R \sum_{<ij>,\alpha\beta} \hat{c}^\dagger_{i\alpha} \; (\hat{\sigma}_x \; \hat{\tau}_z \; \hat{s}_y \; - \hat{\sigma}_y \; \hat{s}_x) \; \hat{c}_{j\beta} \tag{4.7}$$

For $\Delta_{KM} > \lambda_R$, the QSH gap reduces in magnitude to $2(\Delta_{KM} - \lambda_R)$, shrinking to zero for $\Delta_{KM} < \lambda_R$[108]. Since the intrinsic SOC gap in graphene is quite small, advances have been made to open up a stronger SOC gap through artificial techniques. For the QSHE, Rashba SOC appears to be detrimental by directly competing with the intrinsic Kane-Mele SOC. In other situations however, it can be helpful, such as in realizing the QAHE in graphene. We address these points next.

4.1.4 Designing the quantum anomalous Hall effect in graphene

In 2010, Z. Qiao et al., theoretically demonstrated that in the presence of a magnetic exchange field and Rashba SOC, graphene could be a platform for realizing the QAHE at a higher temperature[104].

The new Hamiltonian under the presence of both an exchange field and Rashba SOC is given by

$$\begin{aligned} \hat{H}_{QAH} = -t \sum_{<ij>,\alpha} \hat{c}^\dagger_{i\alpha} \; \hat{c}_{j\alpha} \; + \; \lambda_{ex} \sum_{i,\alpha} \hat{c}^\dagger_{i\alpha} \hat{s}_z \; \hat{c}_{i\alpha} \\ + \lambda_R \sum_{<ij>,\alpha\beta} \hat{c}^\dagger_{i\alpha} \; (\hat{\sigma}_x \; \hat{\tau}_z \; \hat{s}_y \; - \hat{\sigma}_y \; \hat{s}_x) \; \hat{c}_{j\beta} \end{aligned} \tag{4.8}$$

The second term corresponds to a magnetic exchange with an amplitude λ_{ex}.

Fig. 4.3 illustrates the changes in graphene's *bulk (surface)* band structure as a magnetic exchange field and Rashba SOC are added to the system. In the absence of either ($\lambda_{ex} = \lambda_R = 0$), eq.(4.8) reduces to eq.(4.5). We end up with degenerate spin

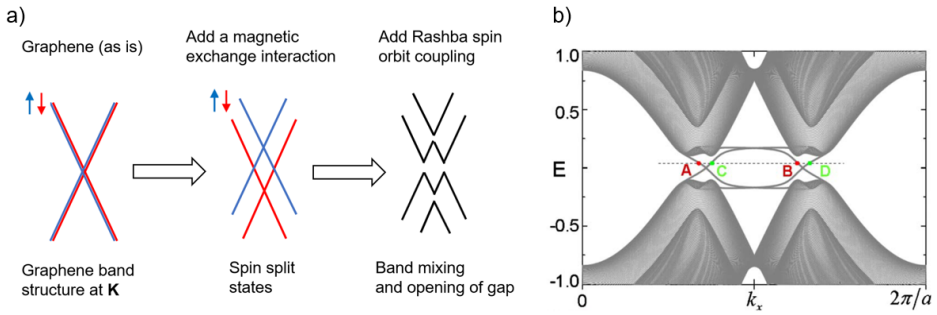

Figure 4.3: Band structure modification of graphene under magnetic exchange and Rashba SOC

(a) Graphene's degenerate spin up and spin down bands are first Zeeman split in energy under magnetic exchange. Adding Rashba SOC mixes the spin bands, that leads to the opening of a non trivial band gap (b) Calculation of the band structure of zigzag edged graphene ribbons showing edge states that reside in the surface gap. Panel b is from [104]

up/down bands at the K/K' points (leftmost panel in fig. 4.3a). Adding a magnetic exchange term (finite λ_{ex}, $\lambda_R = 0$), lifts the spin degeneracy by lowering (raising) the energy of the spin down (up) states (middle panel in fig. 4.3a).

Adding Rashba SOC now mixes the spin up/down states, and opens up a band gap at the K/K' points. The band gap is non trivial, with edge states residing in the energy gap, as calculated by Qiao et al., and shown in fig. 4.3b [104].

The authors calculate the Berry curvature and the Chern number for the system described by (4.8)

$$C = \frac{1}{2\pi} \sum_n \int_{BZ} d^2k \; \Omega_n \tag{4.9}$$

Here Ω_n is the Berry curvature for the nth band and the integral is performed over the entire 1^{st} Brillouin zone. The authors show that the Berry curvature has peaks with the same sign at the K/K' points which gives rise to $C = 2$[104]. Thus, if the Fermi level is tuned such that it lies inside the *bulk* energy gap, the only contribution to transport arises from the gapless *edge* states, giving rise to $\sigma_{xx} = 0$ and $\sigma_{xy} = C\frac{e^2}{h} = 2\frac{e^2}{h}$.

Note that this effect is purely a band structure effect, caused by the simultaneous presence of a magnetic exchange coupling and Rashba SOC. Unlike the QHE, no external magnetic field is required to create Landau level quantization. The quantized edge conduction stems from the topological nature of the bulk surface energy gap. Thus, graphene is a platform to realize the QAHE.

The authors further suggest an experiment to realize this effect which would involve adsorbing Fe atoms on the surface of graphene. While this system could in

principle give rise to the Hamiltonian of eqn. (4.8), metal atoms tend to nucleate into clusters on graphene's surface. Moreover, similar to the thin films of V- or Cr-doped topological insulators, the metal atoms would act as scattering agents even at moderately low temperatures making it difficult to observe the QAHE at higher temperatures. A more promising route towards realizing $\hat{H}_{QAH}$ is to introduce magnetic exchange and SOC by means of proximity effects. This can be achieved by using both ferromagnetic and anti-ferromagnetic materials containing heavy atoms.

Proximity coupling to ferromagnets

J. Zhang et al., theoretically study a vdW heterostructure of graphene on a *monolayer* of $Cr_2Ge_2Te_6$ [109]. $Cr_2Ge_2Te_6$ is a layered vdW ferromagnet that was discussed in section 1.2.4. Additionally, the presence of heavy Te atoms is promising for introducing SOC. Due to the Te-Ge-Cr-Ge-Te vertical layered structure of $Cr_2Ge_2Te_6$(fig. 1.4), the Te atoms would be the closest to the graphene layer ($d = 3.56\ \mathring{A}$). The distance between the C and the magnetic Cr atoms is greater ($d = 5.25\ \mathring{A}$). Thus, it is aptly theorized that the magnetic exchange coupling is not a result of direct hybridization between graphene's π orbitals and Cr $3d$ orbitals. Rather the magnetic coupling is an indirect two step process that is mediated by the Te $5d$ atoms, which themselves are slightly spin polarized by Cr[109].

The authors construct a Hamiltonian similar to $\hat{H}_{QAH}$ in (4.8)

$$\begin{aligned}\hat{H}_{(g-CGT)} = -t \sum_{<ij>,\alpha} \hat{c}^{\dagger}_{i\alpha}\, \hat{c}_{j\alpha} \;+\; \lambda_{ex} \sum_{i,\alpha} \hat{c}^{\dagger}_{i\alpha} \hat{s}_z\, \hat{c}_{i\alpha} \\ + \lambda_R \sum_{<ij>,\alpha\beta} \hat{c}^{\dagger}_{i\alpha}\, (\hat{\sigma}_x\, \hat{\tau}_z\, \hat{s}_y \;-\hat{\sigma}_y\, \hat{s}_x)\, \hat{c}_{j\beta} \\ + \Delta_{KM} \sum_{i,\alpha} \hat{c}^{\dagger}_{i\alpha} (\hat{\sigma}_z\, \hat{\tau}_z\, \hat{s}_z)\, \hat{c}_{i\alpha} \;+\; U \sum_{i,\alpha} \hat{c}^{\dagger}_{i\alpha} \hat{\sigma}_z \hat{c}_{i\alpha}\end{aligned} \tag{4.10}$$

The first three terms are identical to that of (4.8). The authors also include graphene's small intrinsic SOC (4^{th} term). The final term is a staggered sublattice potential that raises (lowers) in energy the A(B) sublattices when graphene is put on a substrate, opening up a small trivial gap at the K/K' points.

The calculations yield a QAH gap of 0.5 meV (6 K), which is 20 times stronger than graphene's intrinsic QSH gap. The larger gap also signifies that the QAHE in this system would be accessible at a temperature that is 20 times higher than the present 300 mK for doped thin films of topological insulators. The nature of the gap is qualitatively identical to that discussed in section 4.1.4. Gapless edge states cross inside the bulk surface energy gap. The Berry curvature has sharp peaks at the K/K' points and results in a Chern number $C = 2$.

Since there is a small mismatch (3%) between the lattice constants of graphene and $Cr_2Ge_2Te_6$, the twist angle between the two layers might be an important factor.

However, the authors predict that the QAHE is more or less independent of this twist angle between graphene and $Cr_2Ge_2Te_6$. While the strength of the non trivial band gap certainly depends on the twist angle, the effect is robust enough that a sizeable gap is present at all twist angles[109].

Proximity coupling to antiferromagnets

By definition, antiferromagnets possess zero *net* magnetic moment. Yet, proximity coupling graphene to an antiferromagnet can lead to a large magnetic exchange coupling. Consider the example of bilayer CrI_3 which is an antiferromagnet with two oppositely aligned ferromagnetic monolayers[20, 23]. When a graphene on bilayer CrI_3 heterostructure is assembled, the ferromagnetic coupling from the top CrI_3 layer will be significantly stronger than that from the bottom CrI_3 layer because of separation between the relevant layers.

Two theoretical proposals for realizing the QAHE in graphene by coupling to an antiferromagnetic vdW material have been reported [110, 111]:

(i) graphene on (111) surface of $BiFeO_3$
(ii) graphene on (001) surface of $RbMnCl_3$.

$BiFeO_3$ is an antiferromagnet with a perovskite structure. Fe atoms reside on (111) atomic planes with alternating (111) planes having oppositely aligned ferromagnetic orders. Thus, the (111) plane closest to graphene should introduce a ferromagnetic exchange coupling in graphene. Indeed, the authors calculate a proximity induced ferromagnetic exchange coupling $\lambda_{ex} = 70\ meV$[110]. Proximity Rashba SOC from $BiFeO_3$ opens up a topological gap $\delta \approx 1.1\ meV$ ($\sim 12.5\ K$), which shares the same characteristics discussed in sections 4.1.4 and 4.1.4 (gapless edge states crossing inside the bulk gap; $C = 2$).

$RbMnCl_3$ is similarly another antiferromagnet with Mn atoms on (001) atomic planes with alternating ferromagnetic order. The authors theorize that putting graphene on (001) terminated $RbMnCl_3$ spin splits graphene's π bands by 280 meV[111]. Proximity Rashba SOC opens up a topologically non-trivial gap $\delta \approx 1.1\ meV$ ($\sim 12.5\ K$) with $C = 2$.

Thus, both systems have been predicted to house the QAHE that should be visible at temperatures lower than 12.5 K, 600 times higher than the present experimental standards.

In summary, three material systems (1 ferromagnetic, 2 antiferromagnetic) have been theoretically considered and predicted to host a higher temperature QAH state by coupling to graphene. It should be pointed out that the route proposed by Z. Qiao et al. [104] in eqn. 4.10 is quite generic and should be realizable by any material that possesses magnetic order and can induce spin orbit coupling in graphene. The discovery of a large number of vdW layered magnets, which contain heavy atoms

provides us with many possible material systems to couple to graphene towards this goal[24].

4.2 Prior experimental results of proximity effects in graphene

Some major experimental results studying proximity effect induced magnetic exchange coupling and/or SOC are discussed in this section.

4.2.1 Graphene-ferromagnet proximity effects

Graphene-EuS

EuS is a 3D ferromagnetic insulator with $T_c = 16\ K$ that crystallizes in a NaCl structure. P. Wei et al. studied the magnetic exchange field (MEF) induced in graphene by EuS [36]. They grew monolayer graphene via CVD on copper, which was then transferred onto an Si substrate. Subsequently, they fabricated a Hall bar device. Lastly, 3-7 nm thick film of EuS was deposited on the graphene via electron beam evaporation at 10^{-8} Torr. The authors measure non-local transport in the graphene devices to quantify the induced MEF.

Non-local transport involves sourcing a current in one part of the device, and measuring its voltage response *outside of the current channel* in another part of the device. In fig. 4.4c, current I is sourced in a vertical branch $2-6$ of a Hall bar, and the voltage response is being measured in the vertical branch $3-5$. If the length/width ratio (aspect ratio) of the device is large enough ($L/W > 3$), then the usual ohmic charge contribution to the signal that varies as $e^{(-\pi L/W)}$ is negligible. By eliminating the ohmic contribution, more subtle contributions to transport can be detected in non-local transport.

In the case of graphene (under zero magnetic field), the non-local resistance $R_{NL} = V/I$ is negligibly small and relatively featureless as the carrier density is varied (fig. 4.4d). When an out-of-plane magnetic field B is turned on, the spin-up and spin-down bands are Zeeman split in energy. When the Fermi level lies at charge neutrality, there is an equal number of electrons (spin-up say) and holes (spin-down) with opposite spins in the device (fig. 4.4b).

Fig. 4.4c illustrates the transport mechanism under such a scenario. When a current is sourced in $2-6$, the electrons and holes are Lorentz scattered by the magnetic field. These charge carriers are thus deflected into the horizontal channel. Since an equal population of electrons and holes is travelling in the same direction, there is a zero net *charge* current in the horizontal channel. However, the contribution to the *spin* current by the two channels is additive, and there is a finite *spin* current. This magnetic field assisted generation of a pure spin current from a charge current has been named the *Zeeman* spin Hall effect (ZSHE)[112]. At the vertical branch

$3-5$, these electrons and holes are now deflected in the opposite vertical directions, giving rise to a finite non-local voltage V_{3-5}, which is illustrated in fig. 4.4d. Thus, the non-local voltage is a sensitive probe of measuring magnetism in graphene systems, and can be applied to detect proximity induced MEF.

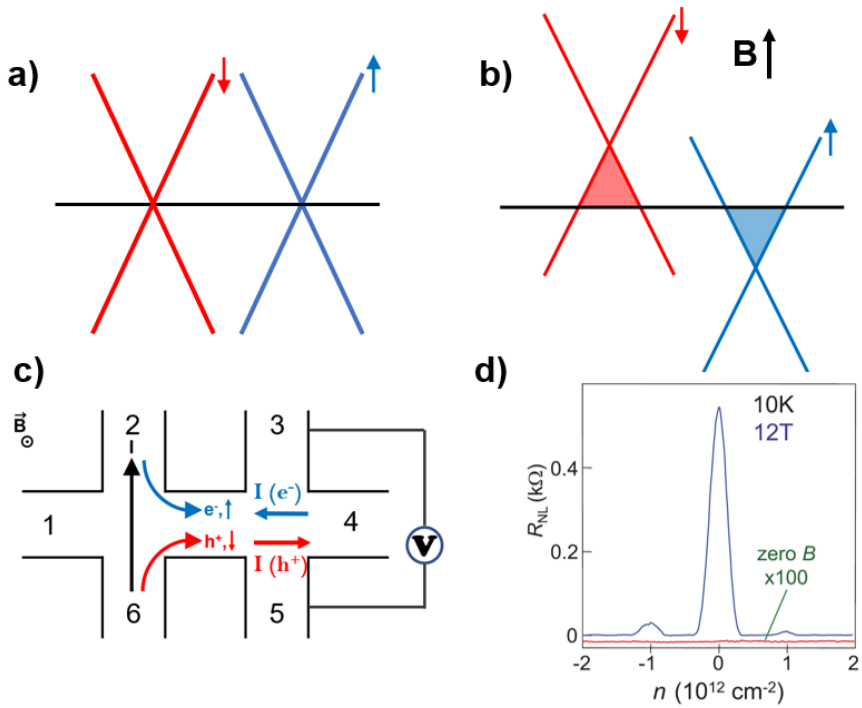

Figure 4.4: Non local transport in graphene Hall bars
(a) Spin degenerate Dirac cones in graphene. Fermi level (black line) is tuned to charge neutrality point. (b) Applying a magnetic field splits the spin bands and creates an equal population of spin down holes, and spin up electrons. (c) Schematic of ZSHE when the bands are aligned as in panel b. (d) A significant non-local resistance develops at CNP under a magnetic field. Panel d is from ref. [112]

In their graphene-EuS devices, P. Wei et al. observed an onset in the neutrality point non-local resistance $R_{NL,D}$ as the device was cooled at 16 K, coinciding with T_c of EuS[36]. Since EuS is an insulator, all features in transport, including any magnetic signatures are characteristics of graphene. The authors also measured similar graphene-AlO_x devices as reference, since AlO_x is non magnetic.

The authors measure $R_{NL,D}$ vs B for both graphene-EuS and graphene-AlO_x devices (fig. 4.5a). The graphene-AlO_x device is relatively featureless, whereas the g-EuS device undergoes two orders of magnitude increase in $R_{NL,D}$. By subtracting the zero field $R_{NL,D}$, the authors compare $R_{NL,D}$ vs B in the two devices and use it to extract a MEF vs B which is plotted in fig. 4.5b. At an external field of 4 T, the exchange coupling between graphene and EuS is $\sim 17\ T$ ($2\ meV$). Thus, the authors

demonstrate a significant MEF induced in graphene by EuS.

There are however a few inconsistencies between the authors' observations and what we might expect out of an MEF. These measurements are performed at 4.2 K, below $T_c = 16$ K of EuS. Thus, even at zero external field, the magnetic moments of EuS should be polarized, and lead to a non zero MEF. The authors however, do not see any increase in their non local signal until $B_{external} \approx 1\ T$ and at $B_{external} = 0\ T$, they have $B_{Zeeman} = 0\ T$.

On the other end of the spectrum, the authors' observations suggest that the MEF continues to increase even at $B_{external} \approx 4\ T$, when the moments of EuS will have long saturated. By our definition of the MEF in section 4.1.2, this should lead to a saturation of the MEF. This is clearly not the case, and this inconsistency is not well understood.

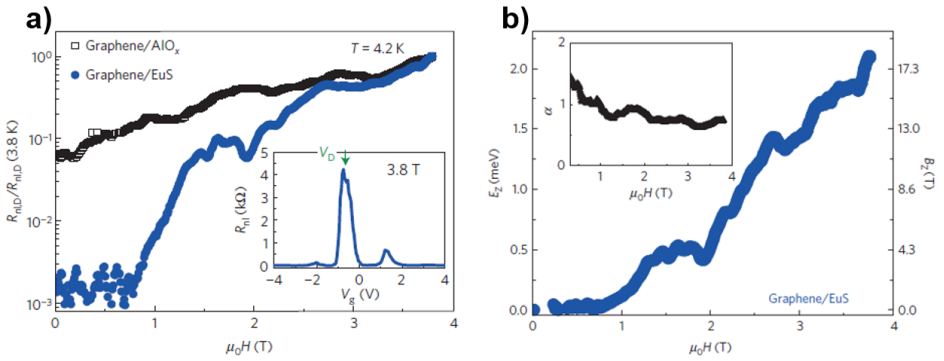

Figure 4.5: Enhanced non local transport in EuS-graphene devices (a) Non-local resistance at CNP vs magnetic field for EuS-graphene and AlO_x-graphene. The former shows a change in $R_{NL,D}$ that is two orders of magnitude greater. (b) Extracted value of magnetic exchange coupling vs external magnetic field. The MEF exceeds 17 T at $B = 4\ T$. From [36]

Even though Eu is a relatively heavy element, there does not appear to be any proximity induced SOC in graphene. Local resistance measurements vs B indicate a weak localization peak at $B = 0$, which is a clear sign of *absence* of any SOC effects. The absence of SOC is not yet understood.

Graphene-YIG

Yttrium iron garnet (YIG), chemical formula $Y_3Fe_2(FeO_4)_3$ or $Y_3Fe_5O_{12}$ is a 3D *ferrimagnetic* insulator. A ferrimagnet contains magnetic moments pointing in opposite directions, but in unequal numbers. Due to a high Curie temperature (T_c= 550K), YIG has magnetic order and can induce ferromagnetic exchange coupling at room temperatures.

Z. Wang et al. fabricated graphene Hall bar devices on Si and transfered them onto $\sim$ 20 nm thick YIG films[37]. A metal top gate was subsequently evaporated

to tune graphene's carrier density. The authors observe the anomalous Hall effect (AHE) in graphene transport at all measured temperatures ($T_{max} = 250K$) as shown in fig. 4.6. YIG being an insulator does not shunt current away from graphene, and the transport characteristics are arising solely from the graphene layer. The anomalous Hall resistance R_{AHE}, linearly rises with magnetic field and saturates at $\sim 230\ mT$, correlated with the saturation field for YIG. The presence of AHE indicates that YIG induces both a MEF and SOC in graphene.

On the negative side, their anomalous Hall conductivity $\sigma_{AHE} \approx 7\ \mu S \approx 0.09 * (2e^2/h)$ is over 10 times smaller than the predicted quantized Hall conductivity for graphene. This is caused due to broadening from disorder that is greater than the topological band gap δ. This is not surprising, since the quality of device is on par with graphene on Si devices with mobility $\mu \sim 6000\ cm^2/V.s$ due to the rough surface of the 3D YIG. Thus, utilizing 2D magnets and assembling an all vdW heterostructures with atomically flat layers is a more promising approach towards realizing the QAHE in graphene.

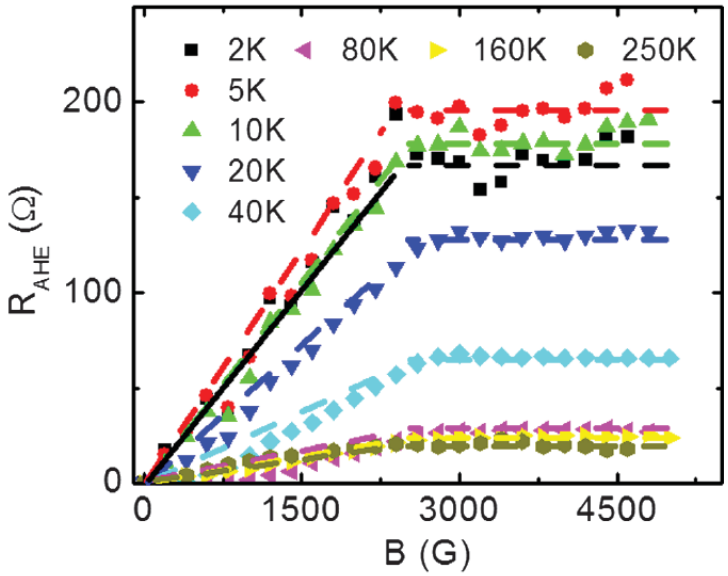

Figure 4.6: Anomalous Hall effect in graphene-YIG
The anomalous Hall resistance saturates at the saturation field of YIG around 250 mT at all temperatures. From ref. [37]

4.2.2 Graphene-antiferromagnet proximity effects

Two experimental reports coupling graphene to an antiferromagnet exist in literature: both using $RuCl_3$. These are discussed in this section.

Magnetic properties of $RuCl_3$

$RuCl_3$ exhibits a rich, complex phase diagram of magnetic order due to competing magnetic orders. Its Hamiltonian can be approximated as a Kitaev-Heisenberg Hamiltonian[113]

$$H_{KH} = \sum_{<ij>} (K S_i^m S_j^m \ + \ J \ \mathbf{S_i}.\mathbf{S_j}) \tag{4.11}$$

The first term is a ferromagnetic Kitaev coupling term ($K < 0$) with the superscript m denoting the component of spins along the direction of the bond connecting spins $\mathbf{S_i}$ and $\mathbf{S_j}$. $m = 1, 2, 3$ corresponds to three different directions in the ab plane, rotated 120° from one another. Clearly, no stable solution exists that satisfies the pure Kitaev Hamiltonian ($J = 0$), and the spins are in a state of *frustrated* magnetic order. The second term in (4.11) is a Heisenberg exchange term with an antiferromagnetic coupling ($J > 0$)[27].

$RuCl_3$ has a honeycomb structure with Ru atoms octahedrally coordinated to Cl atoms. Each *monolayer* comprises 3 atomic planes: Cl-Ru-Cl. The monolayers are stacked in an ABCABC fashion in bulk. However, defects and structural transformations can change the stacking order to ABAB, which is also stable.

At the lowest temperatures, $RuCl_3$ is a zigzag antiferromagnet with $T_N = 7\ K$ ($14\ K$) for ABCABC (ABAB) stacking[27, 114, 115]. The spins are oriented *in-plane*, in two opposite directions for alternating zigzag edges. The in-plane magnetic anisotropy is quite strong, with the zigzag antiferromagnet order persisting beyond a $9\ T$ magnetic field along the c axis. By contrast, S. Baek et al. demonstrated quenching the antiferromagnetic order with an in-plane magnetic field of $7.5\ T$[116].

Graphene-$RuCl_3$

Mashhadi et al., and Zhou et al. have recently reported results on transport in graphene-$RuCl_3$ devices[117, 118]. Mashhadi et al., fabricated (from top to bottom) hBN-$RuCl_3$-graphene-hBN devices. The first observation is that the devices exhibit unnaturally low resistances $\sim 5\ \Omega$, about 3 orders of magnitude smaller than what is expected from graphene. Measuring magneto-transport, the authors observe Shubnikov-de Haas (SdH) oscillations with two different frequencies, corresponding to two different *hole* densities. Hall resistance R_{xy} has a non-linear behaviour near $B = 0$, indicate the simultaneous presence of *both* electrons and holes, however.

Based on a theoretical model, the authors suggest spin-split hybridization of graphene's originally degenerate spin bands with those of $RuCl_3$. Due to the large work function difference between graphene and $RuCl_3$, the valence bands at the Fermi level hybridize with the low energy $RuCl_3$ bands that are spin split due to the antiferromagnetic nature of $RuCl_3$. The hybridization gives rise to two distinct Fermi pockets of spin-up and spin-down holes in graphene, with slightly different sizes, cor-

responding to hole densities of $\sim (1.75 - 1.85 \times 10^{13})\ cm^{-2}$. The electrons have an open Fermi countour, hence do not contribute to SdH oscillations[117].

As a function of temperature, the authors notice an upturn in device resistance around $T \sim 10\ K$. They also find a peak in the fast Fourier transform (FFT) amplitude of the SdH oscillations around $7\ K$. Both of these observations are likely signatures of the onset of an antiferromagnetic transition at T_N. These observations do not necessarily imply a magnetic order in graphene, and probably result from the underlying $RuCl_3$ flake.

Zhou et al., fabricated $RuCl_3$-graphene devices on Si. By varying the back gate voltage, they also observe qualitative behaviour that is consistent with graphene, but with device resistances $\sim 10 - 50$ times smaller in magnitude than expected. The low resistance on their device is attributed to parallel conduction through layers of $RuCl_3$ that are at the graphene-$RuCl_3$ interface. While $RuCl_3$ is a Mott insulator, the large work function difference between graphene and $RuCl_3$ should lead to a large charge transfer from graphene into $RuCl_3$ near the interface. These extra electrons in $RuCl_3$ would cause it to become conducting, giving rise to a second transport channel which would lower the resistance of the device[118].

Hall measurements show positive R_{xy} (at $B > 0$) regardless of the gate voltage, and a nonlinear behaviour near $B = 0$. This supports the picture of two carrier model with the dominant carriers being holes due to the work function difference between graphene and $RuCl_3$. Unlike Mashhadi et al., the authors observe oscillations with only one period in SdH oscillations. Most notably, in R vs T measurements, they observe a peak or a peak-dip features that are gate voltage tunable in the range of $12 - 35$ K. Based on early work characterizing electronic transport in magnetic metals and semiconductors, they attribute the peak (peak-dip) as being a signature of a ferromagnetic (anti-ferromagnetic) phase transition. We will revisit this later on in sec. 5.5.

However, once again, these features are likely an indirect result of the underlying $RuCl_3$ flake as opposed to the onset of a magnetic order in graphene.

4.2.3 Proximity induced spin orbit coupling in graphene

Magneto-transport in graphene-TMD heterostructures

Successful efforts to induce SOC in graphene by proximity effects have utilized vdW heterostructures of graphene with TMDs: MoS_2,WS_2, and WSe_2. Z. Wang et al., demonstrate the presence of SOC using weak antilocalization (WAL) in magneto-transport measurements[33, 34]. WAL is observed in magneto-conductivity as a sharp, narrow peak at zero magnetic field and is a clear signature of the presence of SOC.

Encouragingly, Z. Wang et al. observe signatures of proximity induced SOC in a broad range of graphene-TMD devices. The WAL signature is present in their devices irrespective of

i) Thickness of graphene: monolayer, bilayer, trilayer graphene
ii) TMD material: MoS_2,WS_2, WSe_2
iii) Quality of graphene device: $\mu_{min} \approx 3,000\ cm^2/V.s$ and $\mu_{max} \approx 160,000\ cm^2/V.s$
iv) Carrier density in graphene

The quality of the cleanest g-WSe_2 devices is on par with the highest quality g-hBN devices[34]. The presence of proximity SOC in trilayer graphene is interesting, as it is expected that only the bottom graphene layer in contact with the TMD flake would be significantly modified by proximity interactions. Nonetheless, the proximity SOC effect will eventually disappear as graphene thickness is continually increased.

The WAL effect observed here is distinct from occasional signatures of WAL in as-is graphene at intermediate temperature values $T \sim 10\ K$. Those arise due to electrons that undergo *intra-valley* backscattering, picking up a Berry phase $= \pi$. Indeed, the spin-orbit scattering times observed in the graphene-TMD systems is 10-100 times smaller than those in graphene-SiO_2 and graphene-hBN systems. Additionally, the implicit WAL effect does not occur for bilayer graphene, where the Berry phase is 2π. Thus, the WAL signatures observed in these graphene-TMD systems clearly point to a proximity induced SOC origin. The authors calculate from their data an estimated induced Rashba SOC strength $\lambda_R \approx 10\ meV$[34].

While WAL provides a signature for the presence of SOC, it fails to distinguish between the different *types* of SOC: Rashba, Kane-Mele, Ising ($= \lambda_I \tau_z s_z$). For example both the cases $\{\lambda_R = 10\ meV, \lambda_I = 5-6\ meV\}$ as well as $\{\lambda_R = 15\ meV, \lambda_I = 0\ meV\}$ provide accurate fits to the experimental data. The strength of Ising SOC was recently studied by J. Island et al. in bilayer graphene-WSe_2 heterostructures using magneto-*capacitance*[35].

Magneto-capacitance in graphene-WSe_2

J. Island et al. fabricated symmetric WSe_2-bilayer graphene-WSe_2 dual gated devices, allowing independent control of carrier density n and displacement field D[35]. Using penetration capacitance, they measure the bulk electronic compressibility $\partial n/\partial \mu$ where μ is the chemical potential. The electronic compressibility measurements allow easy visualization of any electronic gaps present in the system.

SOC from WSe_2 opens up a non-trivial gapped phase at charge neutrality ($D = 0$). This gap is different from a conventional band insulator gap that can be opened by applying an electric field. As the electric field is turned on, the gap associated with the non-trivial gapped phase closes adiabatically before reopening. The observations are explained in terms of an Ising SOC term that is induced by the WSe_2

$$\hat{H} = \hat{H}_{BLG} + \ u \sum_{i,\alpha} \hat{c}^{\dagger}_{i\alpha} \hat{\sigma}_z \hat{c}_{i\alpha} \pm \lambda_I \sum_{i,\alpha} \hat{c}^{\dagger}_{i\alpha} (\hat{\tau}_z\ \hat{s}_z)\ \hat{c}_{i\alpha} \tag{4.12}$$

The first term is the Hamiltonian for an unperturbed bilayer graphene system.

The second term is the potential difference between the top and bottom graphene layers with $u = -\frac{d}{\epsilon_{BLG}} D$. Here $d = 0.33\ nm$ is the layer separation, and ϵ_{BLG} is the dielectric constant of bilayer graphene.

The final term is an Ising SOC term that (consistent with 3D inversion symmetry) has opposite signs for the bottom and top graphene layers. In Bernal stacked bilayer graphene the layer number and the sublattice are cross linked. Thus the $\pm$ sign in equation 4.12 can be replaced by $\hat{\sigma}_z$ and the Hamiltonian can be rewritten as

$$\hat{H} = \hat{H}_{BLG} + \ u \sum_{i,\alpha} \hat{c}^{\dagger}_{i\alpha} \hat{\sigma}_z \hat{c}_{i\alpha} + \lambda_I \ \sum_{i,\alpha} \ \hat{c}^{\dagger}_{i\alpha} (\hat{\sigma}_z \ \hat{\tau}_z \ \hat{s}_z) \ \hat{c}_{i\alpha} \tag{4.13}$$

Now, the final Ising SOC term is identical to the Kane-Mele term that was discussed in section 4.1.3, but for monolayer graphene[108].

To estimate the strength of λ_I, the authors apply a perpendicular magnetic field $B_{\perp} = 5\ T$ and study penetration capacitance in the regime where Landau level physics become relevant. The zeroth Landau level of bilayer graphene has eight sublevels, due to sublattice, valley and spin degrees of freedom. This corresponds to filling factor values $\nu \in [-4, +4]$.

In the $|sublattice\ valley\ spin\rangle$ basis, the relative energy of the eight sublevels can be shifted by electric and magnetic fields. For example in the presence of a positive displacement field along $+Z$, it is energetically favourable for an electron to reside in the bottom graphene layer. Similarly the total magnetic field B_{Tot} (perpendicular magnetic field $\mathrm{B}_{\perp}$) direction determines the relative energies of the spin (valley) degrees of freedom.

The moment when two states cross each other in energy, a minimum in the penetration capacitance arises. In pristine bilayer graphene for $\nu = +3$, the levels $|+\ 1\ \downarrow\rangle$ and $|-\ 1\ \downarrow\rangle$ cross at $D = 0$. Similarly for $\nu = -3$, it is the levels $|-\ 0\ \downarrow\rangle$ and $|+\ 0\ \uparrow\rangle$ that cross at $D = 0$.

In the presence of Ising SOC, the levels are further shifted, and the displacement field D^* at which the levels now cross are shifted by a few mV/nm. Using the observed values of D^*, the authors calculate $\lambda_I \approx 2\ meV$. The Landau level spectrum is independent of Rashba SOC, so no predictions for strength of λ_R can be made.

4.3 Concluding remarks

Graphene's 2D nature, high mobility and easily tunable carrier density make it a potentially strong attractive system in which to study novel spin transport. This is an attractive proposal from the point of view of industrial applications, as well as fundamental physics. Adding magnetism and spin orbit coupling, whilst preserving graphene's excellent mobility, make proximity effects a top choice towards realizing the QAHE in graphene.

Proximity induced SOC using TMDs, most notably WSe_2, has been convincingly demonstrated in graphene[33, 34, 35]. It has also been demonstrated that the electronic quality of such devices is on par with the highest quality graphene devices in literature.

While proximity induced magnetism has also been demonstrated in graphene, the adjacent magnetic layers so far have been limited to thin films of 3D ferromagnets[36, 37]. The accompanying roughness and disorder dampen graphene's electrical properties and preclude the observation of the QAHE even under the simultaneous presence of SOC (such as in graphene-YIG in section 4.2.1).

Efforts are needed to proximity induce magnetism in a *purely 2D* vdW heterostructure. So far the only report in this regard has been limited to graphene-$RuCl_3$, where no evidence of magnetic order in graphene was visible[117, 118]. In the following chapter, we report our results from devices comprising graphene and 3 separate vdW magnets: ferromagnetic CrI_3 and $CrSiTe_3$, as well as antiferromagnetic $RuCl_3$.

Chapter 5

Experiments towards realizing the magnetic proximity effect in graphene

Having motivated the need for studying vdW heterostructures of graphene and 2D magnets, we now report on our experimental observations and results in these devices. As has already been mentioned, we will focus on three different 2D magnets: CrI_3, $CrSiTe_3$, $RuCl_3$. The primary characterization tool in our measurements will be variable temperature magneto-transport. We support the transport measurements with low-temperature capacitance and magneto-optical characterization techniques. Each of the three vdW magnets that we use require different strategies for device fabrication due to distinct chemical instabilities towards various precursors.

5.1 Chemical instability of van der Waals magnets

The majority of vdW magnets are chemically unstable under ambient conditions. There are additional concerns of chemical degradation associated with otherwise routine fabrication steps that each material possesses. We first introduce some of those concerns before reporting on experimental procedures designed specifically to circumvent the same.

5.1.1 Degradation of CrI_3

CrI_3 rapidly degrades under ambient conditions. We find exfoliated flakes of CrI_3 to disintegrate under an optical microscope on the time scale of seconds. The primary mechanism for the degradation of CrI_3 is a chemical reaction with moisture in atmosphere[119]:

$$CrI_3 + 6\ H_2O \xrightarrow{\text{Light}} Cr(H_2O)_6^{3+} + 3\ I^-$$

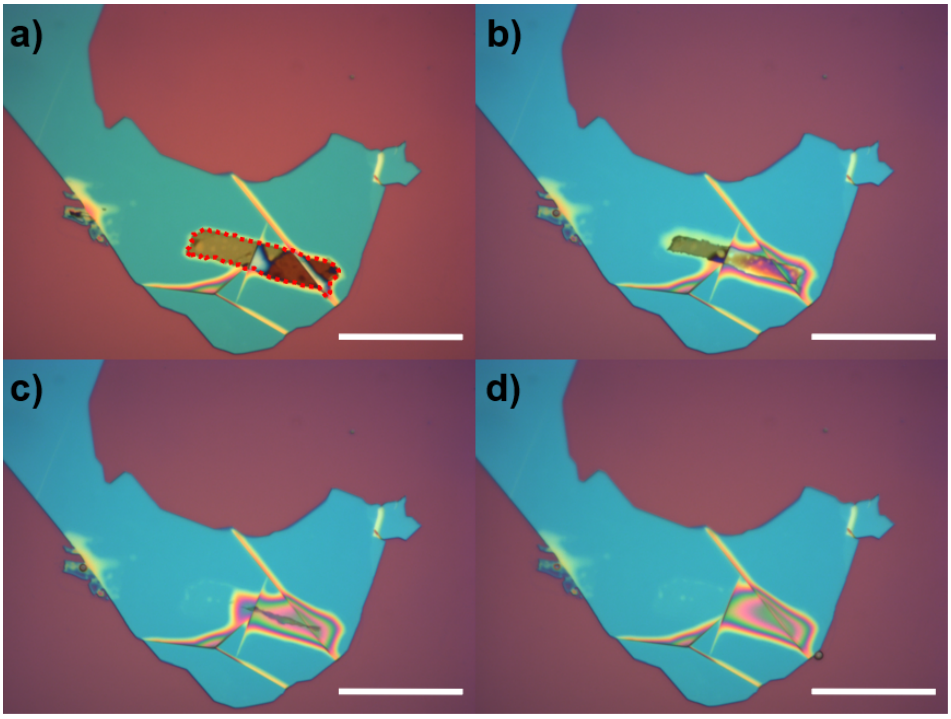

Figure 5.1: Degradation of CrI_3
. The CrI_3 flake (Red outline in panel a) is underneath a thick h-BN flake. The h-BN flake is unaffected, but the the CrI_3 flake disappears completely over a time period of ∼15 seconds. Scale bars are 25 μm

The formation of this aqueous chromium solution is aided by light. We confirm this by observing in real time the degradation of CrI_3 under an optical microscope. The rate of the chemical reaction is greatly accelerated when light is focused on a CrI_3 flake, such as when observing it at high magnification under an optical microscope.

Real time photos of degradation of a CrI_3 flake are shown in 5.1. The photos were taken about 5 seconds apart from one another. Surprisingly, covering a CrI_3 flake with a thick h-BN flake does not prevent degradation of CrI_3. This is the case for the flake presented in fig. 5.1. Since the Si substrate is relatively rough $\sim 1\ nm$, moisture can seep in through the edges of the h-BN "blanket" and react with CrI_3 due to its hygroscopic nature.

To prevent CrI_3 from degrading, it needs to be *encapsulated* in h-BN, i.e., sandwiched between a top and a bottom h-BN flake. The atomically flat nature of h-BN closes air gaps at the edges and thus keeps CrI_3 inert. Nonetheless, in addition to

this protection mechanism, we focus on minimizing the amount of time that CrI_3 is under ambient conditions in our experiments.

5.1.2 Sensitivity of $CrSiTe_3$ to heat

We find obvious optical signatures of $CrSiTe_3$ degradation upon heating at moderate temperatures ($T > 150°C$) over short duration of 2 minutes under ambient conditions. Small "bubbles" appear to form on the surface of $CrSiTe_3$ flakes which are clearly visible under an optical microscope (fig. 5.2). This presents a problem in device fabrication since our electron beam resist, poly methyl methacrylate (PMMA) needs to be heated at $180°C$ for 2 minutes for "baking". We bypassed this problem by devising an alternate fabrication recipe where we bake the resist at 100°C. This relatively lower temperature does not appear to degrade $CrSiTe_3$.

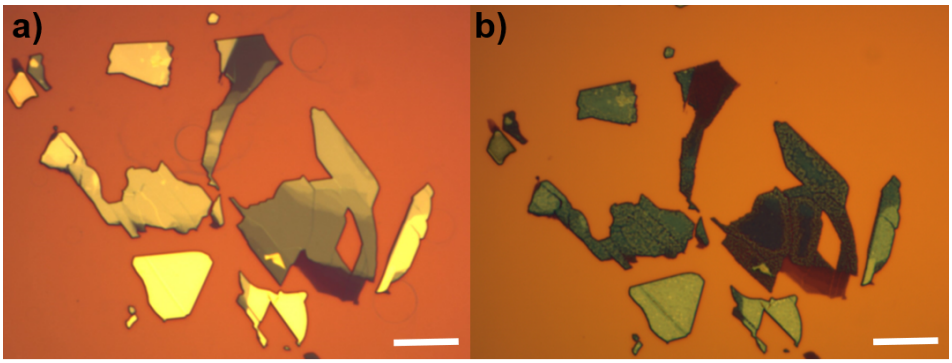

Figure 5.2: Degradation of a exfoliated $CrSiTe_3$ flakes
(a) No obvious signs of degradation are visible after heating to 180°C inside N_2 glovebox for an extended period. (b) $CrSiTe_3$ flakes appear clearly degraded after heating to 180°C for 2 minutes under ambient conditions. Scale bars are 10 μm

Our vdW stacking technique requires us to heat the sample to 180°C for a time > 2 seconds. However, this procedure is performed inside a Nitrogen glovebox (O_2, H_2O concentration ~ 1 ppm), $CrSiTe_3$ does not appear to degrade during this step. We thus theorize that under ambient conditions, especially at elevated temperatures, $CrSiTe_3$ oxidizes to Cr_2O_3 which leads to the formation of bubbles and a change in colour of the flakes.

5.1.3 Sensitivity of $RuCl_3$ to heat

Vacuum annealing is a technique that is routinely utilized to clean the surface of 2D materials and vdW heterostructures. This involves heating the sample at 350°C for 15 minutes under vacuum ($P \sim 1 \times 10^{-6}$ Torr). We find optically, that all flakes of $RuCl_3$ appear to have a relatively stronger purple hue after vacuum annealing (fig. 5.3).

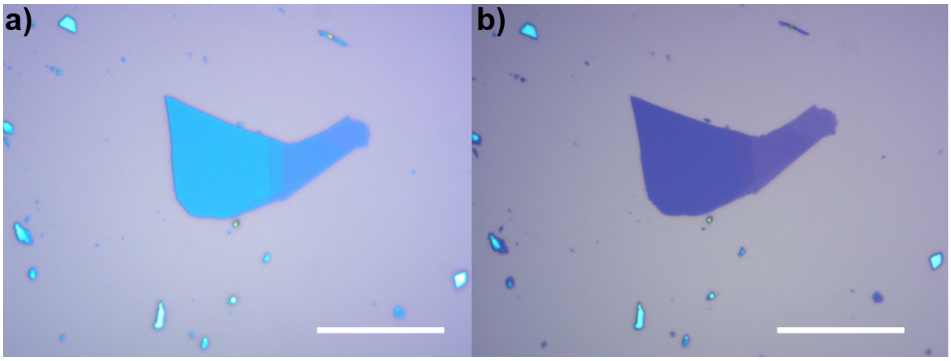

Figure 5.3: Degradation of an exfoliated $RuCl_3$ flake
a) As-is exfoliated flake of $RuCl_3$ b) Optical image of same flake after vacuum annealing for 15 minutes at 350°C shows a clear change in colour. Scale bars are 20 μm. Optical images courtesy of Q. Cao

It is known that $RuCl_3$ can undergo a change in stacking order from ABCABC to ABAB style stacking. It is possible that the observed change in colour simply corresponds to the stacking order of $RuCl_3$ being altered, if the refractive indices of ABCABC vs ABAB stacked $RuCl_3$ are different[120]. We do not investigate this problem in any more detail, simply choosing to avoid heating $RuCl_3$ based devices to high temperatures to work around the issue. In any case this is not a degradation caused due to the presence of O_2 or H_2O since we heat $RuCl_3$ under vacuum conditions.

5.2 Novel techniques to work with chemically sensitive 2D magnets

5.2.1 Glovebox assembly of van der Waals heterostructures

Due to the chemically sensitive nature of vdW magnets under ambient conditions, we work with them inside of an N_2 glovebox. The O_2 and H_2O content are closely monitored and maintained at $\sim$ 1 ppm. Bulk vdW magnets are stored inside the glovebox, and freshly exfoliated each time before assembly of vdW heterostructures. The exfoliation of vdW magnets, as well as the vdW heterostructure assembly, are performed inside the glovebox. For most devices, we cover the vdW magnet with either a top h-BN flake, or completely encapsulate it between two h-BN flakes. The presence of the h-BN capping layer protects the vdW magnet by minimizing exposure to atmosphere when the device eventually needs to be taken out of the glovebox for device nanofabrication.

5.2.2 One dimensional edge contacts to completely encapsulated devices

When our vdW heterostructure has a top h-BN flake completely covering the graphene, we cannot directly access the graphene. The conventional electrical "top" or "areal" contacts are no longer an option. We utilize an idea that was demonstrated by L. Wang et al. and is illustrated in fig. 5.31a for a $CrSiTe_3$-graphene device[121]. The vdW heterostructure is first etched using reactive ion etching. This anisotropic etch technique ends up creating an angular etch profile (see fig. 5.31a) which exposes the edges of graphene[121]. Subsequent metal evaporation then makes an electrical contact to this one dimensional edge (the edge is one atom thick for the case of monolayer graphene). Thus, we can make electrical connections to graphene that are otherwise completely covered in h-BN flakes to protect the underlying vdW magnet.

5.2.3 Contact AFM cleaning of graphene surfaces

We utilize a contact AFM "nanobrooming" technique to clean the top surface of open faced graphene devices post fabrication[122]. Due to the relatively weak adhesion to the graphene sheet, the contact AFM tip is able to move around the particulates away from the active device channel and close to the edges. We demonstrate the effectiveness of this technique on a particularly dirty graphene device in fig. 5.4. By confining the area of our scan to a rectangular region near the device channel, we show that the region of our scan is completely clean, save for one spot in the right half of the rectangle. All the particulates have been pushed to the edge of our scan area, or outside of the graphene Hall bar region.

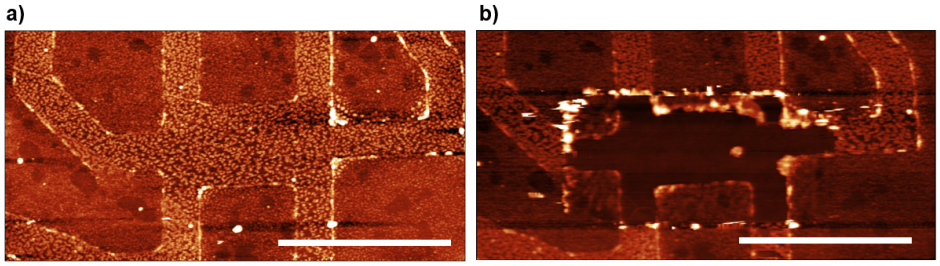

Figure 5.4: Contact AFM cleaning of a graphene Hall bar
AFM scans of the graphene Hall bar (a) *before* and (b) *after* contact AFM cleaning. In panel (b), the particulates can be seen assembled along the edges of the rectangular scan area. Colour scale range is 25 nm in both images. Horizontal scale bars are 3 μm long.

The magnetic proximity effect is extremely sensitive to the quality of the interface between graphene and the 2D magnet. Thus, we also utilize this technique to clean graphene's surface *immediately before* transferring a flake of 2D magnet on top of it.

5.3 CrI_3 - Graphene results

Due to the extreme chemical sensitivity of CrI_3, all our graphene-CrI_3 devices are fabricated in a two step process. This procedure is illustrated in fig. 5.5. Firstly, a working graphene device on h-BN is fabricated into a Hall bar shape. Subsequently, a h-BN-CrI_3 stack is then transferred on top of the graphene-h-BN device inside the glovebox. Prior to the h-BN-CrI_3 transfer, we clean the surface of the graphene-hBN device with contact AFM. We refer to these devices as "type A" devices (device A1, A2 etc.).

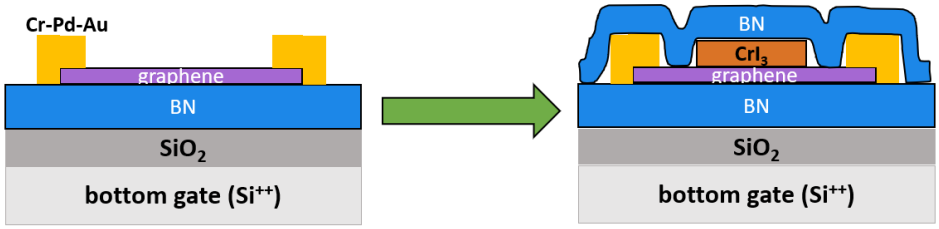

Figure 5.5: Schematic of "type A" h-BN-CrI_3-graphene-h-BN devices
First a graphene-h-BN device is completed. Next the top surface of graphene is cleaned with a contact AFM tip. Lastly, h-BN-CrI_3 is transfered on top of the graphene.

This minimizes the amount of time CrI_3 is exposed to atmosphere, as once the device is completed, we immediately load it into a cryostat post wirebonding. By completing the device nanofabrication prior to CrI_3 transfer, we also do not expose the CrI_3 flake to other potential degradation channels that could result from any of the nanofabrication steps. Lastly, this approach also allows us to measure the graphene-hBN device as is, prior to transfer of CrI_3. We can thus assess the quality of the graphene device before *and* after the incorporation of CrI_3 and look for any changes in transport behaviour that might be indicative of a magnetic proximity effect.

5.3.1 Graphene transport characteristics before CrI_3 transfer

Optical image and AFM scan (measuring *deflection*, not topography) of one such device, device A1 is shown in fig. 5.6. The AFM scan shows that the graphene-h-BN Hall bar device is free of any macroscopic particulates, which have accumulated at the edge of the Hall bar after contact AFM cleaning.

We measure device A1 prior to transfer of CrI_3 on top of the graphene. Fig. 5.7 shows four terminal device resistance measured at 25 mK. The magnetic field is applied perpendicular to the plane of graphene. Varying the gate voltage at zero magnetic field reveals a sharp charge neutrality associated resistance peak around V_{gate} = -2 V indicating that the device is not strongly doped. Mobility calculation reveals a mobility $\mu \sim 110,000\ cm^2/V.s$ consistent with a high quality graphene device.

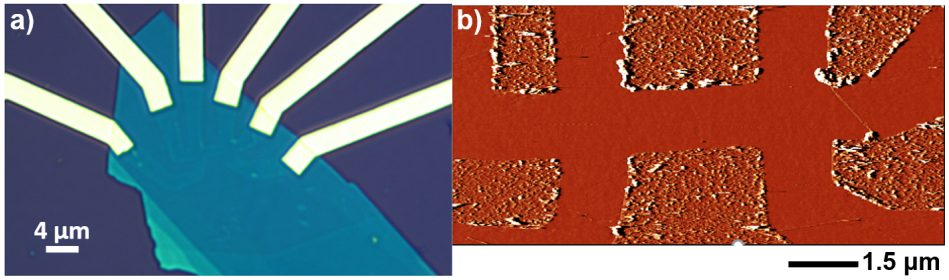

Figure 5.6: Device A1 images
(a) Optical image and (b) AFM scan (deflection) of device A1. The colour scale range is 350 pA

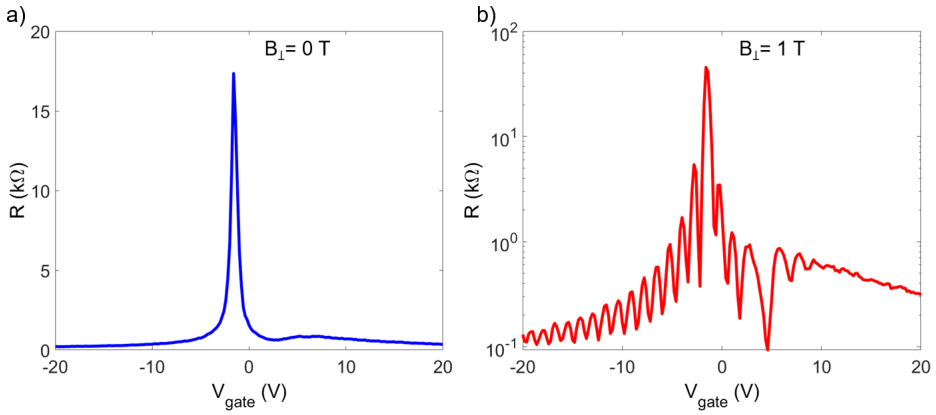

Figure 5.7: Electrical transport in device A1 before CrI_3 transfer
Four terminal device (A1) resistance as a function of back gate voltage at a) $B_\perp = 0$ T and b) $B_\perp = 1$ T (*log scale*). The sharp CNP peak, quantum oscillations and high mobility are indicative of high device quality

We start to see quantum oscillations associated with the QHE by $B \sim 100$ mT corresponding to a quantum mobility $\mu > 100,000\ cm^2/V.s$. Resistance as a function of V_{gate} at $B = 1$ T is plotted in fig. 5.7b. The Landau levels appear better developed on the hole side ($V_{gate} < -2$ V) than on the electron side ($V_{gate} > -2$ V) in device A1.

Fig. 5.8 shows colour maps associated with the quantum Hall regime in the 2D space of gate voltage, and magnetic field. Local resistance R_{xx} reveals the familiar Landau fan comprising alternating regions of zero resistance (Fermi level inside a Landau level) and high resistance (Fermi level in a gap between two Landau levels). Conductivity in the transverse direction, $\sigma_{xy} = \frac{R_{xy}}{R_{xx}^2+R_{xy}^2}$ is shown in fig. 5.8b along with filling factors labeled.

Graphene's Landau levels are fourfold degenerate due to doubly degenerate valleys and spins. Thus, completely filling a Landau level increases the Hall conductivity by

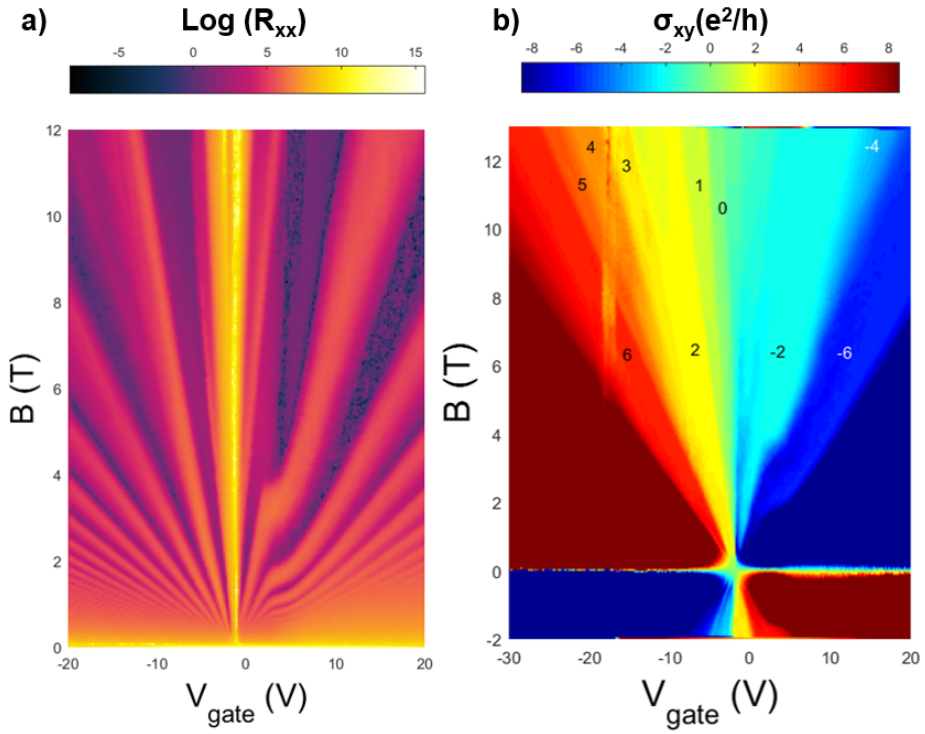

Figure 5.8: Quantum Hall effect and symmetry broken states in device A1 (a) R_{xx} (*log scale*) as a function of magnetic field and gate voltage (b) σ_{xy} (units of e^2/h) reveals symmetry broken Landau level states

$4e^2/h$. The presence of a non zero Berry phase $= \pi$ gives rise to Hall conductivity plateau values $\sigma_{xy} = \nu e^2/h$ where $\nu = \pm 2,\ \pm 6,\ \pm 10$ ...[12, 123].

Under the application of a perpendicular magnetic field, the valley degeneracy is first broken for the zeroeth Landau level. Further increasing the magnetic field also breaks the spin degeneracies. For any other Landau level, it is the spin degeneracy that is first broken, followed by the valley degeneracy [124]. Nonetheless, in these completely symmetry broken Landau level regimes, the visible filling factors are now $\nu = \pm 1,\ \pm 2,\ \pm 3\ \pm 4$ .... In the shown data in fig. 5.8b, we see complete symmetry breaking on the hole side with filling factors $\nu = 1,\ 2,\ 3,\ 4,\ 5,\ 6$ labeled. The presence of full symmetry breaking in our device further highlights its high quality.

5.3.2 Transport characteristics after CrI_3 transfer

After characterizing transport of the graphene implicitly, we unload device A1 from the cryostat and clean the graphene surface one more time with contact AFM. Then, we exfoliate fresh CrI_3 inside the glovebox and transfer an h-BN-CrI_3 heterostructure on top of the graphene (fig. 5.10b). Care was taken to ensure that the CrI_3 flake aligns precisely with the graphene channel.

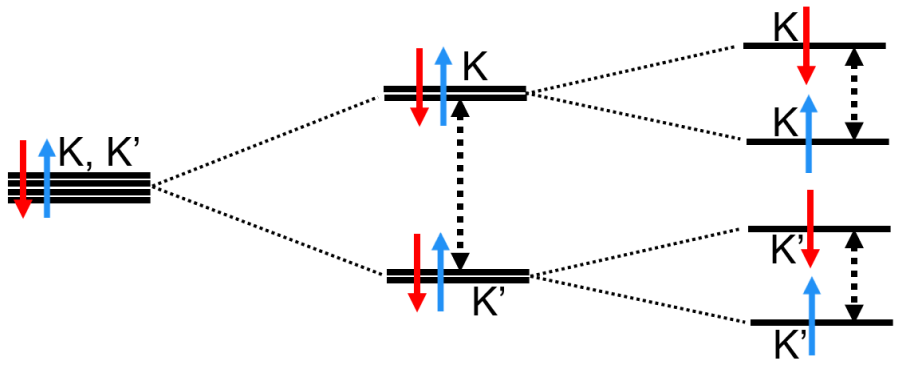

Figure 5.9: Symmetry breaking in the zeroeth Landau level with increasing $B_{\perp}$

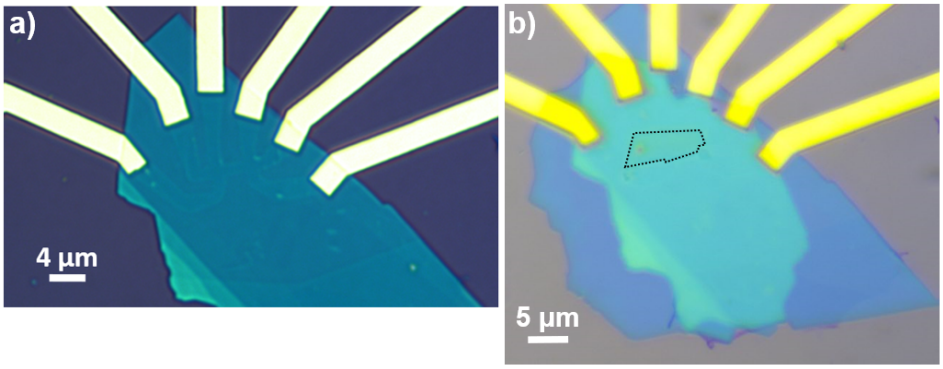

Figure 5.10: Optical micrographs of device A1 before and after CrI_3 transfer a) before and b) after transfer of a top h-BN-CrI_3 heterostructure. The CrI_3 flake has been outlined in black, and is precisely on top of the graphene Hall bar channel, which is not optically visible.

Four terminal resistance of device A1 post CrI_3 transfer is shown in fig. 5.11 versus gate voltage at 0 T and 9 T. There appears to be no signature of the CNP in the device (We push the gate voltage as high as V_{gate} = 100 V and do not observe any signature). Increasing the perpendicular magnetic field to 9 Tesla, we observe a weak positive MR but the transport characteristics appear almost unchanged beyond that. Most notably, we do not observe any quantum oscillations associated with the QHE even at 9 T. This is further highlighted in the colour map of R_{xx} in the B-V_{gate} 2D space in fig. 5.12a. In contrast to the very clear Landau fan in fig. 5.8a before CrI_3 transfer, the resistance profile now is completely featureless, save for a linear increase in R_{xx} with increasing V_{gate} at all B values.

All these observations point to an extremely disordered semiconductor system that is very strongly hole doped (due to the *increase* in resistance as V_{gate} is increased). The lack of observation of charge neutrality up to V_{gate} = 100 V places a lower

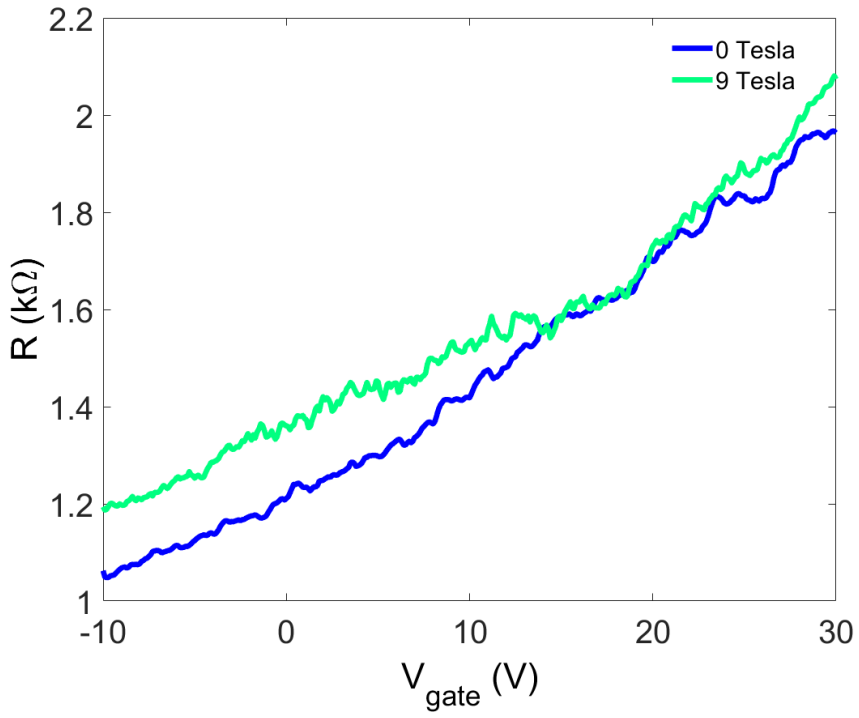

Figure 5.11: Electronic transport in device A1 after CrI_3 transfer
Four terminal resistance vs back gate voltage at $B_\perp$=0 T and $B_\perp$=9 T

estimate on the hole density due to doping as $p > 7.20 \times 10^{12}\ cm^{-2}$. This number is calculated using a simple parallel plate capacitor model with a 285 nm thick SiO_2 dielectric ($\kappa = 3.8$).

Interestingly, we do observe a clear CNP signature in all of our *two-terminal* and *three-terminal* resistance measurements. Fig. 5.12b shows three-terminal resistance for the same device. Contrasting to the four-terminal measurements, there is a clear Landau fan now visible in the three-terminal (as well as two-terminal) measurements.

Explicit traces of three-terminal resistance versus V_{gate} are shown in fig. 5.13 for 0 T and 4 T fields. At 0 Tesla, we observe the familiar Dirac peak near $V_{gate} = 0$ V. At non-zero fields, in addition to the CNP, we observe oscillations associated with the QHE.

This disparity between the four-terminal and three-terminal (and two-terminal) measurements can be understood in the following manner. In a four-terminal measurement, only the resistance of the device channel $R_{channel}$ is measured. In a three-terminal measurement, one of the terminals is common to both sourcing a current, as well as a voltage measurement (Pin 4 in fig. 5.14 for example). Thus, a three-terminal measurement measures the contact resistance of the common terminal, in series with a contribution from the device channel ($R_{common-terminal} + R'_{channel}$). Similarly, in a

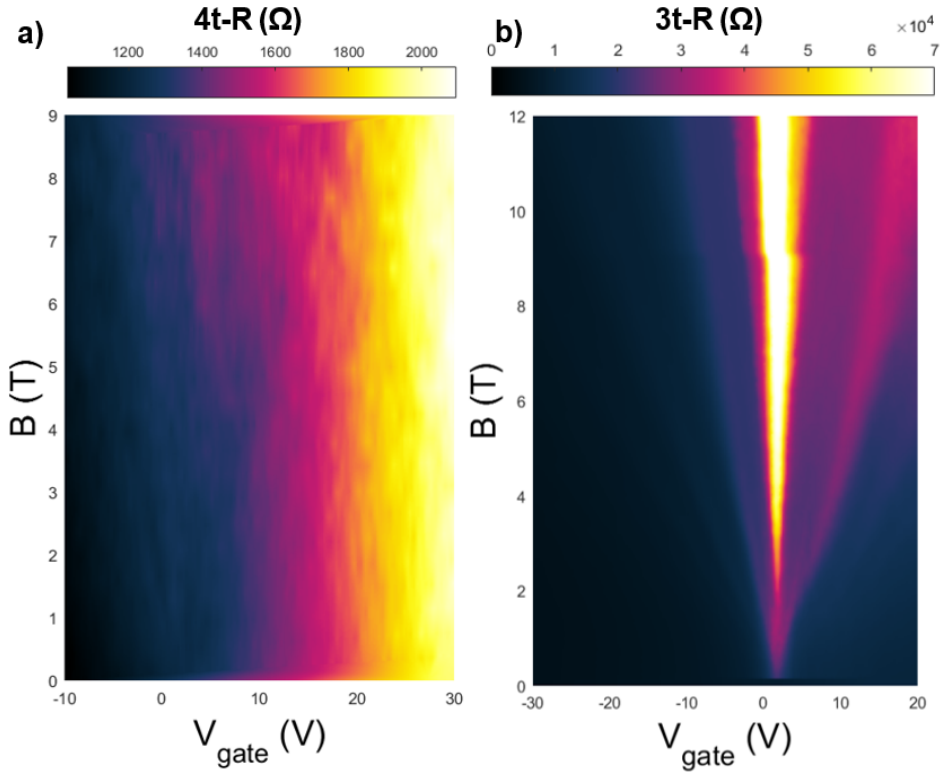

Figure 5.12: Four-terminal and three-terminal transport in device A1 after transfer Colour maps in $B_\perp - V_{gate}$ 2D space of (a) four-terminal and (b) three-terminal resistance in device A1. The three-terminal resistance shows a Landau fan originating near $V_{gate} = 0$ V.

two-terminal measurement, the contact resistances of both the participating contacts are measured ($R_{contact1} + R''_{channel} + R_{contact2}$).

As can be seen from fig. 5.14, the graphene channel is completely covered by CrI_3 (orange shaded region). There are however, other graphene regions outside the channel that are uncovered (white) that are part of the electrical contacts. It is these uncovered regions that still exhibit graphene like behaviour, and are responsible for the Landau fan and quantum oscillations in fig. 5.12b and fig. 5.13.

We believe the degradation of the graphene quality relates to the photocatalytic dissociation of CrI_3 that was discussed in section 5.1.1. Even though we have taken rigorous precautions to encapsulate the device in h-BN flakes, air pockets exist in regions where the top h-BN flake drapes over the thick metal leads (see right panel of figure 5.5). This "tenting" effect leaves open windows for moisture to seep in and react with CrI_3. The degradation forms $Cr(H_2O)_6^{3+}$ and I^- ions which form an electric double layer, with the I^- ions on top of the graphene layer. This close proximity to the negative anions drives electrons away from the graphene, in turn strongly hole

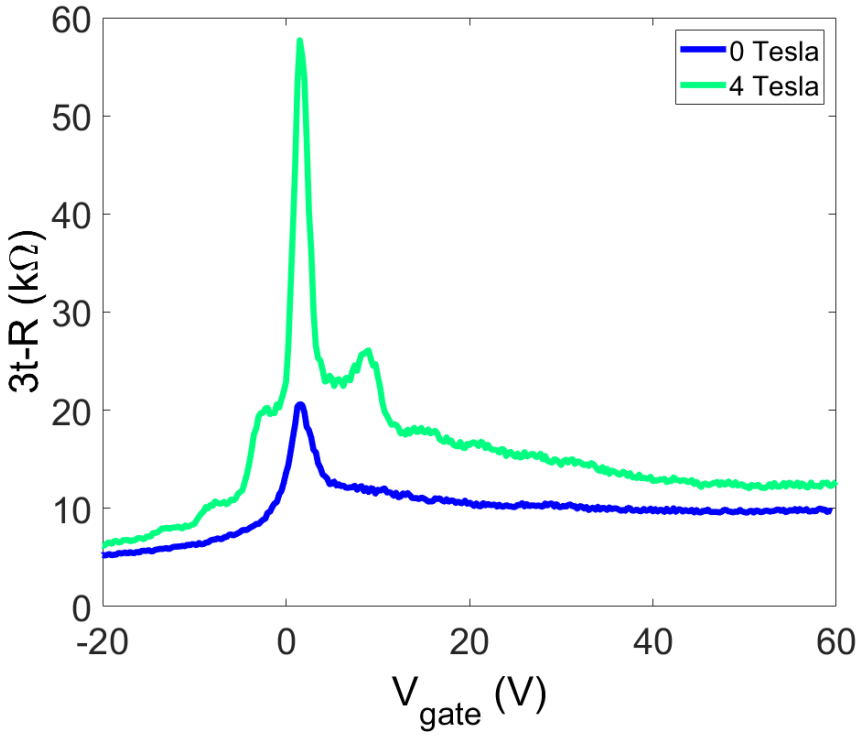

Figure 5.13: Three terminal transport in device A1 after CrI_3 transfer
Three-terminal resistance vs back gate voltage at $B_\perp$=0 T and $B_\perp$=4 T

doping it. Our observations and this explanation are consistent with another report in literature studying CrI_3-bilayer graphene interfaces[119].

AFM scans from the device post CrI_3 transfer corroborate our explanation of highly disordered graphene channel. While having a thick h-BN flake ($\sim$ 15 nm) on top prevents us from clearly observing the interface underneath, it is quite clear that the graphene channel is quite dirty. Regions that were completely clean prior to transfer of CrI_3 now have particulates that are $\sim$ 10 nm in height.

5.3.3 Non local transport in CrI_3-graphene devices

All of our CrI_3-graphene devices show transport characteristics that are nothing like graphene in four-terminal *local* transport. Non local transport, which is a far more sensitive technique, shows no coherent behaviour, with R_{NL} vs V_{gate} scans simply appearing to be noise. We briefly illustrate this for device A1, before and after transfer of CrI_3 in fig. 5.16.

These non local measurements were taken in an improvised measurement setup, with the use of an op-amp feedback and a high input impedance voltage preamplifier. This was done so as to remove any spurious signals that can arise in non local

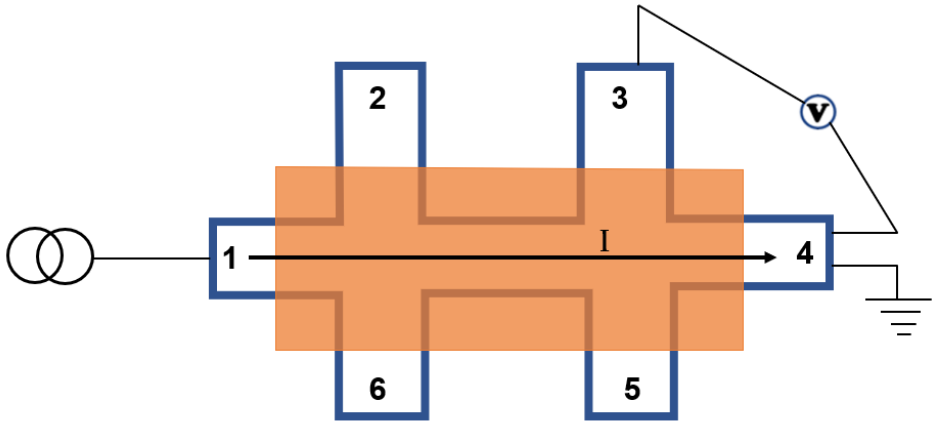

Figure 5.14: Schematic of a three-terminal measurement in device A1 Graphene Hall bar is outlined in blue, underneath an orange CrI_3 flake. Current is sourced at pin 1, and drained at pin 4. The potential drop is measured between pins 3 and 4. In such a measurement, the net measured resistance is a combination of contribution from the graphene channel as well as the contact resistance of pin 4.

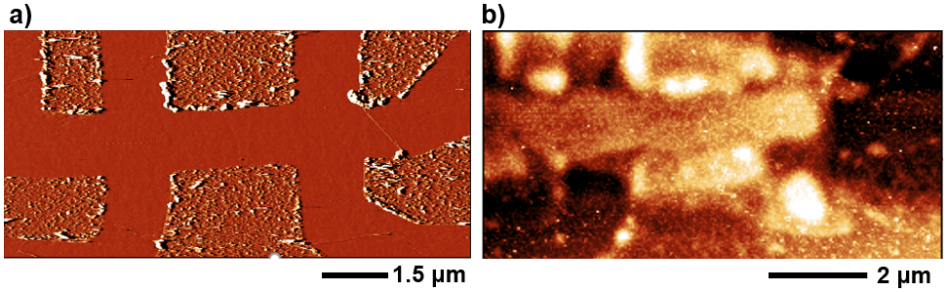

Figure 5.15: Comparing device A1 under AFM pre and post $CrSiTe_3$ transfer AFM scans of device A1 (a) before and (b) after CrI_3 flake transfer. Colour scale range in (a) is 350 pA (deflection) and in (b) is 9 nm (topography).

transport[125]. More details on this are available later in sec. 5.4.3.

Fig. 5.16a shows R_{NL} vs V_{gate} at $B_\perp = 5\ T$ for device A1, prior to transfer of CrI_3 flake. We see the expected behaviour, with a giant non locality at CNP ($\sim 50\ k\Omega$) and additional peaks appearing at half filled Landau levels, where there is an equal population of electrons and holes with opposite flavour (spin or valley)[112]. Peaks corresponding to $\nu = \pm 4,\ +8$ are shown here. To our knowledge, this is the only explicitly reported experimental observation of $\nu = 8$ peak in non local transport that exists in literature.

The exact same trace acquired at $B_\perp = 5\ T$ after CrI_3 transfer appears nothing like graphene's typical non local behaviour (fig. 5.16b). This is in line with our observations of the device in local transport.

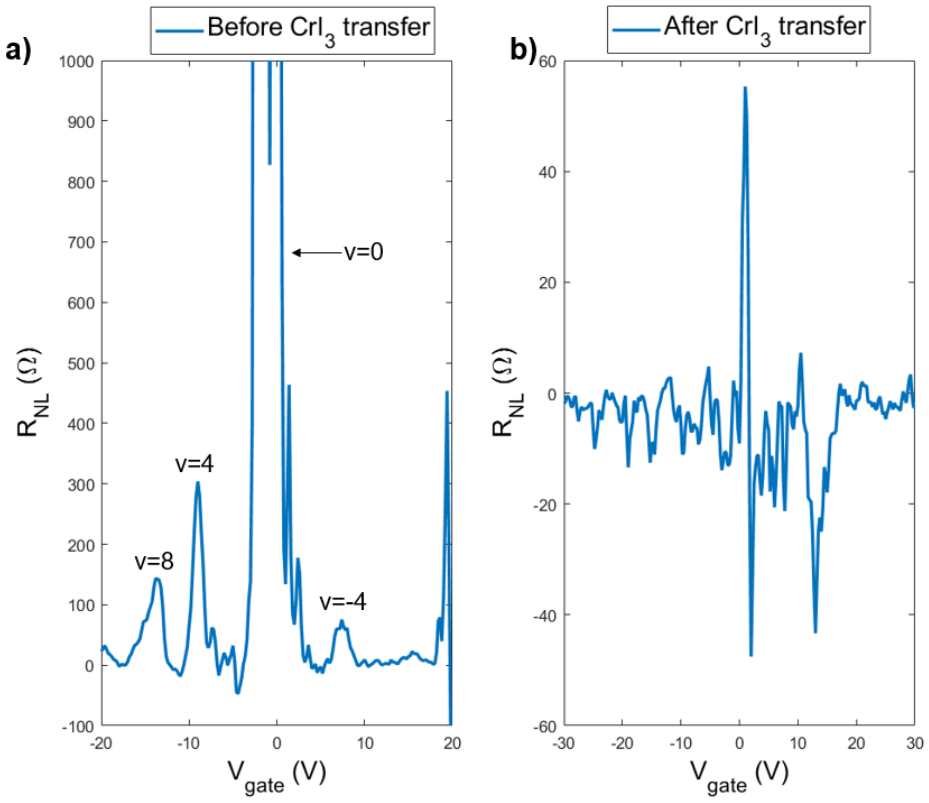

Figure 5.16: Non local transport in device A1
Non local resistance of device A1 at $B_\perp = 5\ T$ (a) Before CrI_3 transfer (T = 52 mK) and (b) After CrI_3 transfer (T = 32 mK)

5.3.4 Other transport characteristics in CrI_3-graphene devices

The results just discussed are reproduced in further devices: namely the lack of a CNP in all four-terminal measurements, but its presence in two-terminal and three-terminal measurements. We fabricate more "Type A" devices (h-BN-CrI_3-graphene-h-BN) as well as "Type B" devices (h-BN-CrI_3-graphene-SiO_2). A few more observations from these devices (Devices A2, A3, A4, B1, B2) are reported in the following sections.

Absence of proximity induced spin orbit coupling

Sweeping the magnetic field slowly through zero, we observe peaks in the resistance of our devices at $B = 0$. Data from three such devices are shown in fig. 5.17. These sharp, narrow peaks at $B = 0$ correspond to weak localization. As was discussed earlier in section 4.2.1, the presence of weak localization necessarily implies that there is no SOC, which otherwise would have manifested as a weak *anti*-localization *dip* in resistance at $B = 0$. Thus, we can conclusively say that there is no proximity

induced SOC in graphene in our devices.

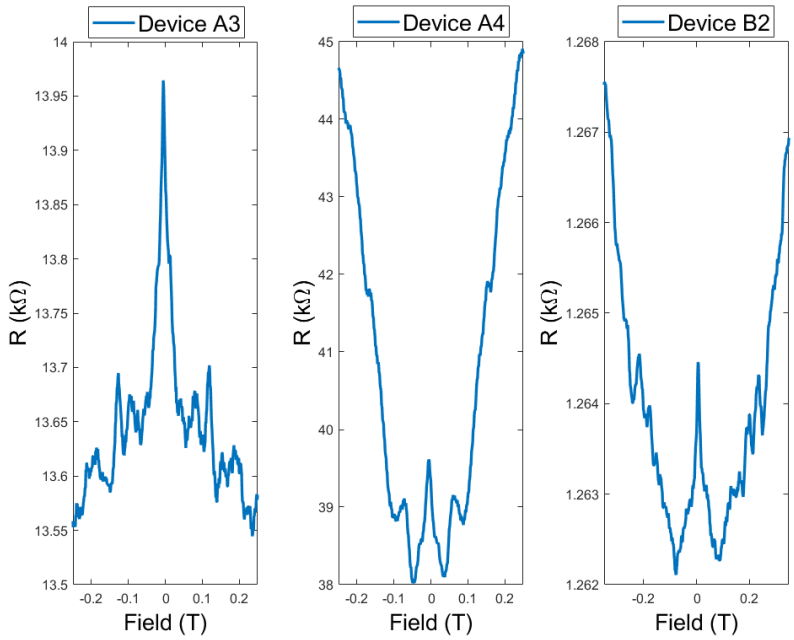

Figure 5.17: Weak localization in CrI_3-graphene devices
Resistance as a function of magnetic field in three different CrI_3-graphene devices. All devices demonstrate a weak localization peak at $B = 0$. Data for devices A3, and A4 recorded at 2 K. Data for device B2 recorded at 10 K.

Divergence upon repeated zero field cooling

Due to its absence in literature, we choose to report an observation here even though it is not a signature of a magnetic proximity effect in graphene. We notice in our devices a divergence in resistance upon repeatedly cooling and warming the device at zero magnetic fields. One such data, from device B1 is shown in fig. 5.18. Here we perform four cycles of zero field cooling (ZFC) and zero field heating (ZFH) sequentially between 200 K and 2 K. Each ZFC and ZFH pair has a separate trace that diverges around $T = 70\ K$.

Since T_c of CrI_3 is 61 K, one theory could be that the divergence is a signature of a ferromagnetic transition at the Curie temperature[22, 20]. Each time the device is cooled down below T_c the magnetic moments "freeze" in different domain structures. Each domain structure is unique, and would scatter electronic carriers differently on a macroscopic scale, thus leading to differing resistance traces. Since the domain structure stays frozen until the temperature is increased above T_c, the ZFH trace lies exactly on top of its corresponding ZFC trace which can be seen in fig. 5.18.

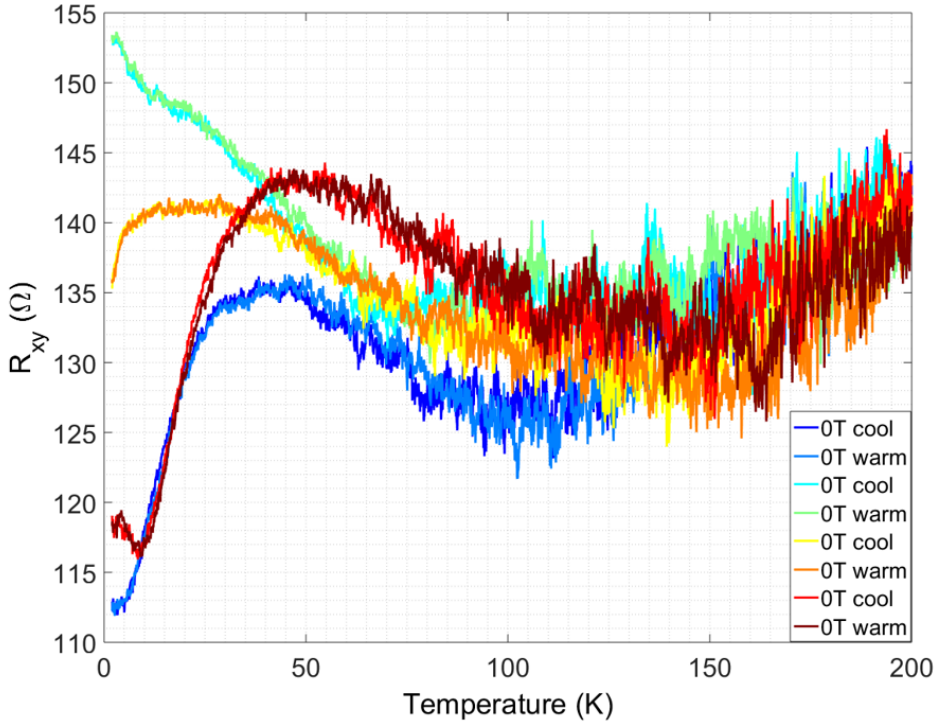

Figure 5.18: Repeated zero field cooldowns in device B1
R_{xy} traces for device B1 for four sets of ZFC and ZFH. Each ZFC and ZFH pair lie on top of each other perfectly, but each set is different from the subsequent pair below $\sim 70\ K$.

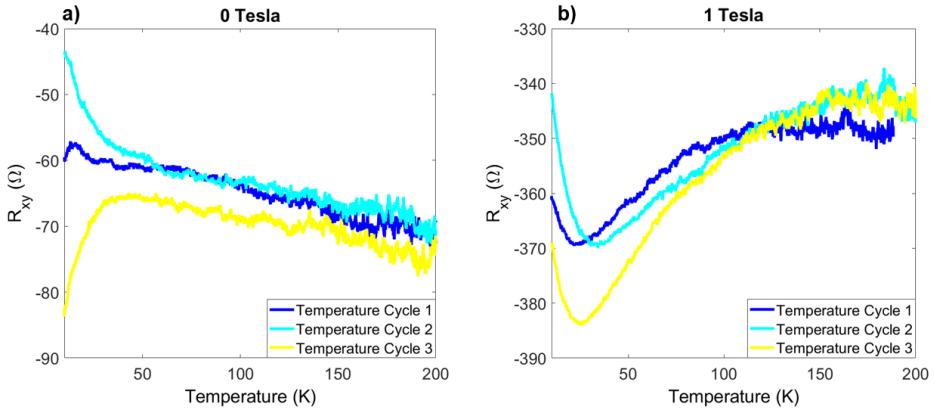

Figure 5.19: Repeated temperature cycles in device A3
R_{xy} traces for device A3 for three sets of temperature cycles taken at (a) $B_\perp = 0\ T$ and (b) $B_\perp = 1\ T$. Divergence at lower temperatures is visible in both scenarios

However, the presence of a magnetic domain structure necessarily requires a mag-

netic hysteresis loop to correspond with the switching of the magnetic domains as the external magnetic field is varied. Slowly ramping the magnetic field in both directions, we do not observe a magnetic hysteresis loop. Thus, the divergence upon ZFC is not related to a magnetic transition.

The coercive field of CrI_3 is $\sim 50\ mT$. Thus, if we repeated such a measurement with an out of plane magnetic field $B_\perp > 50\ mT$, we would expect all the R_{xy} traces to lie on top of each other. This is because all the magnetic domains would now be perfectly aligned with the external magnetic field, and there would not be a new random configuration of magnetic domains each time upon cooling. But as can be seen in fig. 5.19, we observe the divergence at lower temperatures even at $B_\perp = 1\ T$. Thus the origin of the divergence upon cooling is not magnetic.

It is more likely that the effect is a result of (non-magnetic) impurity sites due to disorder in the device. These sites are mobile at high temperatures but freeze at different locations at low temperatures. The electrons would then get scattered differently based on the configuration of these scattering sites, leading to diverging traces of the resistance upon cooling.

5.4 $CrSiTe_3$ - Graphene results

5.4.1 Non local transport in $CrSiTe_3$ - graphene

We have already mentioned how non local transport can be utilized as a tool for studying the MEF in section 4.2.1. Motivated by results of P. Wei et al. on EuS-graphene, we extend the idea to $CrSiTe_3$-graphene devices[36]. The idea is to first measure non local transport in graphene only, which will be a control experiment. After, we transfer $CrSiTe_3$ on top, and remeasure non local transport in the $CrSiTe_3$-graphene heterostructure. As with the case of CrI_3, the graphene surface is cleaned with a contact AFM tip prior to $CrSiTe_3$ transfer. An enhancement in non local transport signal would be expected in the device if there were an enhanced MEF in graphene due to a magnetic proximity effect induced by $CrSiTe_3$. The schematic of such a device is shown in fig. 5.20. We label such devices ($CrSiTe_3$-graphene-SiO_2) with the label "C".

5.4.2 Characterizing graphene transport prior to $CrSiTe_3$ transfer

Transport characteristics of our graphene on SiO_2 "C" type devices are briefly summarized in this section. The quality of these devices are on par with the best graphene on SiO_2 devices in literature. All of our devices exhibit mobilities in the $5,000 - 10,000\ cm^2/V.s$ range.

As a representative device, graphene transport characteristics from device C1 are shown in fig. 5.21. AFM scan over the Hall bar demonstrates that all particulates have been pushed away from the graphene channel (fig. 5.21b). Varying the carrier density

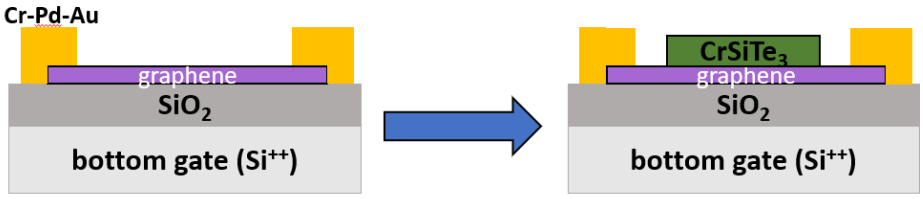

Figure 5.20: Construction of a "Type C" device
A graphene Hall bar is first fabricated on an SiO_2/Si substrate and measured. Thereafter, the graphene surface is cleaned with a contact AFM tip, and a $CrSiTe_3$ flake is transferred on the graphene channel.

by means of a global back gate simultaneously with the out-of-plane magnetic field yields the familiar Landau fan associated with the QHE (fig. 5.21c). Zero field carrier density sweep (not shown here) reveals a mobility of $\approx 10,000\ cm^2/V.s$. Explicit traces at 12 Tesla of the device resistance R_{xx} and transverse conductivity σ_{xy} are shown in fig. 5.21d and fig. 5.21e respectively.

The Hall conductivity plateaus $\sigma_{xy} = \nu e^2/h$ are shown in fig. 5.21e for $\nu = -10, -6, -2, +2, +6$. Thus, the QHE effect is observed with the fourfold degeneracies intact in the Landau levels.

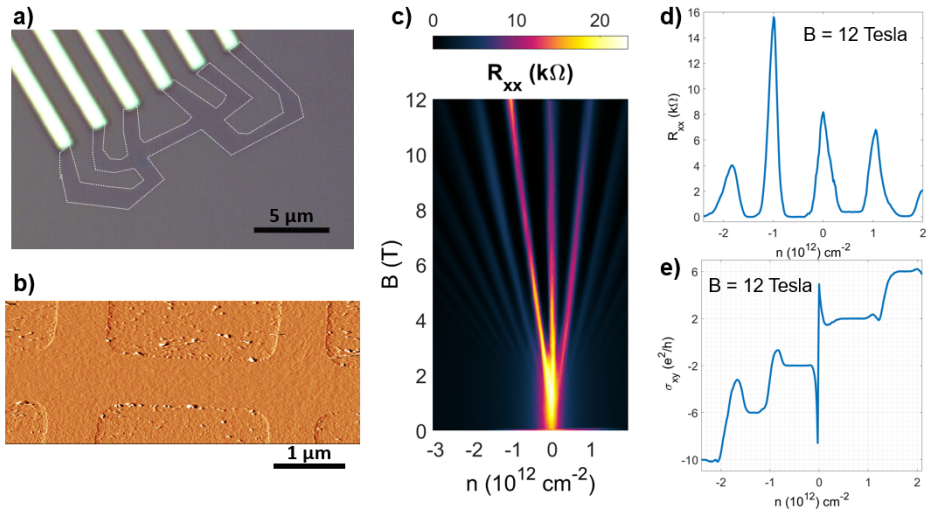

Figure 5.21: Transport characteristics of graphene in device C1 prior to $CrSiTe_3$ transfer
(a) Optical image and (b) AFM image (deflection) of device C1. Colour range is 250 pA (c) Landau fan in R_{xx} colour map vs density and perpendicular magnetic field. Line traces at 12 Tesla of (d) R_{xx} and (e) σ_{xy} vs density

5.4.3 Enhancement of non local transport in $CrSiTe_3$-graphene

Non local transport of graphene is first characterized to perform a control experiment and reproduce results of Abanin et al.[112]. These are summarized in fig. 5.22 for device C2. Firstly, we see the strongest signal at charge neutrality near $V_{gate} = 33\ V$. Thus, the graphene is implicitly hole doped. The non local signal is relatively small at $B_\perp = 0$ and steadily increases with increasing $B_\perp$. A classical explanation for the giant non local resistance was already discussed in section 4.2.1 in terms of the ZSHE and inverse ZSHE due to equally populated Dirac cones of electrons and holes with opposite spins[112].

At low temperatures and large magnetic fields, the Dirac cone picture is replaced by a Landau level picture. Each Landau level is spin split due to the Zeeman effect under the application of a magnetic field. At exactly half filling of a Landau level, there thus exist an equal population of electrons and holes with opposite spins, that give rise to a giant non local resistance by means of a ZSHE and inverse ZSHE. The key difference from the classical case however, is that there will now be additional peaks associated with half filling of *every* Landau level[112]. Thus, we see an additional prominent peak associated with $\nu = 4$ (near $V_{gate} = 16\ V$ at 12 T in fig. 5.22b), corresponding to half filling of the first Landau level.

After $CrSiTe_3$ transfer, we notice that the CNP has shifted to $V_{gate} = 50\ V$. Thus, the graphene has been further hole doped by the $CrSiTe_3$ by about $p \approx 1.22 \times 10^{12}\ cm^{-2}$. The mobility of C2 device reduced slightly from $5,000\ cm^2/V.s$ to $4,000\ cm^2/V.s$ after $CrSiTe_3$ was transferred onto the graphene. Thus, there is not a significant reduction in the quality of the device. Non local resistance of C2 *after* $CrSiTe_3$ transfer is shown in fig. 5.23. Most notably, we see an enhancement in the absolute value of the non local signal. The peak non local signal at the Dirac point $R_{NL,D}$ increases from $\approx 13\ k\Omega$ to $\approx 25\ k\Omega$. Additionally, the non local peak at $\nu = 0$ appears broader than before, with the $\nu = 4$ branch not visible.

We now directly compare the non local response in graphene before and after the addition to $CrSiTe_3$ to the device. Overlaying the two curves, we see a nearly two fold enhancement in the non local signal at 12 Tesla (fig. 5.24) at charge neutrality, and a suppression of the peak associated with $\nu = 4$.

The non local resistance at the Dirac peak is tracked as a function of the magnetic field (fig. 5.25a). Based on the approach used by P. Wei et al. [36], we use the comparison between the before/after $CrSiTe_3$ $R_{NL,D}$ behaviour to extract the MEF strength.

The non local resistance at the Dirac point is given by

$$R_{_{NL,D}} \propto \frac{1}{\rho_{xx}} \left(E_Z \frac{\partial \rho_{xy}}{\partial \mu} \right)^2 \Bigg|_{\mu_D} \tag{5.1}$$

For fitting purposes, equation (5.1) can be rewritten as

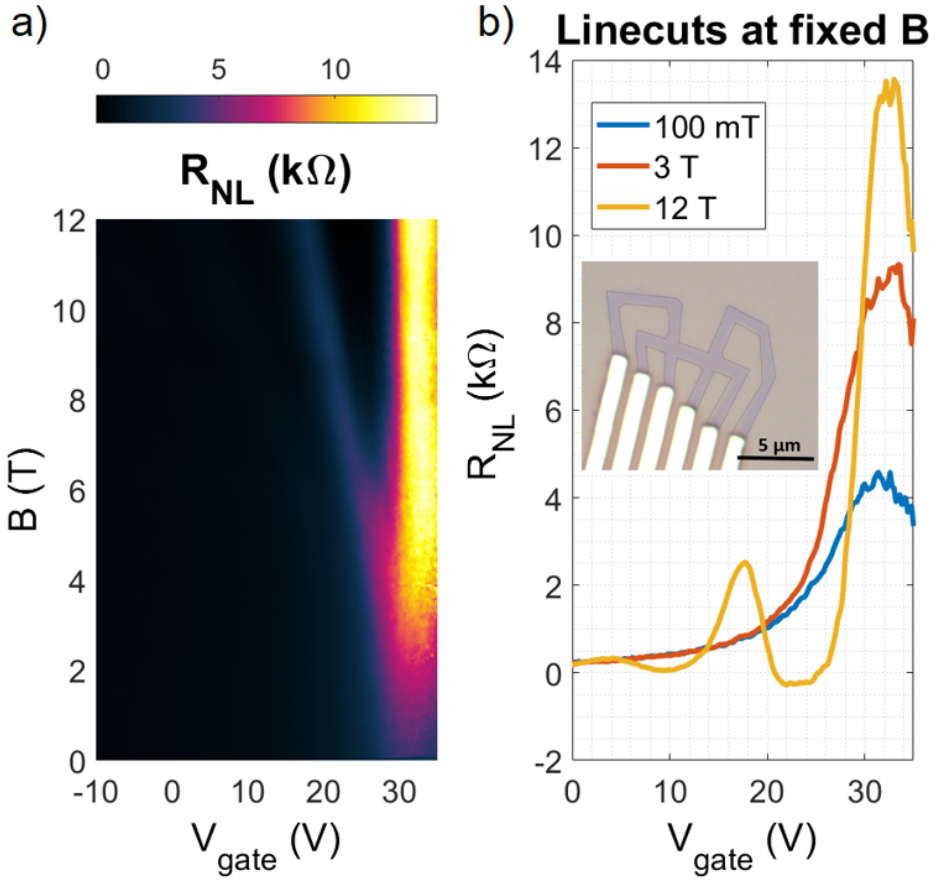

Figure 5.22: Non local resistance of device C2 before $CrSiTe_3$ transfer
(a) 2D colour map of non local resistance in B-V_{gate} space. (b) Line traces vs V_{gate} at three different $B_\perp$ values. Inset shows optical image of graphene Hall bar.

$$R_{NL,D} = R_0 + \beta(B) \cdot E_Z^2 \tag{5.2}$$

Here E_Z is the strength of the MEF that we wish to extract. R_0 is the non local resistance offset at magnetic field $B = 0$. $\beta(B)$ is a single quantity (as a function of the external magnetic field B) incorporating the remainder of the terms in eq. (5.1). Similar to the analysis in ref. [36], we assume that $\beta(B)$ does not change after the $CrSiTe_3$ transfer. This is a reasonable assumption, since the change in mobility is $\approx 20\%$, which corresponds to only a $\approx 10\%$ change in $R_{NL,D}$. For the "graphene only" case, $E_Z = \mu_B B$ since there is zero MEF. Thus, we can fit the "graphene only" data to eq. (5.2), and calculate $\beta(B)$. Once $\beta(B)$ has been determined, we replug it in eq.5.2 and refit eq. 5.2 to the $CrSiTe_3$-graphene data to determine $E_Z = \mu_B(B_{Zeeman}) = \mu_B(B_{external} + B_{MEF})$.

Raw $R_{NL,D}$ data before and after $CrSiTe_3$ transfer, along with the extracted MEF are plotted in fig. 5.25. At 12 Tesla (external field), we find a significant net Zeeman

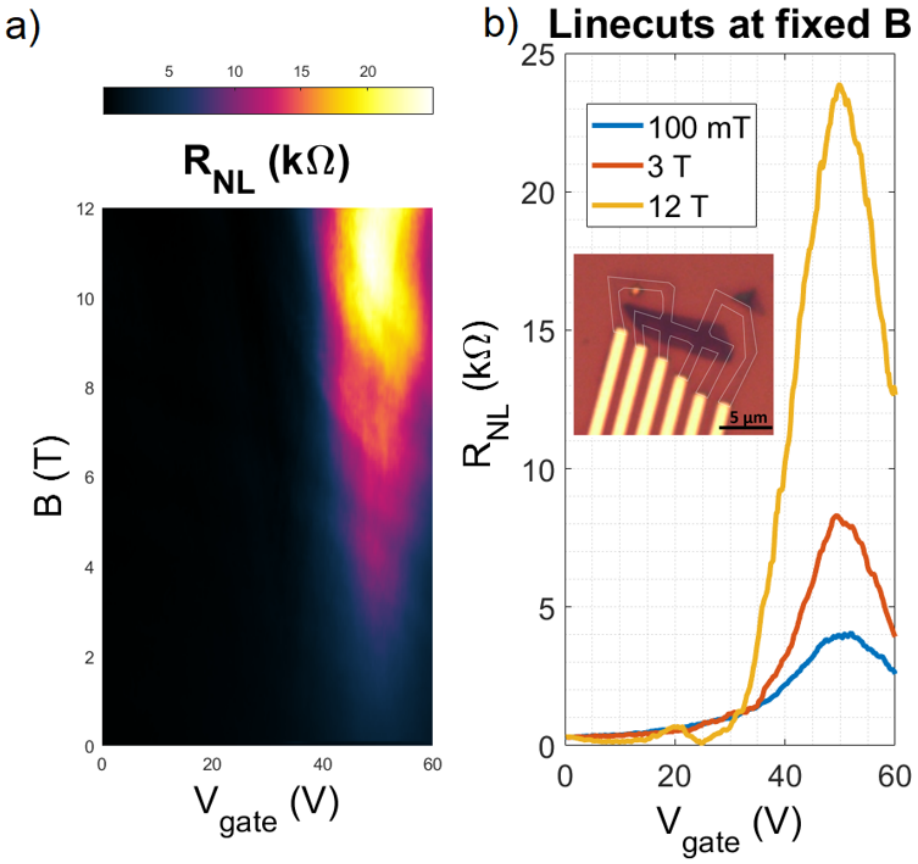

Figure 5.23: Non local resistance of device C2 *after* $CrSiTe_3$ transfer (a) 2D colour map of non local resistance in B-V_{gate} space. (b) Line traces vs V_{gate} at three different $B_\perp$ values. Inset shows optical image of the device with $CrSiTe_3$ flake in purple. Graphene Hall bar underneath is outlined in white.

field of 33 Tesla ($\approx 3.5\ meV$).

We now share some inconsistencies in our observations compared to what might be expected out of a proximity induced magnetic exchange in graphene. Firstly, the extracted B_{Zeeman} continues to increase up to 12 Tesla (external field). Whereas it would be expected that the MEF and hence B_{Zeeman} would increase sharply near $B_{external} = 0$ and quickly saturate at a relatively low field. For example, the saturation field of $CrSiTe_3$ (the field at which the net magnetization saturates) is $\sim 100\ mT$. This discrepancy is also a common theme in the graphene-EuS work in ref. [36] where the authors observe no sign of saturation in the B_{Zeeman}. Secondly, the raw $R_{NL,D}$ signals for both graphene and $CrSiTe_3$-graphene systems track each other fairly well until $B_{external} = 6\ T$ before the latter increases much more. It would normally be expected that $R_{NL,D}$ for the $CrSiTe_3$-graphene system would be greater than that of the graphene only system from the onset.

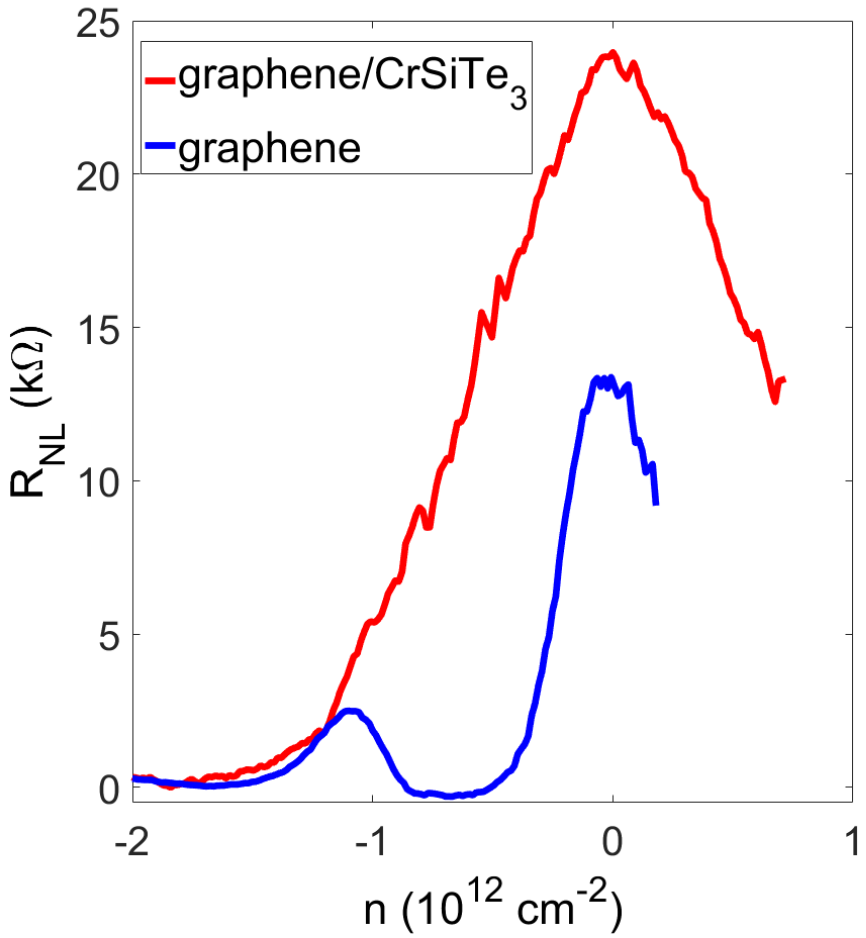

Figure 5.24: Enhanced non local transport in device C2
Non local resistance vs density at 12 Tesla before and after $CrSiTe_3$ transfer. The non local resistance at CNP increases from 13 $k\Omega$ to 24 $k\Omega$.

Improving non local transport measurement setup

After our measurements on device C2, we became aware of a separate work which pointed out that measurement artefacts can appear in non local transport, when necessary precautions are not taken [125]. This arises due to a common mode voltage $V_{CM} \neq 0$ at the centre of the vertical branch of the Hall bar. This is indicated by a red dot in fig. 5.26a. Since $V_{CM} \neq 0$, a non zero charge current now flows across the device channel. Due to different contact resistances of pins 3 and 4, this current splits in unequal amounts when draining to ground. Thus, there is a non zero contribution to the potential difference between pins 3 and 4 which gets picked up when measuring the non local voltage.

On subsequent devices we implemented a technique that is described by ref. [125]

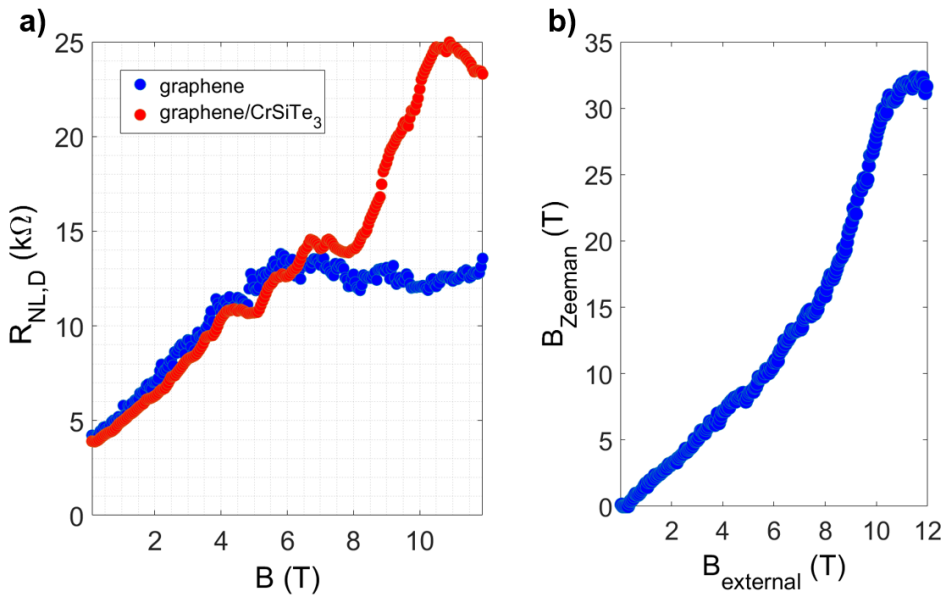

Figure 5.25: Extracting the strength of the magnetic exchange field from non local transport

(a) Non local resistance at the Dirac point as a function of the external field (b) Net B_{Zeeman} extracted from data in (a) versus the external magnetic field.

and illustrated in fig. 5.26b. We first use an op-amp feedback mechanism to neutralize V_{CM} whilst flowing the same current through the device. Additionally, on the measurement side we added a high input impedance preamplifier to eliminate any effects arising from differences in contact resistance.

We first tested this apparatus on a "dummy Hall bar" that was fabricated by soldering 7 resistors (6 Hall bar leads, and 1 device channel) to replicate our vdW device. We found that if uncorrected, $V_{CM} \sim 100\mu V$ and was reduced to $V_{CM} < 1\mu V$ after.

Fig. 5.26c illustrates the difference that arises as a result of implementing this new measurement scheme on graphene device C5 before transfer of $CrSiTe_3$. Without the op-amp feedback and SR560 preamplifier, we see large negative R_{NL} at $B_\perp = 0$. After adding the op-amp feedback and SR560 preamplifier, we eliminate this spurious signal, and measure R_{NL} close to 0 Ω, as would be expected.

One important point to be careful about with these measurements is the following. It is imperative to ensure that pin 2 is already grounded before the common mode pin (that is connected to $-$ terminal of op-amp) is grounded. When starting measurements, the common mode pin should be floated before pin 2. When grounding the device, pin 2 should be grounded before the common mode voltage. Otherwise, the output of the op-amp that is connected to pin 2 will be very large in magnitude due to the op-amp's large gain and destroy the pin. The resulting potential at pin 2

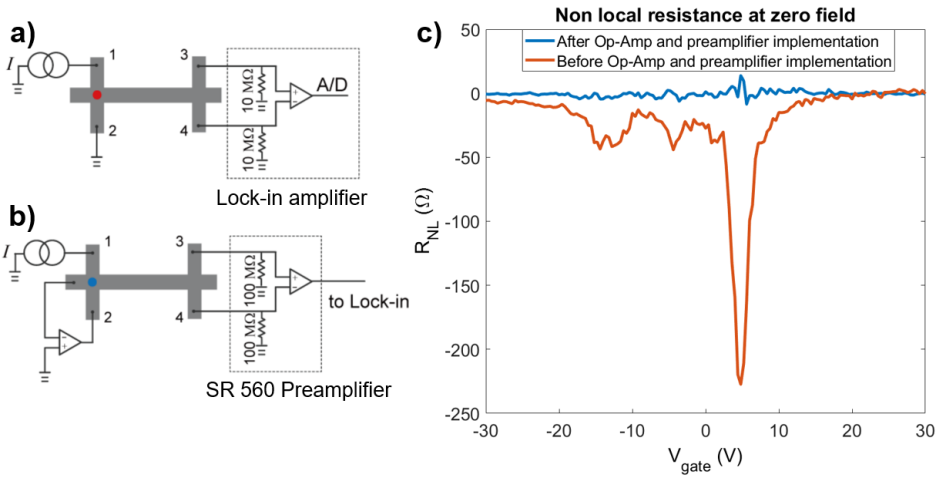

Figure 5.26: Elimination of spurious non-local signal in device C5 (a) Measurement schematic before any additions (b) An op-amp feedback is added to the left vertical branch (sourcing side) and a preamplifier with large input impedance is added to the right vertical branch (measurement side) (c) Non local signal at zero external field. A spurious signal of 250 Ω is removed by improving the measurement scheme. Panels (a) and (b) adapted from ref. [125]

is as large as $\pm 15\ V$ in our case since the op-amp is powered by DC voltage inputs of $\pm 15\ V$.

We were unable to test the impact of this new measurement scheme on device C2 (that we discussed in the previous section) due to failure of its contacts over the course of measurement, which made subsequent measurements impossible. Additionally, we were unable to replicate the results of device C2 in subsequent $CrSiTe_3$-graphene devices. These factors, along with the absence of saturation of the MEF are why we cannot confidently contribute the enhancement of non local resistance in device C2 as arising out of a proximity induced MEF.

5.4.4 Divergence upon repeated cooldowns

In section 5.3.4 we discussed the divergence on repeated cooldown at zero magnetic field for CrI_3-graphene devices. This observation was explained as not a signature of magnetism, but rather the freezing of impurity scattering sites in the device at low temperatures. We also observe this phenomena in $CrSiTe_3$-graphene devices.

For device D1 (construction of this device is discussed later in sec. 5.4.6) this is shown in fig. 5.27. Two curves tracing the Hall resistance R_{xy} are recorded as the device is cooled down on two separate occasions under identical conditions ($B = 0$) shortly one after the other. The two curves appear to diverge starting $T \approx 110\ K$, much greater than the Curie temperature of $CrSiTe_3$[25, 26].

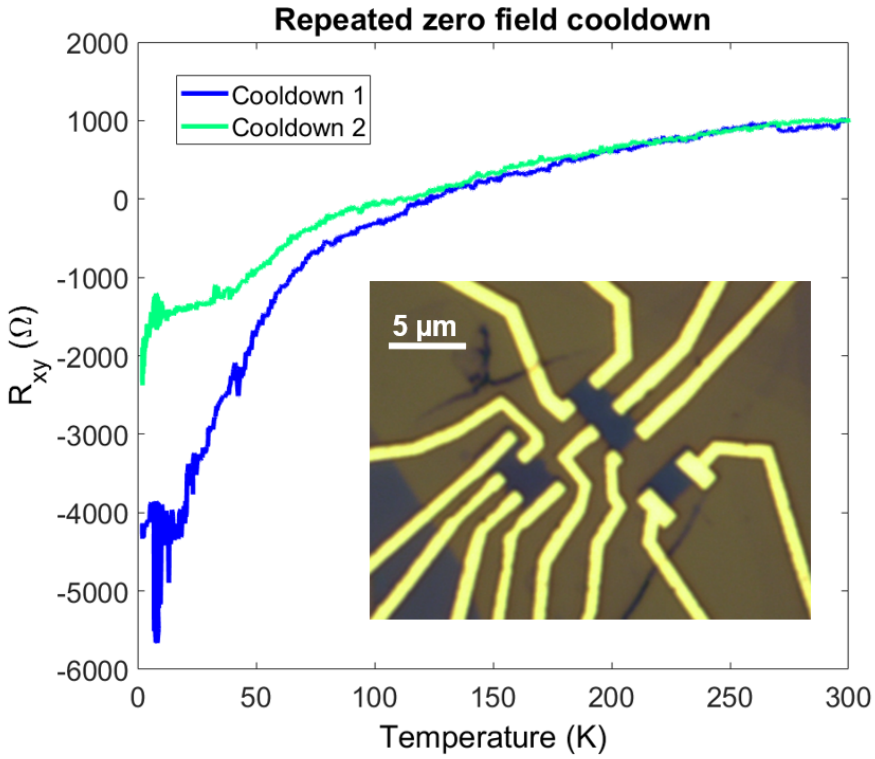

Figure 5.27: Repeated zero field cooldowns in device D1
The two curves start diverging around T$\sim$ 110 K, much greater than $T_c = 33$ K forCrSiTe$_3$. Inset contains an optical image of device D1

The absence of any hysteretic behaviour vs external magnetic field at low temperatures points to this phenomena arising due to (non magnetic) impurity scattering based contribution to the resistance.

5.4.5 Absence of spin orbit coupling

We do not observe any signatures of AHE or WAL. Instead we observe weak localization peaks at $B = 0$, indicating that the CrSiTe$_3$-graphene devices, similar to CrI$_3$-graphene devices do not possess any proximity induced spin orbit coupling effects. This is demonstrated in fig. 5.28 for two CrSiTe$_3$-graphene devices at low temperatures.

5.4.6 Quality of graphene in CrSiTe$_3$-graphene devices

Unlike the CrI$_3$-graphene devices, the CrSiTe$_3$-graphene devices do not degrade and retain their electrical properties after the transfer of the 2D magnet on top of the graphene channel. We show this explicitly in fig. 5.30 for device C3. Optical and AFM

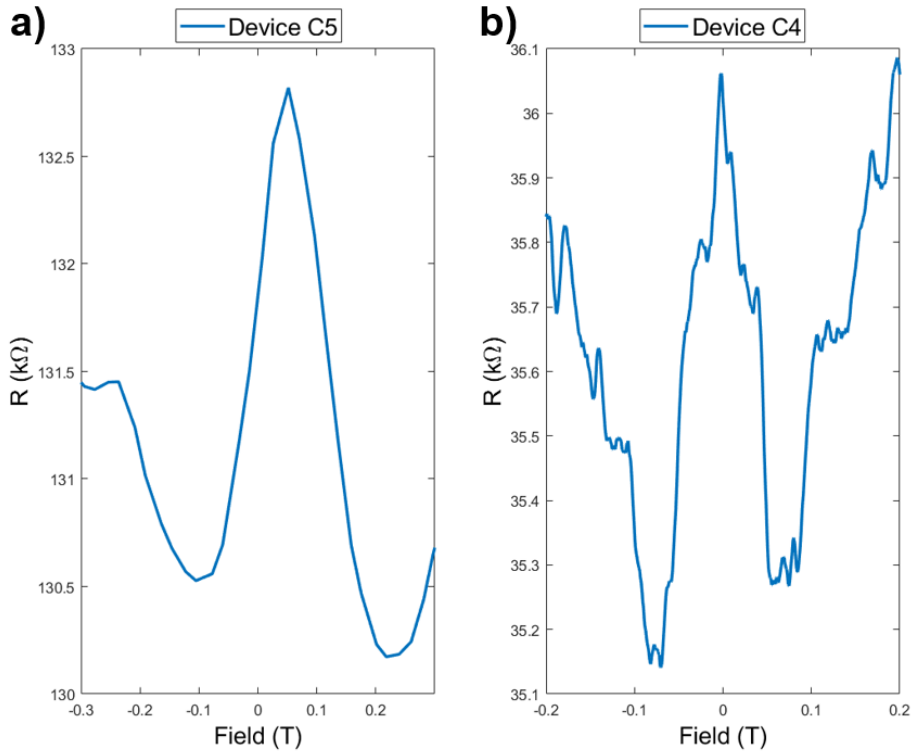

Figure 5.28: Weak localization in $CrSiTe_3$-graphene devices
Resistance as a function of magnetic field in two different $CrSiTe_3$-graphene devices. Weak localization peak is visible at $B = 0$.(a) Two-terminal resistance for device C5, recorded at 2 K (b) Four-terminal resistance in device C4, recorded at 37 mK

images of this device C3 are shown in fig. 5.29. Four-terminal resistance measurements reveal a clean quantum Hall effect with fourfold degenerate Landau levels, consistent with the quality of graphene expected on SiO_2 substrates.

Additionally, we confirm that graphene and $CrSiTe_3$ retain their properties even beyond device nanofabrication steps in other device geometries. In "type D" devices, we assemble vdW heterostructures of h-BN-graphene-$CrSiTe_3$-SiO_2, and then make one dimensional edge contacts to the graphene [121]. A schematic of this is shown in fig. 5.31a. For device D1 (fig. 5.31b and fig. 5.31c), we once again observe the familiar fourfold degenerate QHE, consistent with a bottom SiO_2 substrate.

Even though we do not see conclusive evidence of a magnetic proximity induced MEF in graphene, the quality of graphene channel in $CrSiTe_3$-graphene devices is an encouraging result nonetheless, keeping in mind the chemically unstable nature of vdW magnetic materials.

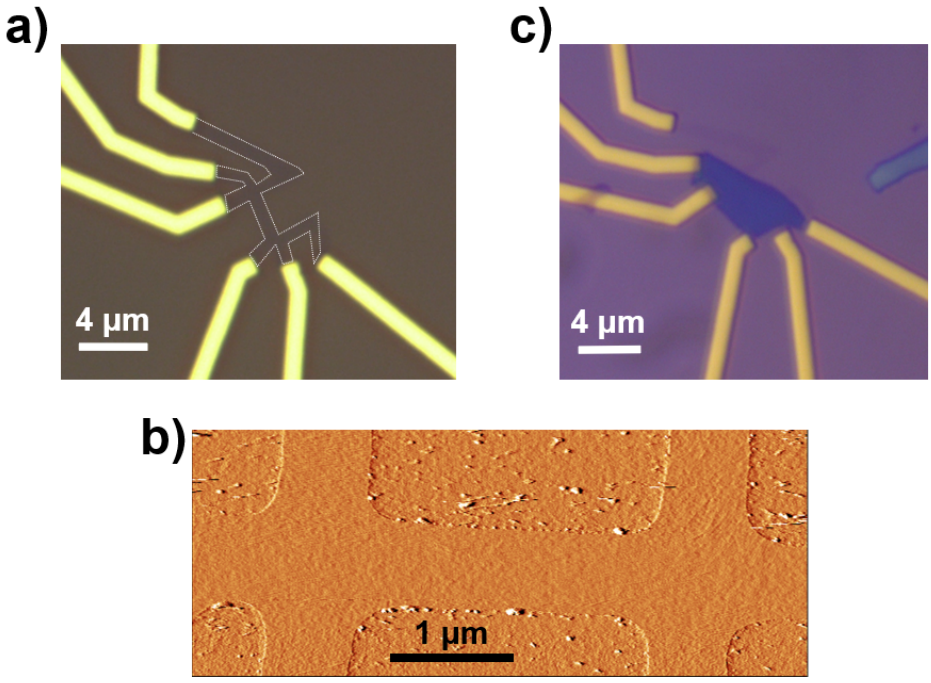

Figure 5.29: Completion of device C3
(a) Optical image of graphene Hall bar (outlined in white) (b) AFM deflection scan of device just prior to $CrSiTe_3$ transfer. Colour scale range is 250 pA (c) Optical image of device C3 after transfer of $CrSiTe_3$ flake.

5.4.7 Magneto-optical characterization of $CrSiTe_3$-graphene devices

To test the quality of the chemically sensitive $CrSiTe_3$ we perform reflective magnetic circular dichroism (RMCD) measurements on device C4. RMCD measurements are fairly identical to MOKE measurements that were introduced in section 1.2.4. The key difference is that while MOKE measures the change in the polarization angle of the reflected light, RMCD measures the difference in the intensity of right circularly polarized and left circularly polarized light. To first order, RMCD is a quantity directly proportional to the sample magnetization, and this is how we will treat it[126].

Optical and AFM images of device C4 that were used for magneto-optical characterization are shown in fig. 5.32. After device fabrication and transport measurement, the device was stored in our N_2 glovebox for 1 month before being loaded into another cryostat for RMCD measurements.

RMCD traces from a single point on the $CrSiTe_3$-graphene channel are shown in fig. 5.33. At the lowest temperatures, we observe signatures consistent with soft ferromagnetism. The RMCD signal saturates at external magnetic field of few tens of

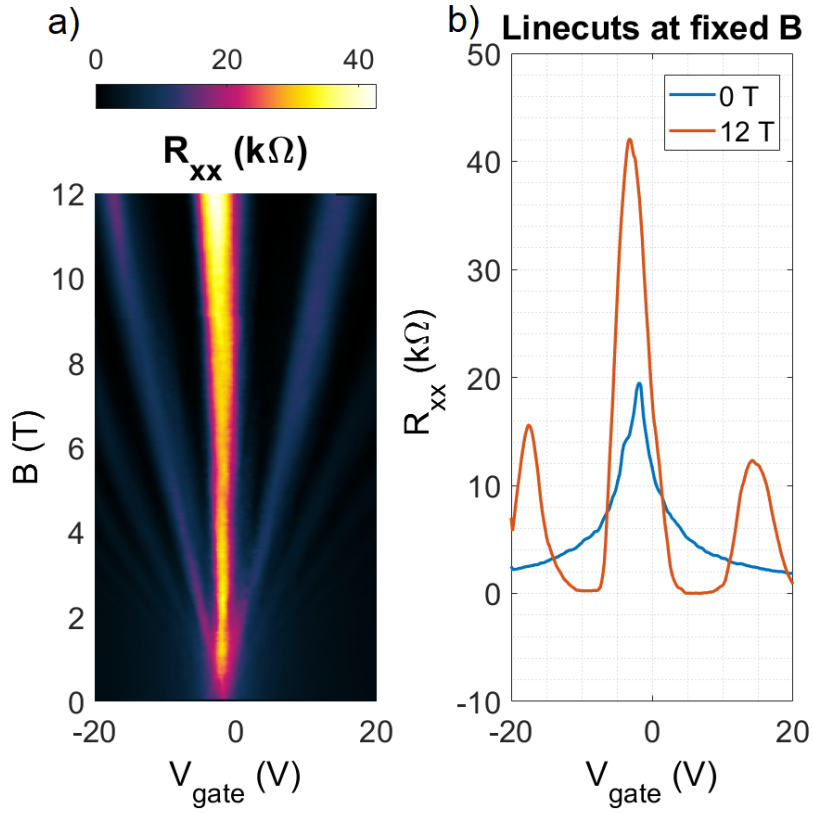

Figure 5.30: Quantum Hall transport in device C3
(a) Colour map of four terminal R_{xx} in $B - V_{gate}$ space (b) Line traces of R_{xx} vs V_{gate} at 0 T and 12 T

mT. Traversing the external field in both directions through zero, we do not observe a hysteresis loop. Increasing the temperature, the ferromagnetic RMCD characteristic is replaced by a paramagnetic trace, visible at 34 K and 36 K. Here, the RMCD has a linear dependence on the external field. This is consistent with $CrSiTe_3$ behaviour that is known to have a $T_c = 33$ K[25, 26].

We further explore the spatial distribution of RMCD signal at different external magnetic field values. These measurements were taken at 5 K. Small domain structures on the length scale of a few microns are visible as their local magnetic moments switch at different values of the external magnetic field.

While the RMCD measurements cannot ascertain the magnetic state of the graphene itself, they nonetheless demonstrate that $CrSiTe_3$ retains its magnetic properties over a time period greater than 1 month and does not degrade completely, unlike CrI_3.

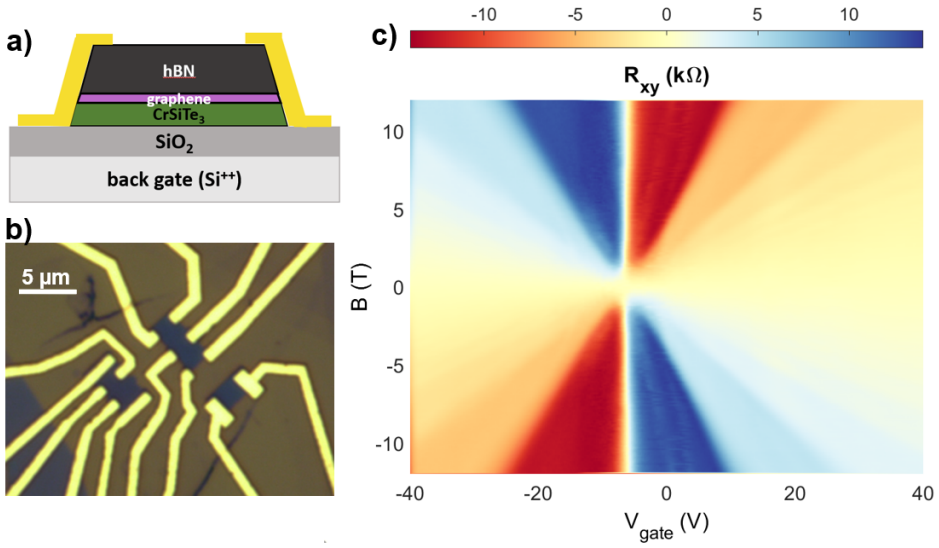

Figure 5.31: Device D1 summary
(a) Schematic of edge contacted device D1 (b) Optical image of D1 (c) Quantum Hall resistance shows plateaus consistent with fourfold degenerate Landau levels

5.4.8 Capacitance measurements in $CrSiTe_3$-graphene devices

Encouraged by the chemical stability of both graphene and $CrSiTe_3$ over an extended time period, we attempt to study the bulk capacitance of $CrSiTe_3$-graphene system to test for any proximity induced SOC. This experiment was introduced in sec. 4.2.3 when J. Island demonstrated proximity induced Ising SOC in graphene-WSe_2 heterostructures by tracking the position of the $\nu = \pm 3$ filling factor versus vertical electric field[35].

To this end, we fabricated dual graphite gated $CrSiTe_3$-bilayer graphene devices ("Type E devices"). The complete heterostructure from top to bottom was graphite-h-BN-$CrSiTe_3$-bilayer graphene-h-BN-graphite on SiO_2/Si substrate. Device nanofabrication was done *after* vdW heterostructure assembly. Using tapping mode AFM images, we were able to located positions at which bubbles and particulates were present, and etch away those regions. Thus, we were able to shape the device such that no bubbles were present, for the cleanest possible device.

Optical image of device E1 is shown in fig. 5.35a. The device has a slightly irregular shape so as to etch around any bubbles, whilst maximizing the device area so as to maximize the capacitance.

Penetration capacitance data (where peaks correspond to low density of states associated with gaps) for device E1 is shown versus the external perpendicular field and the *back* gate voltage. The peaks in capacitance that have been highlighted with dotted white lines correspond to Landau level gaps.

We see signatures of some symmetry breaking with $\nu = -4,\ -2,\ 0,\ 1,\ 2,\ 4$ visi-

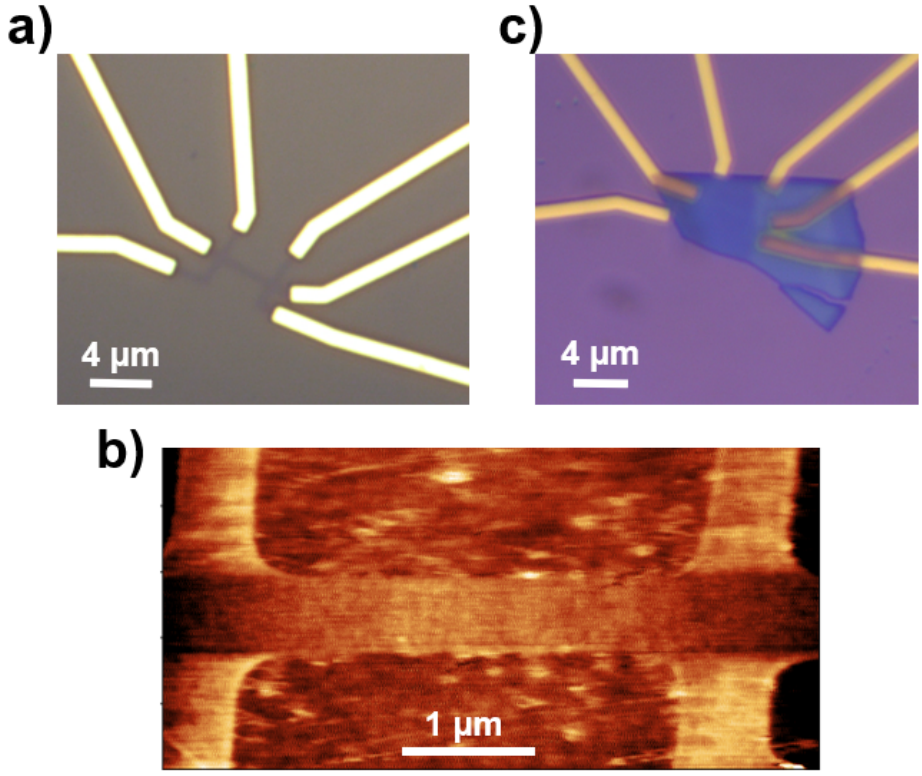

Figure 5.32: Device C4 fabrication
(a) Optical image of graphene Hall bar (outlined in white) (b) AFM topography scan of device just prior to $CrSiTe_3$ transfer. Colour scale range is 3.5 nm (c) Optical image of device C4 after transfer of $CrSiTe_3$ flake.

ble (as opposed to $\nu = \pm 4$ only). Thus, this dual graphite gated, h-BN encapsulated device is of higher quality than any other $CrSiTe_3$-graphene devices we have fabricated (all of which only had degeneracy intact Landau level signatures in transport). However, despite a near identical fabrication scheme, the quality of this device is not as high as the WSe_2-graphene device that Island et al. fabricated. We suspect this is most likely due to $CrSiTe_3$ implicitly not being as ideal a proximal layer as h-BN or WSe_2 are to graphene. Even in the cleanest $CrSiTe_3$-graphene devices, this could be due to factors such as lattice constant mismatch, minute degradation of $CrSiTe_3$ that is not detectable macroscopically. Nonetheless, at fields as high as 13 T, we do not see the appearance of the $\nu = 3$ state so as to be able to track its position in the 2D space of electric field-carrier density.

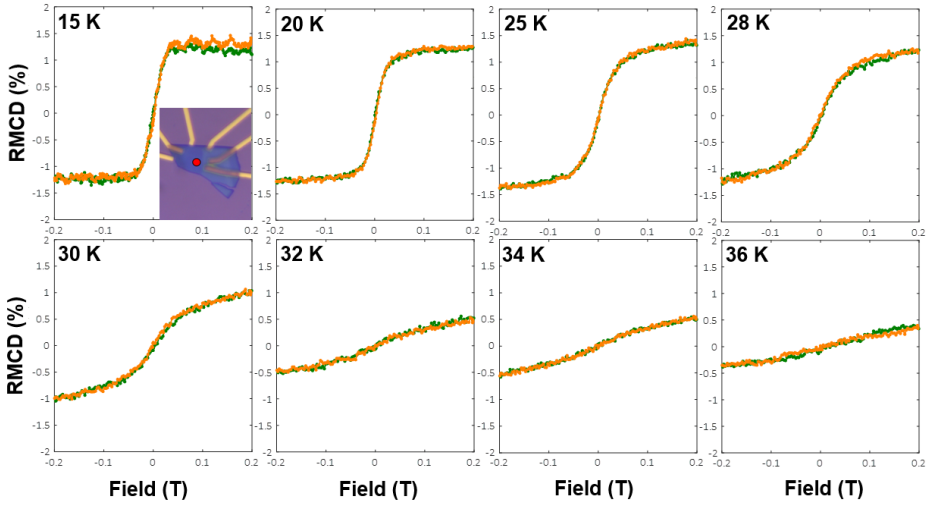

Figure 5.33: Magneto-optical characterization of device C4
RMCD traces versus external magnetic field at different temperatures. Inset of 15 K curve shows the point on $CrSiTe_3$ at which laser is shown (red dot). Orange (Green) trace is from negative (positive) field to positive (negative) field. Around 33 K, the RMCD trace changes from ferromagnetic to a paramagnetic one.

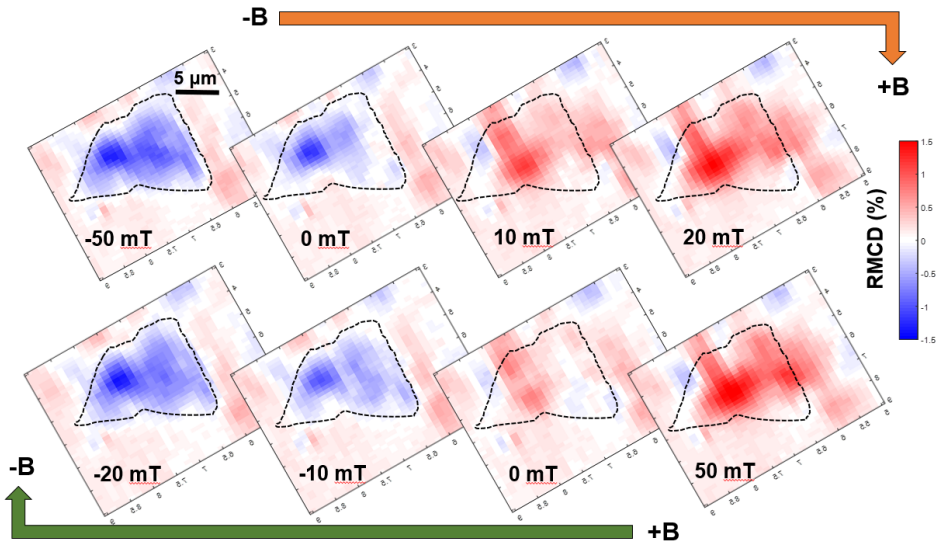

Figure 5.34: Spatial RMCD colour maps of device C4
External magnetic field is cycled through zero twice. The $CrSiTe_3$ flake is outlined in black. Magnetic switching is observed with coercive fields $\sim 20\ mT$ along with μm sized domain structure.

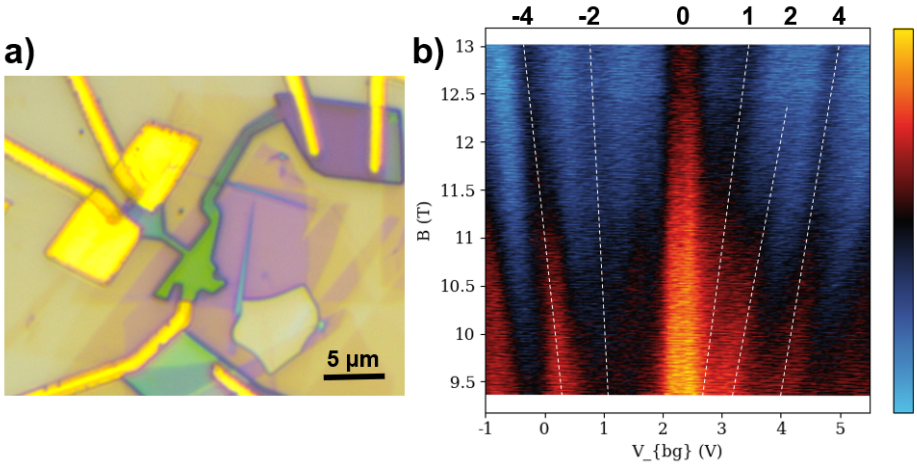

Figure 5.35: Capacitance of device E1 in the Landau level regime
(a) Optical image of device E1 (b) Penetration capacitance of E1 versus $B_\perp$ and $V_{back-gate}$ in the high magnetic field regime

5.5 Graphene - $RuCl_3$ results

We report on our observations pertaining to interfacial physics between graphene and the antiferromagnetic $RuCl_3$ here. We fabricate electronic transport devices out of h-BN-graphene-$RuCl_3$-h-BN heterostructures, with the graphene-$RuCl_3$ fully enclosed within the two h-BN layers. Thus, we utilize edge contacts to electrically contact the graphene[121]. We etch the device such that $RuCl_3$ is not exposed to the reactive ions during etching. Schematic of this device (labelled "Type F" device) is shown in fig. 5.36a.

Optical and AFM images of the completed device F1 are shown in fig. 5.36(b)-(d). As can be seen in fig. 5.36d, the edge of the device extends further beyond the $RuCl_3$ flake (outlined in black). To make edge contacts to the graphene (outlined in red), only the graphene, and the top/bottom h-BN flakes are shape etched.

Four terminal resistance measurements of device F1 versus back gate voltage and temperature are summarized in fig. 5.37. At first glance, the R vs V_{gate} curves in fig. 5.37b appear consistent with graphene's implicit transport behaviour, with a Dirac peak visible around +2 V at all temperatures. The absolute magnitude of the device resistance is between 150 Ω and 350 Ω. This is at least one order of magnitude lower than typical graphene device resistances (both from literature, as well as graphene devices with similar aspect ratios that we have studied). This observation is also consistent with two recent reports in literature that were discussed in sec. 4.2.2[117, 118].

One possible explanation for this enhanced conductivity is additional parallel conduction pathways opening up at the graphene-$RuCl_3$ interface. $RuCl_3$ is a Mott insulator, and thus, normally not expected to conduct electrons. However, when graphene

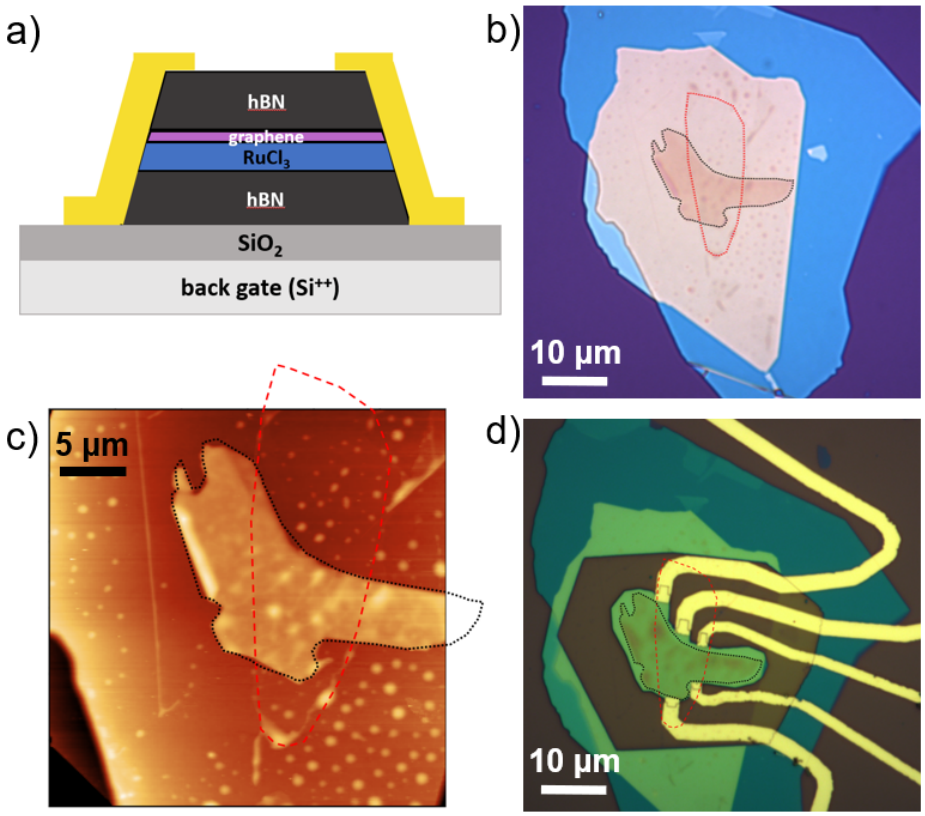

Figure 5.36: Device F1 nanofabrication summary
(a) Schematic of edge contacted graphene-$RuCl_3$ "F" type device (b) Optical image of device F1 before device nanofabrication. The large blue and yellow regions are h-BN flakes. Encapsulated between them are $RuCl_3$ (black outline) and graphene (red outline) flakes. (c) AFM image of device F1 before device nanofabrication (d) Completed device post nanofabrication. The device is etched around $RuCl_3$ on the outside

and $RuCl_3$ are brought into contact, electron transfer from graphene into $RuCl_3$ is plausible due to the work function differences (graphene: 4.6 eV and $RuCl_3$: 6.1 eV). The 1-3 layers of $RuCl_3$ closest to graphene would thus be parallel conducting channels, leading to a lower overall device resistance[118]. One argument against this theory is the presence of the CNP near $V_{gate} = 0$ V instead of a large positive value due to strongly p-doped graphene as a result of the charge transfer. We will mention as an improbable possibility that there are lateral distinct regions of graphene that are either undoped or p-doped, depending on whether there is a dirty or clean vertical interface with $RuCl_3$. The former gives rise to the visible CNP near $V_{gate} = 0$ V, whereas the latter still might give rise to a *second* CNP at a large positive V_{gate} that we cannot access.

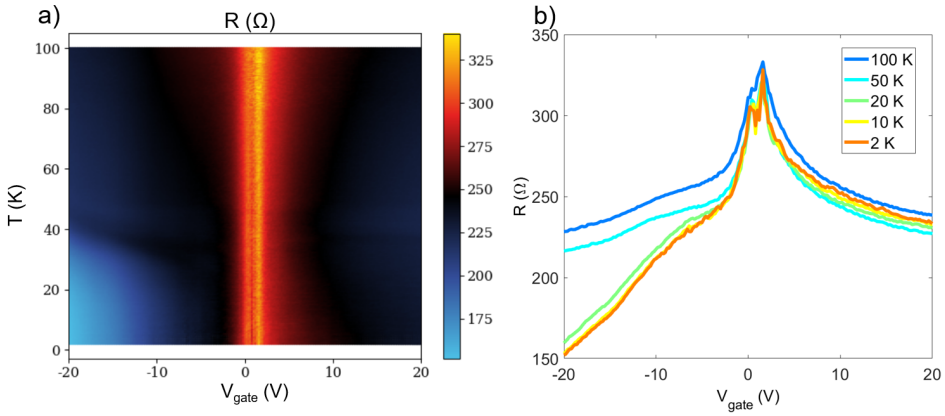

Figure 5.37: Enhanced conductivity in $RuCl_3$-graphene F1 device
Four terminal resistance of device F1 (a) As a function of temperature and V_{gate} (b) Line traces of resistance vs V_{gate} at different temperature values

It is more likely that there is a proximity effect comprising of hybridization between the graphene valence bands and the low energy $RuCl_3$ bands at the Fermi level due to the work function difference, as suggested by Mashhadi et al.[117].

For the most part, the device resistance does not exhibit a strong temperature dependence, except for a weak decrease with reducing T. This is consistent with a reduction in the phonon density of states upon cooling, leading to a reduction in phonon induced scattering [127]. However, we find an interesting divergence from this weak behaviour away from charge neutrality. Most visible is a blue dome of lower resistance in fig. 5.37a for $-20\ V < V_{gate} < -5\ V$ below 40 K.

We thus investigate this region in more detail, and procure another colour map in this negative V_{gate} regime (fig. 5.38). Upon cooling, line traces of resistance versus temperature (fig. 5.38b) reveal a hump at a critical temperature (between 30-45 K depending on the chosen V_{gate}) in addition to the weak decrease in resistance. This hump in resistance could be in line with critical behaviour associated with a phase transition at the critical temperature.

In magnetic systems, the electrical resistance behaviour near the critical temperature can be used to ascertain the macroscopic magnetic order[128, 129]. As the temperature approaches the Curie (Neel) temperature, the resistance, and the temperature derivative of the resistance show particular features associated with ferromagnetic (antiferromagnetic) phase transitions. In the vicinity of the critical Neel temperature, dR/dT is described by a power law behaviour

$$dR/dT = A\left(\frac{|T - T_N|}{T_N}\right)^{-\lambda} \tag{5.3}$$

Here the constant A has opposite signs for $T > T_N$ and $T < T_N$ cases.

Plotting the temperature derivative of the resistance dR/dT, we notice a clear

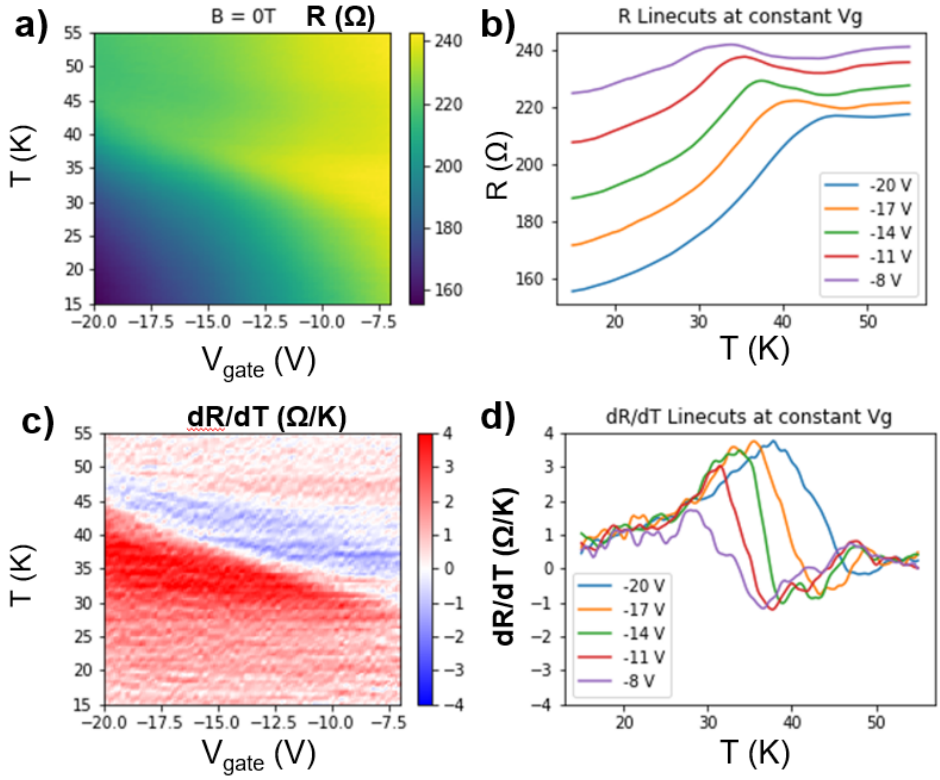

Figure 5.38: Magnetic transition signature in electronic transport in device F1 (a) Resistance vs temperature and V_{gate} in a narrow range (b) Resistance linecuts vs temperature at different V_{gate} values (c) Derivative of resistance dR/dT vs temperature and V_{gate} (d) dR/dT linecuts versus temperature at different V_{gate} values

peak-dip feature in the colour map (red to blue transition) and dR/dT linecuts at different V_{gate} values (fig. 5.38 (c)-(d)). Such a peak dip feature in dR/dT vs temperature is a signature of an antiferromagnetic transition, as was first predicted by Suezaki and Mori and later polished by Alexander, Helman, and Balberg [128, 129]. Experimentally, behaviour consistent with these predictions were reported for the antiferromagnetic transition in chromium[130].

Interestingly though, we observe this antiferromagnetic transition at a much elevated temperature compared to the Neel temperature of $RuCl_3$, which is either 7 K or 14 K based on the stacking order. We believe this enhanced T_N is tied with the electrostatic effects that are also responsible for the order of magnitude lower resistance. This is further corroborated by the the variation in T_N as we vary V_{gate}. Varying V_{gate} from -8 V to -20 V, we observe T_N increase from $\approx 36\ K$ to $\approx 48\ K$. We assign the Neel temperature as the point at which the dR/dT dip occurs, consistent with the predictions of Alexander, Helman, and Balberg[129].

Somewhat similar observations are shared by the report from Zhou et al.[118]. They also observe signatures of magnetic transitions at comparable elevated temperatures that are gate voltage tunable. However, their features in dR/dT appear to change with gate voltage corresponding to ferromagnetic or antiferromagnetic transitions at different V_{gate} values. Contrasting, our devices show transport behaviour that remains consistent with an antiferromagnetic transition.

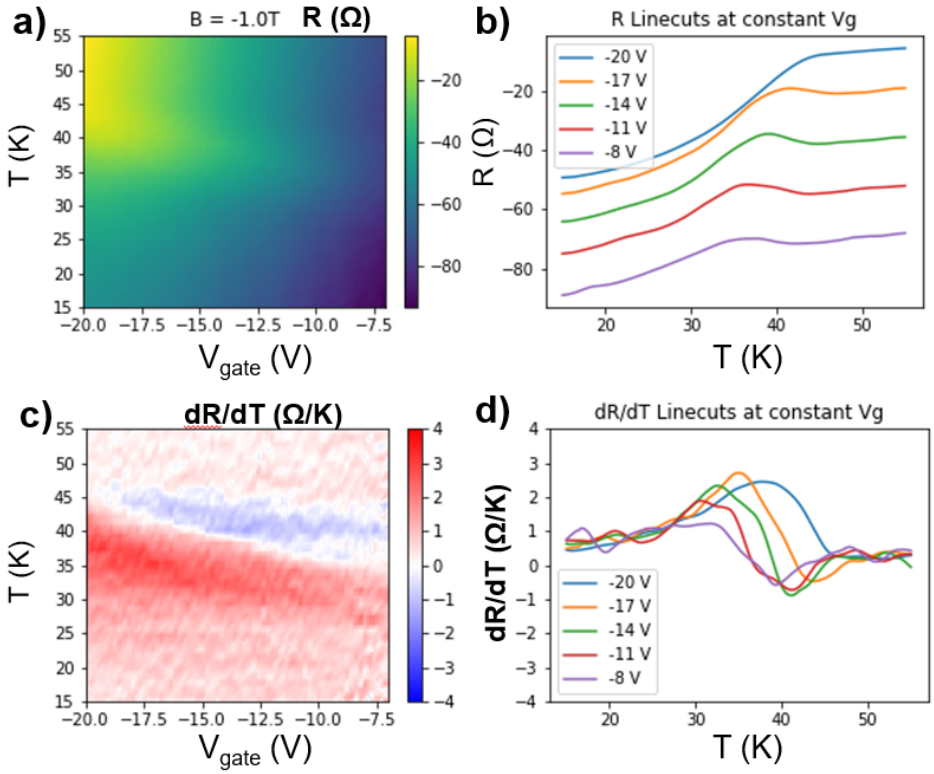

Figure 5.39: Electronic transport in device F1 at $B_\perp$ = -1 T
(a) Resistance vs temperature and V_{gate} in a narrow range (b) Resistance linecuts vs temperature at different V_{gate} values (c) Derivative of resistance dR/dT vs temperature and V_{gate} (d) dR/dT linecuts versus temperature at different V_{gate} values

Applying an out of plane magnetic field $B_\perp$, we observe qualitatively the same behaviour as in the $B_\perp = 0$ case. We still observe the antiferromagnetic transition at the elevated T_N values independent of $B_\perp$. This is expected, since the in plane zigzag antiferromagnetic order in $RuCl_3$ is quite robust to out of plane magnetic fields. S. Baek et al., had demonstrated that even at $B_\perp = 9\ T$, the antiferromagnetic transition was visible in specific heat capacity measurements [116].

Fig. 5.39 summarizes $T - V_{gate}$ characteristics at $B_\perp = -1\ T$. By recording such data at various $B_\perp$ values, we find that the amplitude of the peak-dip feature in dR/dT amplitude gradually reduces as $B_\perp$ is increased. For example, at $V_{gate} = -20\ V$, it

shrinks from 3.5 Ω/K at $B_\perp = 0\ T$ to 2 Ω/K at $B_\perp = -2\ T$. Thus, while the external magnetic field does start to shrink the peak-dip feature associated with antiferromagnetism, the *in-plane* Heisenberg antiferromagnetic interaction is much stronger than the *out of plane* Zeeman interaction.

We record the same dataset also at larger $B_\perp$ values and continue to observe the antiferromagnetic transition. However, beyond ~ -2 Tesla, it becomes difficult to draw quantitative conclusions due to smearing of the data from the onset of the QHE.

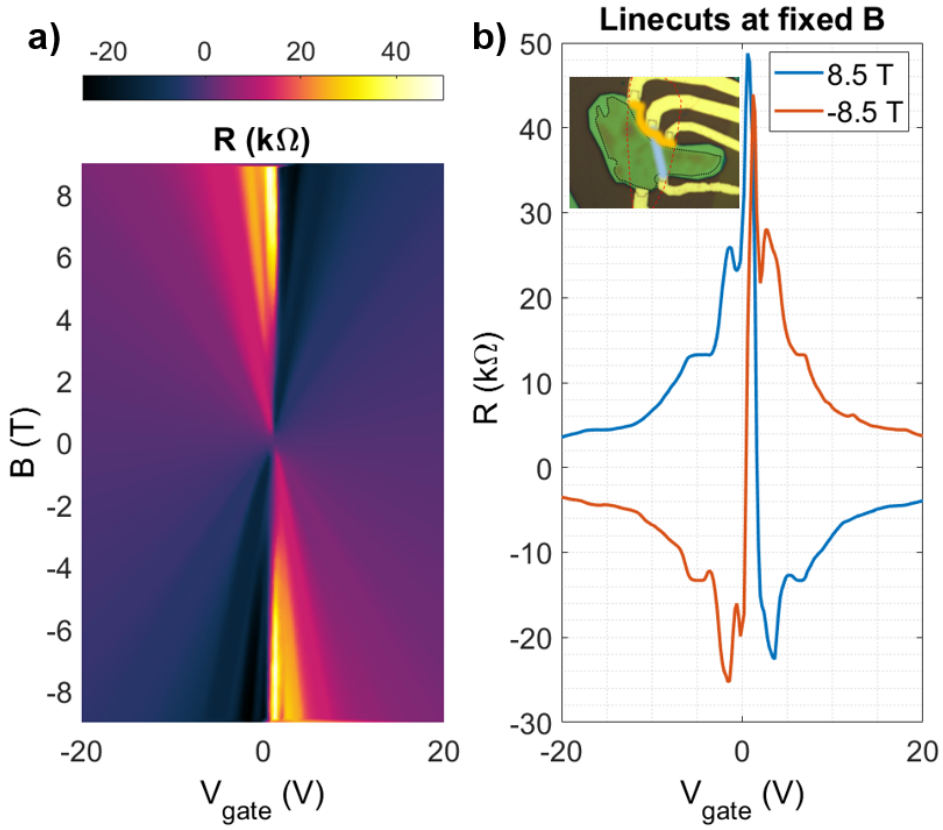

Figure 5.40: The quantum Hall effect under Config 1 in device F1
Colour map in (a) and linecuts in (b) both show the expected symmetries in B and V_{gate}. Inset in (b) highlights the measurement configuration. Blue line indicates the two leads across which current is sourced. Yellow line indicates the voltage measurement leads. The edge connecting the latter does not include the $RuCl_3$ flake.

Quantum Hall data from one *quasi*-R_{xy} configuration is shown in fig. 5.40. The inset of fig. 5.40b highlights this measurement configuration (which we label "Config. 1"). The highlighted *blue* line shows the two leads across which 100 nA of current is sourced. The glowing *yellow* line highlights the edge across which the potential drop is measured.

As can be seen from both the colour map, and line traces at $\pm 8.5\ T$, the resistance

obeys Onsager relation $R_{xy}(-B) = -R_{xy}(B)$. Additionally, the expected electron hole symmetry is also reasonably well observed $R_{xy}(B, -n) \approx -R_{xy}(B, n)$. In summary, the Hall resistance in this Config. 1 matches well with expected quantum Hall behaviour in graphene, with filling factors $\nu = 1$ ($\approx 25\ k\Omega$) and $\nu = 2$ ($\approx 12.5\ k\Omega$) visible from the zeroeth Landau level.

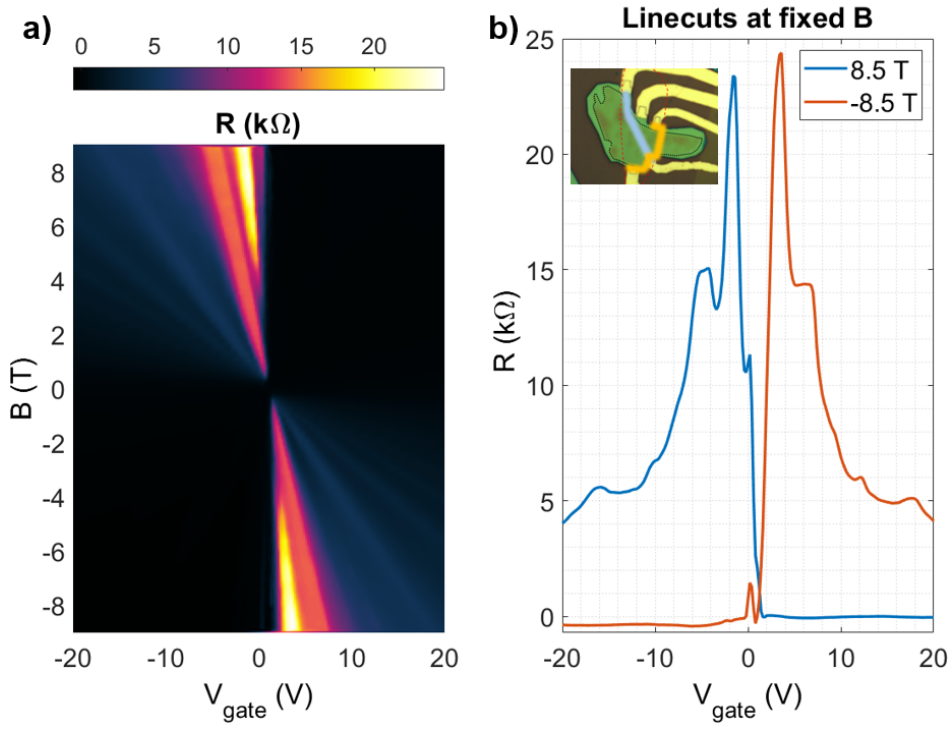

Figure 5.41: The asymmetric quantum Hall effect under Config 2 in device F1 Colour map in (a) has the resistance plateaus missing in the 1^{st} and 3^{rd} quadrants (b) Linecuts at fixed B only demonstrate QHE plateaus for half the V_{gate} range. Inset in (b) highlights the measurement configuration. In this case the measurement happens across an edge that *includes* $RuCl_3$ underneath the graphene

The observations become markedly different when we change configurations. Data from a second measurement configuration ("Config. 2") is shown in fig. 5.41. Inset of fig. 5.41b highlights the terminals across which 100 nA current is sourced (blue glow) and the edge across which the potential drop is measured (yellow glow). In this quasi-R_{xy} configuration, the same filling factors are visible as in Config. 1 but no quantum Hall behaviour is observed in one half of the entire B-V_{gate} space. In fig. 5.41a, the first and third quadrants do not show a quantum Hall behaviour and are instead in a low resistance state.

This observation is not fully understood yet, but the presence of $RuCl_3$ underneath the graphene is undoubtedly the cause of this effect. By varying configurations, we

can access the quantum Hall regime in all four quadrants, or only in the (1^{st}& 3^{rd}) or (2^{nd}& 4^{th}) quadrants.

We find that when we measure along a graphene edge without crossing the $RuCl_3$ flake (such as in Config. 1), the entire quantum Hall spectrum is visible. Note that since the device extends slightly outside the $RuCl_3$ flake, there exists a "graphene only" edge channel in Config. 1 measurement (highlighted in yellow in fig. 5.40b). However, when measuring across an edge such as in Config. 2 (highlighted in yellow in fig. 5.41b), there is conduction along a graphene-$RuCl_3$ edge.

One might postulate that this observation is due to an electrostatic effect between graphene and $RuCl_3$, such as charge transfer between graphene and $RuCl_3$ at certain gate voltages, which would provide an additional parallel channel of low resistance. However, such an effect should only be gate voltage dependent, and independent of the magnetic field. That is, it might explain a case where the (1^{st}& 4^{th}) quadrants were invisible, but not the current behaviour. Our quasi R_{xy} still obeys Onsager relationship: $R_{xy}(-B,\ -n) = R_{xy}(B,\ n)$.

5.6 Concluding Remarks

We attempt to induce the magnetic proximity effect in graphene by fabricating heterostructures with three separate vdW magnets: CrI_3, $CrSiTe_3$, and $RuCl_3$. We fare the worst with CrI_3, where in spite of the cleanest devices and seemingly incorporating the necessary precautions, the CrI_3 completely disintegrates. This further leads to the graphene either being very strongly hole doped, or itself chemically degrading such that we do not observe any graphene like signatures in electron transport. We learnt of another work where via contacts to graphene were unsuccessfully attempted to preserve CrI_3 [131].

In $CrSiTe_3$-graphene heterostructures, we do not find any noticeable degradation in the quality of graphene on SiO_2 than before the transfer of $CrSiTe_3$ on top. In spite of not having a protective top h-BN layer, $CrSiTe_3$ is found to not degrade over more than a month with magneto-optical measurements confirming its magnetic properties. Quantum Hall measurements in $CrSiTe_3$-graphene confirm graphene's high quality, but do not show signatures of spin splitting. A significant enhancement in non local transport was observed in $CrSiTe_3$-graphene compared to graphene only, which could be suggestive of a proximity induced MEF. There are however other observations, which do not completely add up with a true magnetic system, such as a saturation of the MEF at a relatively small external field.

Our results for heterostructures of 2D *ferromagnets* CrI_3 and $CrSiTe_3$ are summarized along with other observations in lierature in table 5.1.

The graphene-$RuCl_3$ system was the most interesting, with a clear signature of a proximity effect in the form of band hybridization between graphene and $RuCl_3$. Our results, along with reports in literature are summarized in table 5.2. We observe

Table 5.1: Comparison of ferromagnet-graphene results with literature

Report	Proximal layer	Magnetic Proximity?	Proximity SOC?	Mobility ($cm^2/V.s$)	Comments
[34],[35]	MoS_2, WS_2, WSe_2	✗	✓	$\sim$ 100,000	Magnetic proximity not expected
[37]	YIG	✓	✓	10,000	AHE observed
[36]	EuS	✓	✗	6,000	SOC surprisingly absent
[119]	CrI_3	✗	✗	200	After 20 minutes exposure to air and light
[131]	CrI_3	✗	✗	N/A	Device degraded before measurement
[131]	$CrCl_3$	✗	✗	$\sim 100,000$	Signal from two carrier transport incorrectly attributed to AHE
This thesis	CrI_3	✗	✗	N/A	Transport inconsistent with graphene
This thesis	$CrSiTe_3$	✗	✗	5,000-10,000	Graphene and $CrSiTe_3$ do not degrade over time $>$ 1 month

signatures of antiferromagnetic transition in electrical transport at elevated Neel temperatures. While we cannot distinguish whether the magnetic signature arises simply from the underlying $RuCl_3$, or is indicative of magnetic order in graphene, the elevated Neel temperature clearly points to some hybrid interaction between graphene and $RuCl_3$, even if only at an *electrostatic* level. The end result is an enhanced, *gate voltage tunable* antiferromagnetic phase in $RuCl_3$ due to proximity coupling to graphene.

The *asymmetric* QHE is an interesting phenomena that requires further investigation. The asymmetric QHE always includes a graphene-$RuCl_3$ edge, as opposed to a "graphene only" edge, when it reverts to the usual QHE. As yet, we are unaware of any other work in literature where such an asymmetry in carrier density and magnetic field was observed. Neither Zhou et al. nor Mashhadi et al. observe the QHE in their graphene-$RuCl_3$ systems[117, 118].

Table 5.2: Comparison of $RuCl_3$-graphene results with literature

Report	Enhanced conductivity?	Magnetic order of $RuCl_3$	T_N/T_c(K)	Quantum Hall?	Magnetic order in graphene?
[117]	✓	AFM ?	10 K	✗	✗
[118]	✓	FM/AFM	(12-35) K	✗	✗
This thesis	✓	AFM	(36-48) K	✓	✗

Chapter 6

Concluding remarks and future Work

In this final chapter, we summarize our results towards achieving a magnetic proximity effect with vdW magnets CrI_3, $CrSiTe_3$, and $RuCl_3$. While we have not yet demonstrated conclusively the emergence of proximity induced magnetic order in graphene, we put forward some ideas that researchers in the future can utilize to further build upon our work. We first discuss new device configuration ideas with the same magnetic vdW materials that we have employed so far. Lastly, different approaches with alternate materials are discussed.

6.1 CrI_3-graphene: Conclusions and future device ideas

Of all the vdW magnet-graphene systems that we studied, CrI_3-graphene devices were by far the worst due to the extreme chemical instability of CrI_3. We attempted to take care of this issue by fabricating doubly encapsulated h-BN-CrI_3-graphene-h-BN devices. In these "type A" devices, electrical contacts to graphene were made prior to assembling the top half h-BNCrI_3 of the device.

A schematic of this idea is once again shown in fig. 6.1a. Our theory is that the degradation of CrI_3 and that of graphene resultantly is due to small pockets that form at the edges where the metal and h-BN flakes overlap. We highlight this in fig. 6.1b for device A1 with dotted red circles. Even though the CrI_3 flake is seemingly safely encapsulated (black dotted flake in fig. 6.1b), results from our devices show that this is clearly not the case.

Our idea could be further improved by the following two techniques:

i) Via contacts to graphene through the top h-BN flake

ii) Graphite contacts to graphene at a large lateral distance away from CrI_3.

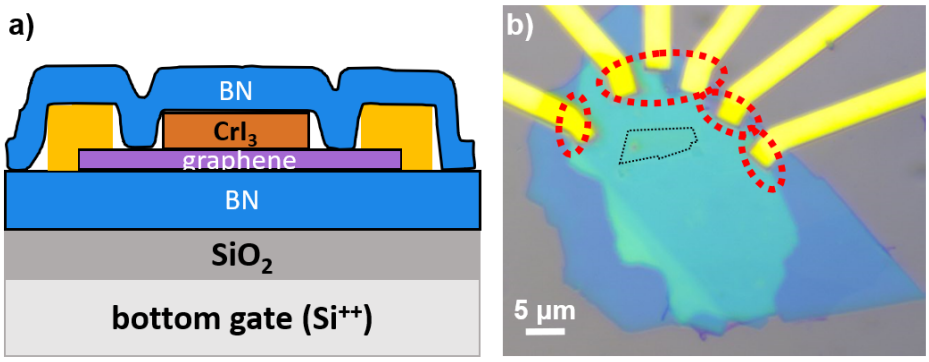

Figure 6.1: Degradation from tenting effects in "type A" devices
(a) Schematic of a completed "type A" device (b) Optical image of device A1. Red dotted circles indicate regions where the thick metal overlaps with the top h-BN flake, causing a tenting effect and leading to open pockets for moisture to seep in. Black dotted lines outline the CrI_3flake.

6.1.1 Via contacts to graphene-CrI_3devices

Recently, it was demonstrated that via contacts are a powerful approach towards making electrical contacts to vdW systems where one or more materials are chemically sensitive [132]. The original idea was implemented to vdW superconductor $NbSe_2$ but could be applied to a graphene-CrI_3 system as well.

In via contacts, elliptic/rectangular holes are first etched into a top h-BN flake that is exfoliated onto a Si substrate. Next Au metallic leads are evaporated on it to fill the etched holes. Note that no adhesion layer of Cr is utilized to ensure that Au does not stick to the Si substrate. Now, the usual vdW assembly can be performed using this h-BN flake as the top most layer and aligning it precisely with the underlying layer so that electrical contact is made to the material of interest.

This idea is illustrated in fig. 6.2. This idea should be an improvement over our "type A" devices as there should not exist any *macroscopic* air pockets. The etched holes in the top h-BN flakes should be completely filled by the evaporated Au metal save for microscopic openings associated with roughness of Au.

A downside of this technique is that the encapsulated CrI_3would still be exposed to the nanofabrication steps as a final lithography plus metal evaporation step is required to connect the via contacts on the device with bond pads on the Si substrate.

We have successfully implemented this via approach in a "graphene only" device to ensure that we can replicate this technique, but haven't implemented this idea to a graphene-CrI_3 system yet. While we haven't yet tested this idea on graphene-CrI_3 heterostructure ourselves, we did find a recent report where this technique was *unsuccessfully* implemented[131]. The author demonstrated in his report that due to the *microscopic* openings arising from the roughness of metallic Au, moisture was able to seep in, and completely degrade the CrI_3 in a matter of minutes (section 5.5

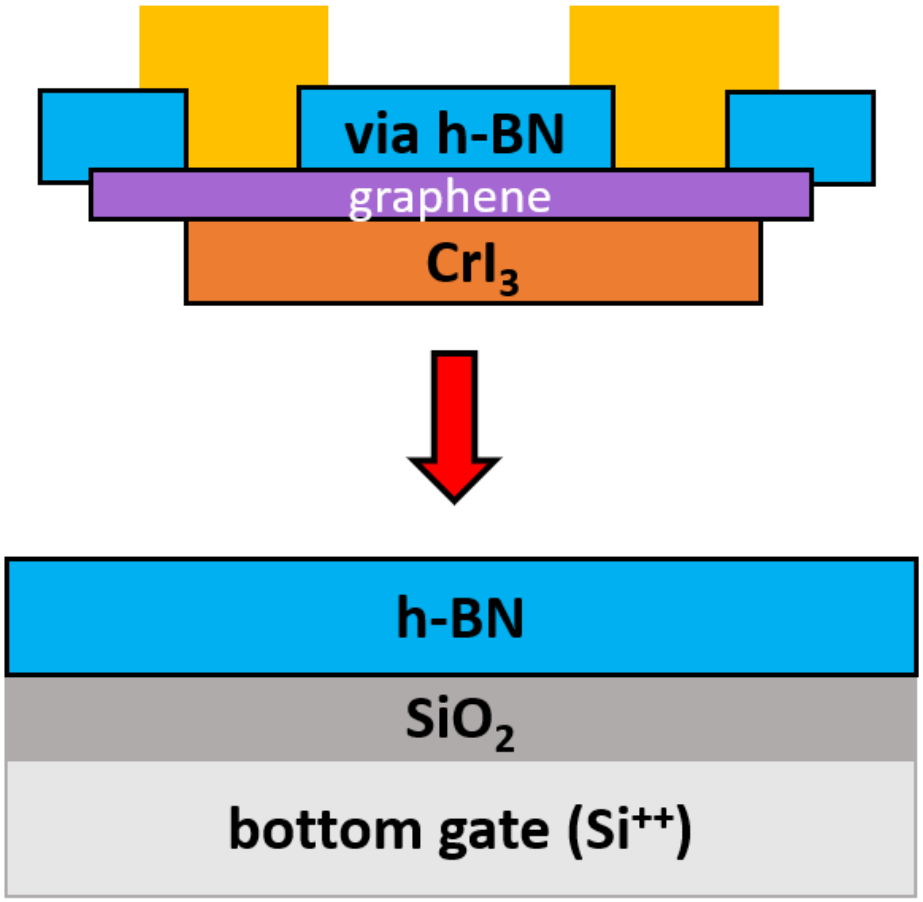

Figure 6.2: Making via contacts to graphene-CrI_3 system.

in ref. [131]).

6.1.2 Graphite contacts to graphene

An encouraging recent result in literature has been the demonstration of tunneling magnetoresistance in CrI_3 based devices. Since CrI_3 is a layered ferromagnetic with antiferromagnetic interlayer coupling, bilayer CrI_3 will have a large (small) associated tunneling magnetoresistance depending on whether the spins in the two layers are anti-aligned (aligned). This result was successfully demonstrated by four separate works using electrical transport [133, 134, 135, 136].

In each of those works, the authors utilized multilayer graphene (or graphite) flakes above and below CrI_3 flakes of varying thickness (two, three, four etc. layers). The graphite flakes extended laterally over some distance, where finally metallic contacts were evaporated to connect the graphite leads with bond pads. The devices were also

doubly encapsulated in h-BN.

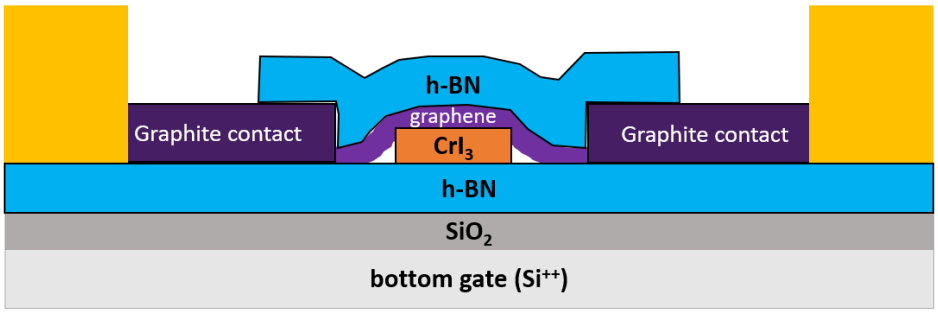

Figure 6.3: Schematic: Making electrical contacts to graphene using graphite flakes in a graphene-CrI_3 system.
Note that the graphite flakes extend further out than the top h-BN so that the h-BN flake does not have to fold over thick metal leads

Such an idea could be extended to a graphene-CrI_3 vdW heterostructure and is illustrated in fig. 6.3. Two (or more) graphite contacts can electrically touch graphene and extend out wide as shown. The graphene-CrI_3 heterostructure is completely encapsulated with top and bottom h-BN flakes. Having said that, it is crucial that the graphite contacts extend out further than the top h-BN flakes. This ensures that the h-BN-graphite-graphene-CrI_3-h-BN heterostructure is *all van der Waals* and should be devoid of any microscopic air pockets, due to the atomic flatness of vdW materials.

There are no reports in literature where this idea has been implemented successfully or unsuccessfully to graphene-CrI_3 proximity devices. Keeping in mind the successful implementation of CrI_3 in transport devices for the tunneling experiments, this approach might be researchers' best bet with regards to creating a graphene-CrI_3 device that does not degrade. There is still the second hurdle of whether a sufficient MEF would even be induced in graphene and if any discernible effects could be observed. But so far even the first hurdle with graphene-CrI_3 devices of creating a non degrading system has yet to be realized. Implementing graphite contacts is likely the best approach in this direction.

6.2 $CrSiTe_3$-graphene: Conclusions and future device ideas

From our experience with fabricating $CrSiTe_3$-graphene devices ('type "C", "D", and "E" devices in sec. 5.4), $CrSiTe_3$ was clearly a far more forgiving material than CrI_3 in terms of chemical stability. Indeed, our $CrSiTe_3$-graphene devices all exhibited transport characteristics consistent with graphene behaviour, with negligible degradation in graphene mobility (less than 20%) in graphene-SiO_2 devices after $CrSiTe_3$ transfer.

Thus, we believe that the $CrSiTe_3$-graphene system is much more likely to succeed than the CrI_3-graphene as far as observing a proximity induced MEF goes.

The concern currently with $CrSiTe_3$-graphene devices is the absence of any *obvious* proximity induced magnetic order in graphene. We suggest improvements upon our ideas that would be more conducive towards successfully achieving a MEF in $CrSiTe_3$-graphene heterostructures.

6.2.1 Symmetric $CrSiTe_3$-graphene-$CrSiTe_3$ devices

Perhaps the most important factor when inducing a proximity effect is the interlayer spacing between neighbouring materials. The strength of the induced MEF increases exponentially with decreasing interlayer spacing between graphene and the vdW magnet.

In our "type D" h-BN-graphene-$CrSiTe_3$ devices, a concern is that the presence of h-BN might be counter productive. It is well known that a graphene-hBN interface leads to a stable, lower energy ground state where graphene's π bands hybridize with h-BN, opening up a band gap[31, 32].

It is possible as a result that this h-BN-graphene proximity interaction could compete with the desired graphene-$CrSiTe_3$ proximity interaction. To subvert this issue, we propose a *symmetric* $CrSiTe_3$-graphene-$CrSiTe_3$ heterostructure which not only doubles the strength of MEF that should arise, but also ensures no other competing interactions exist.

A schematic of such a device is shown in fig. 6.4. Keeping in mind that $CrSiTe_3$ has a chemically sensitive nature, we propose a device that is encapsulated in h-BN for protection, that is then edge contacted. The only challenge we foresee with this device geometry at the moment is the failure rate associated with "picking up" $CrSiTe_3$ for van der Waals stacking. In our vdW assembly, our success rate with $CrSiTe_3$ pickup is $\sim 20\%$, which is compounded if two $CrSiTe_3$ pickups are required for the same device.

However, by either brute forcing multiple attempts at picking up $CrSiTe_3$, or dividing the entire vdW assembly into two separate half steps, this device geometry could be achieved and is a promising idea to increase the strength of induced MEF.

6.2.2 Enhancing proximity interactions by adding pressure

It was recently shown by ref. [137] that compressive strain could be used to reduce interlayer spacing, and hence, strongly enhance proximity interactions in vdW heterostructures. This was achieved by loading the vdW device inside a pressure cell and applying a pressure $P \sim 2\ GPa$. The authors demonstrated significantly enhanced superlattice interactions in h-BN-graphene-h-BN [137]. This idea is illustrated in fig. 6.5b.

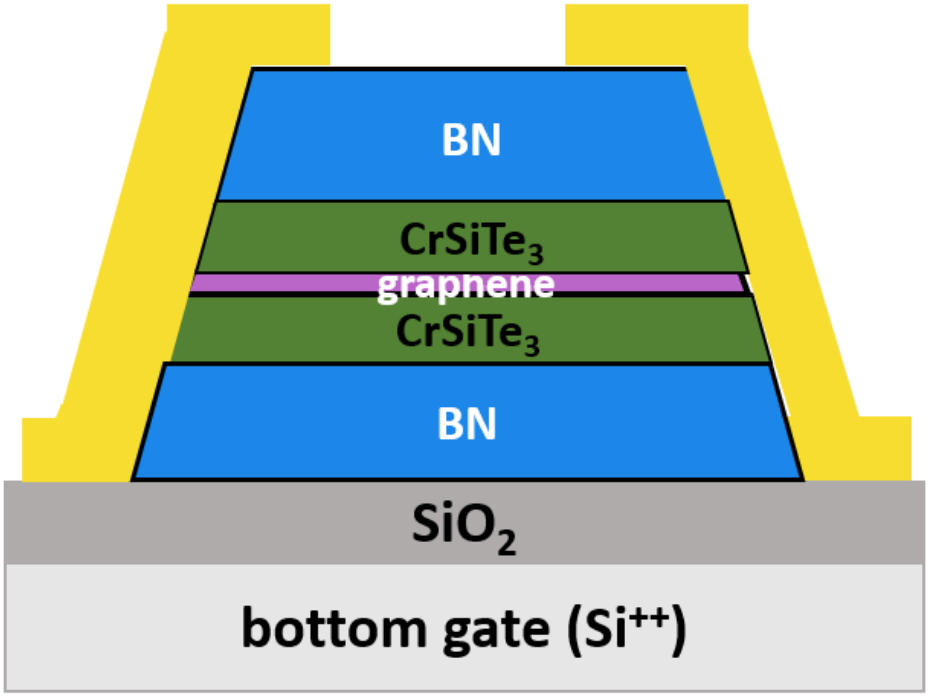

Figure 6.4: Schematic of a symmetric edge contacted $CrSiTe_3$-graphene-$CrSiTe_3$ device

Later, this idea was extended to twisted bilayer graphene, with the idea of enhancing electron-electron interactions between the two graphene monolayers. The authors demonstrated the unconventional superconductivity that occurs in this system to occur at twist angles $\approx$ 1.3°, greater than the conventional 1.1° "magic angle"[138].

We believe that pressure could be utilized to enhance the magnetic exchange interactions in vdW magnet-graphene systems and suggest the above mentioned symmetric $CrSiTe_3$-graphene-$CrSiTe_3$ system as the idea platform to apply this idea (fig. 6.5a). We have demonstrated in this thesis so far that the quality of graphene, $CrSiTe_3$, and the interface are not the issue in $CrSiTe_3$-graphene systems. The absence of any magnetic proximity effects likely stem from a magnetic exchange that is not strong enough.

Thus using a pressure cell such as one utilized in ref. [137] is very likely to sufficiently enhance the magnetic proximity interactions between graphene and $CrSiTe_3$, and most certainly lead to physically observable phenomena in electronic transport.

6.3 $RuCl_3$-graphene: Conclusions and future work

Of the three vdW magnet-graphene systems we have studied, the $RuCl_3$-graphene system has clearly proven to be the most interesting. In our opinion, it is the $RuCl_3$-

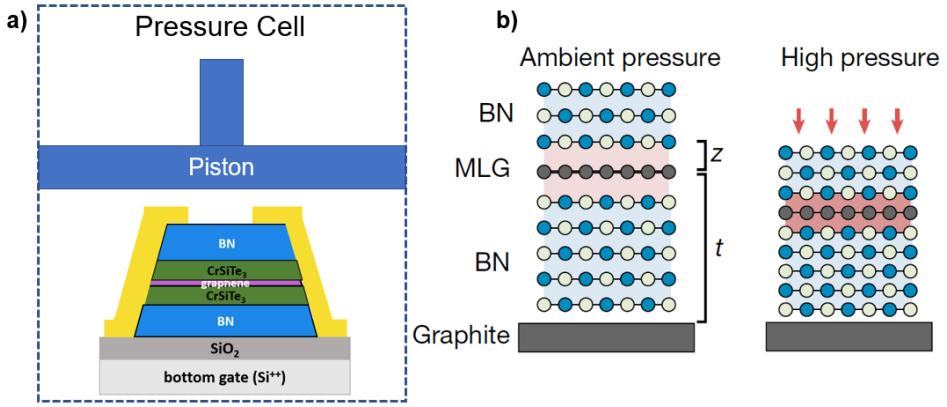

Figure 6.5: Using large pressure to enhance interlayer interactions in $CrSiTe_3$-graphene-$CrSiTe_3$ devices
(a) Schematic of a symmetric $CrSiTe_3$-graphene-$CrSiTe_3$ device inside a pressure cell (b) Reduction in interlayer spacing under high pressure. Panel (b) borrowed from ref. [137].

graphene system that deserves the most attention in any future work studying vdW heterostructures of 2D magnets and graphene.

While we do not observe signatures of *magnetic* proximity effects in graphene, there are clear signatures of proximity effects and band hybridization in the $RuCl_3$-graphene system.

First and foremost, we observe an enhanced electronic conductivity in the system, with resistances an order of magnitude lower than expected in similar graphene devices. $RuCl_3$ is a Mott insulator, so this enhanced conductivity in $RuCl_3$-graphene is impossible without the presence of proximity induced band hybridization between $RuCl_3$ and graphene.

The band hybridization furthermore leads to an enhanced antiferromagnetic order that is gate voltage tunable. As opposed to the implicit $T_N = 7\ K$ or $14\ K$ of $RuCl_3$, we are able to tune T_N between $36\ K$ and $48\ K$. We have reproduced these results in a second $RuCl_3$-graphene device where both the enhanced conductivity and enhanced antiferromagnetic order (with identical control over T_N with similar gate voltages) were observed.

Our results share some common features and some disagreements with the work presented in ref. [118] on $RuCl_3$-graphene. Like us, they also observe an enhanced critical temperature ($12 - 35\ K$) which is gate voltage tunable. However, at some gate voltages, they observe a *ferromagnetic* order and at other gate voltages an *antiferromagnetic* order .

Since there are some open questions with regards to the magnetic ground state of $RuCl_3$-graphene system, we are currently in the midst of performing magneto-optical characterization of our $RuCl_3$-graphene devices, which will be another independent

measurement of the magnetic order in these devices.

Lastly, future work will also aim to examine the quantum Hall regime in these devices, where quantum Hall plateaus associated with holes (electrons) were invisible for positive (negative) values of $B_\perp$. We were unable to test this in our second device due to the availability of only three leads, which prevented us from performing four-terminal R_{xx}/R_{xy} measurements.

6.4 Other material systems and approaches

In this section, we discuss some ideas beyond the three vdW magnetic systems that we have so far considered in this thesis. There exist a plethora of layered magnetic materials today. For example, ref. [24] reported 38 different vdW magnets two years ago, with the number even greater today. As a result, it is imperative that the material systems be carefully chosen, keeping in mind the desired properties.

6.4.1 Large scale growth of vdW magnet-graphene heterostructures

Our approaches towards realizing a magnetic proximity effect were limited to a *top-down* approach of cleaving layered materials and assembling vdW heterostructures out of them. Alternatively, bottom-up approaches towards this goal could be attempted. This was the case for the EuS-graphene system that we discussed in sec. 4.2.1[36].

Even though EuS itself is a three dimensional material, successful large scale growth of *two dimensional* magnetic layers has now been achieved. For example, D. O'Hara et al. demonstrate ferromagnetism at room temperature in monolayer $MnSe_2$ via molecular beam epitaxy[139].

Even if a step by step heterostructure of graphene on a vdW magnet (or vice versa) cannot be directly grown, large area graphene films grown via CVD can be transfered onto two dimensional magnetic substrates. As was shown in the work of EuS-graphene and graphene-YIG, such techniques do not significantly degrade the graphene quality. The up side of this approach is it allows simultaneous fabrication of a large number of devices. The focus with such a work can thus be to simply search for signatures of magnetic proximity effects, while the quality of graphene can be optimized later.

6.4.2 Magnetism in twisted bilayer graphene

Recently two experimental results emerged in literature where magnetic order was observed in twisted bilayer graphene (tBLG)[40, 41]. First, A. Sharpe et al. reported observed magnetic hysteresis and the AHE in tBLG near three quarters filling of the mini Brillouin zone of tBLG[40]. At first sight, this is a surprising result since the

system is defect free, and does not possess any obvious means of creating a magnetic exchange interaction such as magnetic dopants. Instead, this magnetic order arises from strongly correlated electron behaviour. The tBLG samples were encapsulated in top and bottom h-BN flakes, and it seems important that one of the graphene sheets be in near alignment with its neighbouring h-BN layer. This has the effect of breaking the fourfold spin and valley degeneracies in tBLG. Thus, at three quarters filling, the ground state is spin and valley polarized.

M. Serlin et al. demonstrated the quantum anomalous Hall effect in tBLG with $R_{xy} = h/e^2$ corresponding to Chern number $C = 1$ in the absence of an external magnetic field[41]. Outside of the magnetic doped thin films of 3D topological insulators, this is the only other system where the quantum anomalous Hall effect has been demonstrated. The quantum anomalous Hall state is much more robust to temperature, with near perfect quantization at $T = 3\ K$, $\sim$ 100 times higher than the topological insulator films. While a detailed theory does not yet exist, it is believed that the topological order arises from the near perfect alignment of one graphene layer with its neighbouring h-BN layer.

With these two new experimental results in mind, tBLG is undoubtedly the most promising two dimensional "magnetic" system. Introducing a near precise twist angle $\approx 1.15° - 1.20°$ is not a big technical challenge, with multiple groups successfully achieving tBLG devices. The chemical stability of graphene eliminates any experimental challenges associated with chemical degradation that have been the biggest roadblocks in our more conventional vdW magnet-graphene proximity devices. This is a huge positive.

In closing, while attempting to introduce a proximity induced MEF in *monolayer* graphene, we encountered two *major* experimental challenges. The first is associated with the quality of vdW magnets and interfaces. Secondly, the strength of any induced MEF in clean 2D ferromagnet-graphene ($CrSiTe_3$-graphene) devices does not appear to be as strong as predicted theoretically to have clear cut experimental signatures. We have made significant progress towards resolving these issues. Yet, some hurdles still exist, especially in CrI_3-graphene.

The most recent results showcasing interfacial physics in the $RuCl_3$-graphene system are extremely encouraging, and will be the focus of attention in the immediate future. Combined with results from other research groups, particularly for the twisted bilayer system, we do believe that the future is bright for magnetism in graphene based systems. The era of 2D magnetism has only just begun.

Bibliography

[1] Devashish P. Gopalan, Patrick C. Mende, Sergio C. de la Barrera, Shonali Dhingra, Jun Li, Kehao Zhang, Nicholas A. Simonson, Joshua A. Robinson, Ning Lu, Qingxiao Wang, Moon J. Kim, Brian D'Urso, and Randall M. Feenstra. Formation of hexagonal boron nitride on graphene-covered copper surfaces. *Journal of Materials Research*, 31(7):945–958, April 2016.

[2] Raghav Garg, Devashish P. Gopalan, Sergio C. de la Barrera, Hasnain Hafiz, Noel T. Nuhfer, Venkatasubramanian Viswanathan, Benjamin M. Hunt, and Tzahi Cohen-Karni. Electron Transport in Multidimensional Fuzzy Graphene Nanostructures. *Nano Letters*, July 2019.

[3] Sergio C. de la Barrera, Michael R. Sinko, Devashish P. Gopalan, Nikhil Sivadas, Kyle L. Seyler, Kenji Watanabe, Takashi Taniguchi, Adam W. Tsen, Xiaodong Xu, Di Xiao, and Benjamin M. Hunt. Tuning Ising superconductivity with layer and spin–orbit coupling in two-dimensional transition-metal dichalcogenides. *Nature Communications*, 9(1):1–8, April 2018.

[4] Brodie Benjamin Collins. XIII. On the atomic weight of graphite. *Philosophical Transactions of the Royal Society of London*, 149:249–259, January 1859.

[5] A. K. Geim. Graphene prehistory. *Physica Scripta*, T146:014003, January 2012.

[6] H. P. Boehm, A. Clauss, G. O. Fischer, and U. Hofmann. Das Adsorptionsverhalten sehr dünner Kohlenstoff-Folien. *Zeitschrift für anorganische und allgemeine Chemie*, 316(3-4):119–127, 1962.

[7] H. P. Boehm, R. Setton, and E. Stumpp. Nomenclature and terminology of graphite intercalation compounds. *Carbon*, 24(2):241–245, January 1986.

[8] Sidney Coleman. There are no Goldstone bosons in two dimensions. *Communications in Mathematical Physics*, 31(4):259–264, December 1973.

[9] N. D. Mermin and H. Wagner. Absence of Ferromagnetism or Antiferromagnetism in One- or Two-Dimensional Isotropic Heisenberg Models. *Physical Review Letters*, 17(22):1133–1136, November 1966.

[10] A. Fasolino, J. H. Los, and M. I. Katsnelson. Intrinsic ripples in graphene. *Nature Materials*, 6(11):858–861, November 2007.

[11] K. S. Novoselov, A. K. Geim, S. V. Morozov, D. Jiang, Y. Zhang, S. V. Dubonos, I. V. Grigorieva, and A. A. Firsov. Electric Field Effect in Atomically Thin Carbon Films. *Science*, 306(5696):666–669, October 2004.

[12] Yuanbo Zhang, Yan-Wen Tan, Horst L. Stormer, and Philip Kim. Experimental observation of the quantum Hall effect and Berry's phase in graphene. *Nature*, 438(7065):201–204, November 2005.

[13] C. R. Dean, A. F. Young, I. Meric, C. Lee, L. Wang, S. Sorgenfrei, K. Watanabe, T. Taniguchi, P. Kim, K. L. Shepard, and J. Hone. Boron nitride substrates for high-quality graphene electronics. *Nature Nanotechnology*, 5(10):722–726, October 2010.

[14] Jiamin Xue, Javier Sanchez-Yamagishi, Danny Bulmash, Philippe Jacquod, Aparna Deshpande, K. Watanabe, T. Taniguchi, Pablo Jarillo-Herrero, and Brian J. LeRoy. Scanning tunnelling microscopy and spectroscopy of ultra-flat graphene on hexagonal boron nitride. *Nature Materials*, 10(4):282–285, April 2011.

[15] Sajedeh Manzeli, Dmitry Ovchinnikov, Diego Pasquier, Oleg V. Yazyev, and Andras Kis. 2D transition metal dichalcogenides. *Nature Reviews Materials*, 2(8):17033, August 2017.

[16] Xiaoxiang Xi, Zefang Wang, Weiwei Zhao, Ju-Hyun Park, Kam Tuen Law, Helmuth Berger, László Forró, Jie Shan, and Kin Fai Mak. Ising pairing in superconducting $NbSe_2$ atomic layers. *Nature Physics*, 12(2):139–143, February 2016.

[17] A. W. Tsen, B. Hunt, Y. D. Kim, Z. J. Yuan, S. Jia, R. J. Cava, J. Hone, P. Kim, C. R. Dean, and A. N. Pasupathy. Nature of the quantum metal in a two-dimensional crystalline superconductor. *Nature Physics*, 12(3):208–212, March 2016.

[18] Efrén Navarro-Moratalla, Joshua O. Island, Samuel Mañas-Valero, Elena Pinilla-Cienfuegos, Andres Castellanos-Gomez, Jorge Quereda, Gabino Rubio-Bollinger, Luca Chirolli, Jose Angel Silva-Guillén, Nicolás Agraït, Gary A. Steele, Francisco Guinea, Herre S. J. van der Zant, and Eugenio Coronado. Enhanced superconductivity in atomically thin TaS_2. *Nature Communications*, 7:11043, March 2016.

[19] Cheng Gong, Lin Li, Zhenglu Li, Huiwen Ji, Alex Stern, Yang Xia, Ting Cao, Wei Bao, Chenzhe Wang, Yuan Wang, Z. Q. Qiu, R. J. Cava, Steven G. Louie,

Jing Xia, and Xiang Zhang. Discovery of intrinsic ferromagnetism in two-dimensional van der Waals crystals. *Nature*, 546(7657):265–269, June 2017.

[20] Bevin Huang, Genevieve Clark, Efrén Navarro-Moratalla, Dahlia R. Klein, Ran Cheng, Kyle L. Seyler, Ding Zhong, Emma Schmidgall, Michael A. McGuire, David H. Cobden, Wang Yao, Di Xiao, Pablo Jarillo-Herrero, and Xiaodong Xu. Layer-dependent ferromagnetism in a van der Waals crystal down to the monolayer limit. *Nature*, 546(7657):270–273, June 2017.

[21] Nikhil Sivadas, Matthew W. Daniels, Robert H. Swendsen, Satoshi Okamoto, and Di Xiao. Magnetic ground state of semiconducting transition-metal trichalcogenide monolayers. *Physical Review B*, 91(23):235425, June 2015.

[22] J. F. Dillon and C. E. Olson. Magnetization, Resonance, and Optical Properties of the Ferromagnet CrI_3. *Journal of Applied Physics*, 36(3):1259–1260, March 1965.

[23] Nikhil Sivadas, Satoshi Okamoto, Xiaodong Xu, Craig. J. Fennie, and Di Xiao. Stacking-Dependent Magnetism in Bilayer CrI_3. *Nano Letters*, 18(12):7658–7664, December 2018.

[24] Michael A. McGuire. Crystal and Magnetic Structures in Layered, Transition Metal Dihalides and Trihalides. *Crystals*, 7(5):121, May 2017.

[25] V. Carteaux, G. Ouvrard, J. C. Grenier, and Y. Laligant. Magnetic structure of the new layered ferromagnetic chromium hexatellurosilicate $Cr_2Si_2Te_6$. *Journal of Magnetism and Magnetic Materials*, 94(1):127–133, March 1991.

[26] L. D. Casto, A. J. Clune, M. O. Yokosuk, J. L. Musfeldt, T. J. Williams, H. L. Zhuang, M.-W. Lin, K. Xiao, R. G. Hennig, B. C. Sales, J.-Q. Yan, and D. Mandrus. Strong spin-lattice coupling in $CrSiTe_3$. *APL Materials*, 3(4):041515, March 2015.

[27] A. Banerjee, C. A. Bridges, J.-Q. Yan, A. A. Aczel, L. Li, M. B. Stone, G. E. Granroth, M. D. Lumsden, Y. Yiu, J. Knolle, S. Bhattacharjee, D. L. Kovrizhin, R. Moessner, D. A. Tennant, D. G. Mandrus, and S. E. Nagler. Proximate Kitaev quantum spin liquid behaviour in a honeycomb magnet. *Nature Materials*, 15(7):733–740, July 2016.

[28] R. M. Feenstra, Debdeep Jena, and Gong Gu. Single-particle tunneling in doped graphene-insulator-graphene junctions. *Journal of Applied Physics*, 111(4):043711, February 2012.

[29] Marco M. Furchi, Florian Höller, Lukas Dobusch, Dmitry K. Polyushkin, Simone Schuler, and Thomas Mueller. Device physics of van der Waals heterojunction solar cells. *NPJ 2D Materials and Applications*, 2(1):1–7, February 2018.

[30] A. K. Geim and I. V. Grigorieva. Van der Waals heterostructures. *Nature*, 499(7459):419–425, July 2013.

[31] B. Hunt, J. D. Sanchez-Yamagishi, A. F. Young, M. Yankowitz, B. J. LeRoy, K. Watanabe, T. Taniguchi, P. Moon, M. Koshino, P. Jarillo-Herrero, and R. C. Ashoori. Massive Dirac Fermions and Hofstadter Butterfly in a van der Waals Heterostructure. *Science*, 340(6139):1427–1430, June 2013.

[32] C. R. Dean, L. Wang, P. Maher, C. Forsythe, F. Ghahari, Y. Gao, J. Katoch, M. Ishigami, P. Moon, M. Koshino, T. Taniguchi, K. Watanabe, K. L. Shepard, J. Hone, and P. Kim. Hofstadter's butterfly and the fractal quantum Hall effect in moiré superlattices. *Nature*, 497(7451):598–602, May 2013.

[33] Zhe Wang, Dong-Keun Ki, Hua Chen, Helmuth Berger, Allan H. MacDonald, and Alberto F. Morpurgo. Strong interface-induced spin–orbit interaction in graphene on WS_2. *Nature Communications*, 6:8339, September 2015.

[34] Zhe Wang, Dong-Keun Ki, Jun Yong Khoo, Diego Mauro, Helmuth Berger, Leonid S. Levitov, and Alberto F. Morpurgo. Origin and Magnitude of 'Designer' Spin-Orbit Interaction in Graphene on Semiconducting Transition Metal Dichalcogenides. *Physical Review X*, 6(4):041020, October 2016.

[35] J. O. Island, X. Cui, C. Lewandowski, J. Y. Khoo, E. M. Spanton, H. Zhou, D. Rhodes, J. C. Hone, T. Taniguchi, K. Watanabe, L. S. Levitov, M. P. Zaletel, and A. F. Young. Spin–orbit-driven band inversion in bilayer graphene by the van der Waals proximity effect. *Nature*, 571(7763):85–89, July 2019.

[36] Peng Wei, Sunwoo Lee, Florian Lemaitre, Lucas Pinel, Davide Cutaia, Wujoon Cha, Ferhat Katmis, Yu Zhu, Donald Heiman, James Hone, Jagadeesh S. Moodera, and Ching-Tzu Chen. Strong interfacial exchange field in the graphene/EuS heterostructure. *Nature Materials*, 15(7):711–716, July 2016.

[37] Zhiyong Wang, Chi Tang, Raymond Sachs, Yafis Barlas, and Jing Shi. Proximity-Induced Ferromagnetism in Graphene Revealed by the Anomalous Hall Effect. *Physical Review Letters*, 114(1):016603, January 2015.

[38] Yuan Cao, Valla Fatemi, Ahmet Demir, Shiang Fang, Spencer L. Tomarken, Jason Y. Luo, Javier D. Sanchez-Yamagishi, Kenji Watanabe, Takashi Taniguchi, Efthimios Kaxiras, Ray C. Ashoori, and Pablo Jarillo-Herrero. Correlated insulator behaviour at half-filling in magic-angle graphene superlattices. *Nature*, 556(7699):80–84, April 2018.

[39] Yuan Cao, Valla Fatemi, Shiang Fang, Kenji Watanabe, Takashi Taniguchi, Efthimios Kaxiras, and Pablo Jarillo-Herrero. Unconventional superconductivity in magic-angle graphene superlattices. *Nature*, 556(7699):43–50, April 2018.

[40] Aaron L. Sharpe, Eli J. Fox, Arthur W. Barnard, Joe Finney, Kenji Watanabe, Takashi Taniguchi, M. A. Kastner, and David Goldhaber-Gordon. Emergent ferromagnetism near three-quarters filling in twisted bilayer graphene. *Science*, page eaaw3780, August 2019.

[41] M. Serlin, C. L. Tschirhart, H. Polshyn, Y. Zhang, J. Zhu, K. Watanabe, T. Taniguchi, L. Balents, and A. F. Young. Intrinsic quantized anomalous Hall effect in a moiré heterostructure. *arXiv:1907.00261 [cond-mat]*, June 2019. arXiv: 1907.00261.

[42] L. Britnell, R. V. Gorbachev, R. Jalil, B. D. Belle, F. Schedin, A. Mishchenko, T. Georgiou, M. I. Katsnelson, L. Eaves, S. V. Morozov, N. M. R. Peres, J. Leist, A. K. Geim, K. S. Novoselov, and L. A. Ponomarenko. Field-Effect Tunneling Transistor Based on Vertical Graphene Heterostructures. *Science*, 335(6071):947–950, February 2012.

[43] L. Britnell, R. V. Gorbachev, A. K. Geim, L. A. Ponomarenko, A. Mishchenko, M. T. Greenaway, T. M. Fromhold, K. S. Novoselov, and L. Eaves. Resonant tunnelling and negative differential conductance in graphene transistors. *Nature Communications*, 4:1794, April 2013.

[44] Sergio C. de la Barrera, Qin Gao, and Randall M. Feenstra. Theory of graphene–insulator–graphene tunnel junctions. *Journal of Vacuum Science & Technology B*, 32(4):04E101, April 2014.

[45] Xuesong Li, Weiwei Cai, Jinho An, Seyoung Kim, Junghyo Nah, Dongxing Yang, Richard Piner, Aruna Velamakanni, Inhwa Jung, Emanuel Tutuc, Sanjay K. Banerjee, Luigi Colombo, and Rodney S. Ruoff. Large-Area Synthesis of High-Quality and Uniform Graphene Films on Copper Foils. *Science*, 324(5932):1312–1314, June 2009.

[46] Ki Kang Kim, Allen Hsu, Xiaoting Jia, Soo Min Kim, Yumeng Shi, Mario Hofmann, Daniel Nezich, Joaquin F. Rodriguez-Nieva, Mildred Dresselhaus, Tomas Palacios, and Jing Kong. Synthesis of Monolayer Hexagonal Boron Nitride on Cu Foil Using Chemical Vapor Deposition. *Nano Letters*, 12(1):161–166, January 2012.

[47] Lijie Ci, Li Song, Chuanhong Jin, Deep Jariwala, Dangxin Wu, Yongjie Li, Anchal Srivastava, Z. F. Wang, Kevin Storr, Luis Balicas, Feng Liu, and Pulickel M. Ajayan. Atomic layers of hybridized boron nitride and graphene domains. *Nature Materials*, 9(5):430–435, May 2010.

[48] Xuesong Li, Weiwei Cai, Luigi Colombo, and Rodney S. Ruoff. Evolution of Graphene Growth on Ni and Cu by Carbon Isotope Labeling. *Nano Letters*, 9(12):4268–4272, December 2009.

[49] Guangyuan Lu, Tianru Wu, Qinghong Yuan, Huishan Wang, Haomin Wang, Feng Ding, Xiaoming Xie, and Mianheng Jiang. Synthesis of large single-crystal hexagonal boron nitride grains on Cu–Ni alloy. *Nature Communications*, 6:6160, January 2015.

[50] A. Nagashima, N. Tejima, Y. Gamou, T. Kawai, and C. Oshima. Electronic dispersion relations of monolayer hexagonal boron nitride formed on the Ni(111) surface. *Physical Review B*, 51(7):4606–4613, February 1995.

[51] W. Auwärter, M. Muntwiler, J. Osterwalder, and T. Greber. Defect lines and two-domain structure of hexagonal boron nitride films on Ni(111). *Surface Science*, 545(1):L735–L740, November 2003.

[52] Willi Auwärter, Hans Ulrich Suter, Hermann Sachdev, and Thomas Greber. Synthesis of One Monolayer of Hexagonal Boron Nitride on Ni(111) from B-Trichloroborazine $(ClBNH)_3$. *Chemistry of Materials*, 16(2):343–345, January 2004.

[53] Alfonso Reina, Xiaoting Jia, John Ho, Daniel Nezich, Hyungbin Son, Vladimir Bulovic, Mildred S. Dresselhaus, and Jing Kong. Large Area, Few-Layer Graphene Films on Arbitrary Substrates by Chemical Vapor Deposition. *Nano Letters*, 9(1):30–35, January 2009.

[54] Junmo Kang, Soonhwi Hwang, Jae Hwan Kim, Min Hyeok Kim, Jaechul Ryu, Sang Jae Seo, Byung Hee Hong, Moon Ki Kim, and Jae-Boong Choi. Efficient Transfer of Large-Area Graphene Films onto Rigid Substrates by Hot Pressing. *ACS Nano*, 6(6):5360–5365, June 2012.

[55] Xuesong Li, Yanwu Zhu, Weiwei Cai, Mark Borysiak, Boyang Han, David Chen, Richard D. Piner, Luigi Colombo, and Rodney S. Ruoff. Transfer of Large-Area Graphene Films for High-Performance Transparent Conductive Electrodes. *Nano Letters*, 9(12):4359–4363, December 2009.

[56] Yaping Dan, Ye Lu, Nicholas J. Kybert, Zhengtang Luo, and A. T. Charlie Johnson. Intrinsic Response of Graphene Vapor Sensors. *Nano Letters*, 9(4):1472–1475, April 2009.

[57] Silvan Roth, Fumihiko Matsui, Thomas Greber, and Jürg Osterwalder. Chemical Vapor Deposition and Characterization of Aligned and Incommensurate Graphene/Hexagonal Boron Nitride Heterostack on Cu(111). *Nano Letters*, 13(6):2668–2675, June 2013.

[58] Yumeng Shi, Wu Zhou, Ang-Yu Lu, Wenjing Fang, Yi-Hsien Lee, Allen Long Hsu, Soo Min Kim, Ki Kang Kim, Hui Ying Yang, Lain-Jong Li, Juan-Carlos Idrobo, and Jing Kong. van der Waals Epitaxy of MoS_2 Layers Using Graphene As Growth Templates. *Nano Letters*, 12(6):2784–2791, June 2012.

[59] Wei Yang, Guorui Chen, Zhiwen Shi, Cheng-Cheng Liu, Lianchang Zhang, Guibai Xie, Meng Cheng, Duoming Wang, Rong Yang, Dongxia Shi, Kenji Watanabe, Takashi Taniguchi, Yugui Yao, Yuanbo Zhang, and Guangyu Zhang. Epitaxial growth of single-domain graphene on hexagonal boron nitride. *Nature Materials*, 12(9):792–797, September 2013.

[60] Zheng Liu, Li Song, Shizhen Zhao, Jiaqi Huang, Lulu Ma, Jiangnan Zhang, Jun Lou, and Pulickel M. Ajayan. Direct Growth of Graphene/Hexagonal Boron Nitride Stacked Layers. *Nano Letters*, 11(5):2032–2037, May 2011.

[61] Shonali Dhingra, Jen-Feng Hsu, Ivan Vlassiouk, and Brian D'Urso. Chemical vapor deposition of graphene on large-domain ultra-flat copper. *Carbon*, 69:188–193, April 2014.

[62] Ivan Vlassiouk, Murari Regmi, Pasquale Fulvio, Sheng Dai, Panos Datskos, Gyula Eres, and Sergei Smirnov. Role of Hydrogen in Chemical Vapor Deposition Growth of Large Single-Crystal Graphene. *ACS Nano*, 5(7):6069–6076, July 2011.

[63] E. Bauer. Low energy electron microscopy. *Reports on Progress in Physics*, 57(9):895–938, September 1994.

[64] James B. Hannon and Rudolf M. Tromp. Low-energy electron microscopy for nanoscale characterization. In *Handbook of Instrumentation and Techniques for Semiconductor Nanostructure Characterization*, volume Volume 1 & 2 of *Materials and Energy*, pages 127–181. World Scientific Publishing Company, November 2011.

[65] P. C. Mende, Q. Gao, A. Ismach, H. Chou, M. Widom, R. Ruoff, L. Colombo, and R. M. Feenstra. Characterization of hexagonal boron nitride layers on nickel surfaces by low-energy electron microscopy. *Surface Science*, 659:31–42, May 2017.

[66] Patrick C. Mende, Jun Li, and Randall M. Feenstra. Substitutional mechanism for growth of hexagonal boron nitride on epitaxial graphene. *Applied Physics Letters*, 113(3):031605, July 2018.

[67] R. M. Feenstra, N. Srivastava, Qin Gao, M. Widom, Bogdan Diaconescu, Taisuke Ohta, G. L. Kellogg, J. T. Robinson, and I. V. Vlassiouk. Low-energy electron reflectivity from graphene. *Physical Review B*, 87(4):041406, January 2013.

[68] N. Srivastava, Qin Gao, M. Widom, R. M. Feenstra, Shu Nie, K. F. McCarty, and I. V. Vlassiouk. Low-energy electron reflectivity of graphene on copper and other substrates. *Physical Review B*, 87(24):245414, June 2013.

[69] H. Hibino, H. Kageshima, F. Maeda, M. Nagase, Y. Kobayashi, and H. Yamaguchi. Microscopic thickness determination of thin graphite films formed on SiC from quantized oscillation in reflectivity of low-energy electrons. *Physical Review B*, 77(7):075413, February 2008.

[70] Y. Qi, S. H. Rhim, G. F. Sun, M. Weinert, and L. Li. Epitaxial Graphene on SiC(0001): More than Just Honeycombs. *Physical Review Letters*, 105(8):085502, August 2010.

[71] Shu Nie, Wei Wu, Shirui Xing, Qingkai Yu, Jiming Bao, Shin-shem Pei, and Kevin F. McCarty. Growth from below: bilayer graphene on copper by chemical vapor deposition. *New Journal of Physics*, 14(9):093028, September 2012.

[72] W. Świch, B. Rausenberger, W. Engel, A. M. Bradshaw, and E. Zeitler. In-situ studies of heterogeneous reactions using mirror electron microscopy. *Surface Science*, 294(3):297–307, September 1993.

[73] Lloyd M. Davis, Noel C. MacDonald, Paul W. Palmberg, Gerald Edward Riach, and Richard E. Weber. Handbook of Auger Electron Spectroscopy. 1976.

[74] Piran R. Kidambi, Raoul Blume, Jens Kling, Jakob B. Wagner, Carsten Baehtz, Robert S. Weatherup, Robert Schloegl, Bernhard C. Bayer, and Stephan Hofmann. In Situ Observations during Chemical Vapor Deposition of Hexagonal Boron Nitride on Polycrystalline Copper. *Chemistry of Materials*, 26(22):6380–6392, November 2014.

[75] Yi Zhang, Zhen Li, Pyojae Kim, Luyao Zhang, and Chongwu Zhou. Anisotropic Hydrogen Etching of Chemical Vapor Deposited Graphene. *ACS Nano*, 6(1):126–132, January 2012.

[76] Liang Zhang, Yifan Ye, Dingling Cheng, Haibin Pan, and Junfa Zhu. Intercalation of Li at the Graphene/Cu Interface. *The Journal of Physical Chemistry C*, 117(18):9259–9265, May 2013.

[77] Meryl D. Stoller, Sungjin Park, Yanwu Zhu, Jinho An, and Rodney S. Ruoff. Graphene-Based Ultracapacitors. *Nano Letters*, 8(10):3498–3502, October 2008.

[78] Takashi Ikeda, Zhufeng Hou, Guo-Liang Chai, and Kiyoyuki Terakura. Possible Oxygen Reduction Reactions for Graphene Edges from First Principles. *The Journal of Physical Chemistry C*, 118(31):17616–17625, August 2014.

[79] Donghui Guo, Riku Shibuya, Chisato Akiba, Shunsuke Saji, Takahiro Kondo, and Junji Nakamura. Active sites of nitrogen-doped carbon materials for oxygen reduction reaction clarified using model catalysts. *Science*, 351(6271):361–365, January 2016.

[80] Qiyuan He, Shixin Wu, Zongyou Yin, and Hua Zhang. Graphene-based electronic sensors. *Chemical Science*, 3(6):1764–1772, May 2012.

[81] Zongping Chen, Wencai Ren, Libo Gao, Bilu Liu, Songfeng Pei, and Hui-Ming Cheng. Three-dimensional flexible and conductive interconnected graphene networks grown by chemical vapour deposition. *Nature Materials*, 10(6):424–428, June 2011.

[82] Mineo Hiramatsu and Masaru Hori. Future Perspective for Emerging Applications Using Carbon Nanowalls. In Mineo Hiramatsu and Masaru Hori, editors, *Carbon Nanowalls: Synthesis and Emerging Applications*, pages 159–161. Springer Vienna, Vienna, 2010.

[83] Raghav Garg, Sahil K. Rastogi, Michael Lamparski, Sergio C. de la Barrera, Gordon T. Pace, Noel T. Nuhfer, Benjamin M. Hunt, Vincent Meunier, and Tzahi Cohen-Karni. Nanowire-Mesh-Templated Growth of Out-of-Plane Three-Dimensional Fuzzy Graphene. *ACS Nano*, 11(6):6301–6311, June 2017.

[84] Pascal Ruffieux, Jinming Cai, Nicholas C. Plumb, Luc Patthey, Deborah Prezzi, Andrea Ferretti, Elisa Molinari, Xinliang Feng, Klaus Müllen, Carlo A. Pignedoli, and Roman Fasel. Electronic Structure of Atomically Precise Graphene Nanoribbons. *ACS Nano*, 6(8):6930–6935, August 2012.

[85] Young-Woo Son, Marvin L. Cohen, and Steven G. Louie. Half-metallic graphene nanoribbons. *Nature*, 444(7117):347–349, November 2006.

[86] Jian-Hao Chen, W. G. Cullen, C. Jang, M. S. Fuhrer, and E. D. Williams. Defect Scattering in Graphene. *Physical Review Letters*, 102(23):236805, June 2009.

[87] Oleg V. Yazyev and Yong P. Chen. Polycrystalline graphene and other two-dimensional materials. *Nature Nanotechnology*, 9(10):755–767, October 2014.

[88] Oleg V. Yazyev and Steven G. Louie. Electronic transport in polycrystalline graphene. *Nature Materials*, 9(10):806–809, October 2010.

[89] Adam W. Tsen, Lola Brown, Mark P. Levendorf, Fereshte Ghahari, Pinshane Y. Huang, Robin W. Havener, Carlos S. Ruiz-Vargas, David A. Muller, Philip Kim, and Jiwoong Park. Tailoring Electrical Transport Across Grain Boundaries in Polycrystalline Graphene. *Science*, 336(6085):1143–1146, June 2012.

[90] Mingyao Zhu, Jianjun Wang, Brian C. Holloway, R. A. Outlaw, Xin Zhao, Kun Hou, V. Shutthanandan, and Dennis M. Manos. A mechanism for carbon nanosheet formation. *Carbon*, 45(11):2229–2234, October 2007.

[91] Zheng Bo, Yong Yang, Junhong Chen, Kehan Yu, Jianhua Yan, and Kefa Cen. Plasma-enhanced chemical vapor deposition synthesis of vertically oriented graphene nanosheets. *Nanoscale*, 5(12):5180–5204, June 2013.

[92] I. L. Spain, K. J. Volin, H. A. Goldberg, and I. Kalnin. Electronic properties of pan-based carbon fibers—I: Experiment and comparison with properties of bulk carbons. *Journal of Physics and Chemistry of Solids*, 44(8):839–849, January 1983.

[93] D. H. Seo, S. Kumar, and K. Ostrikov. Control of morphology and electrical properties of self-organized graphenes in a plasma. *Carbon*, 49(13):4331–4339, November 2011.

[94] Rong Zhao, Meysam Ahktar, Adel Alruqi, Ruchira Dharmasena, Jacek B. Jasinski, Rukshan M. Thantirige, and Gamini U. Sumanasekera. Electrical transport properties of graphene nanowalls grown at low temperature using plasma enhanced chemical vapor deposition. *Materials Research Express*, 4(5):055007, May 2017.

[95] Melinda Y. Han, Juliana C. Brant, and Philip Kim. Electron Transport in Disordered Graphene Nanoribbons. *Physical Review Letters*, 104(5):056801, February 2010.

[96] N. F. Mott. Conduction in non-crystalline materials. *The Philosophical Magazine: A Journal of Theoretical Experimental and Applied Physics*, 19(160):835–852, April 1969.

[97] Yung-Lung Huang, Shao-Pin Chiu, Zhi-Xin Zhu, Zhi-Qing Li, and Juhn-Jong Lin. Variable-range-hopping conduction processes in oxygen deficient polycrystalline ZnO films. *Journal of Applied Physics*, 107(6):063715, March 2010.

[98] L. B. Ioffe and B. Z. Spivak. Giant magnetoresistance in the variable-range hopping regime. *Journal of Experimental and Theoretical Physics*, 117(3):551–569, September 2013.

[99] I. Shlimak, E. Zion, A. V. Butenko, L. Wolfson, V. Richter, Yu. Kaganovskii, A. Sharoni, A. Haran, D. Naveh, E. Kogan, and M. Kaveh. Hopping magnetoresistance in ion irradiated monolayer graphene. *Physica E: Low-dimensional Systems and Nanostructures*, 76:158–163, February 2016.

[100] Zengji Yue, Igor Levchenko, Shailesh Kumar, Donghan Seo, Xiaolin Wang, Shixue Dou, and Kostya (Ken) Ostrikov. Large networks of vertical multi-layer graphenes with morphology-tunable magnetoresistance. *Nanoscale*, 5(19):9283–9288, September 2013.

[101] Y. Hishiyama, H. Irumano, Y. Kaburagi, and Y. Soneda. Structure, Raman scattering, and transport properties of boron-doped graphite. *Physical Review B*, 63(24):245406, May 2001.

[102] Yang-Bo Zhou, Bing-Hong Han, Zhi-Min Liao, Han-Chun Wu, and Da-Peng Yu. From positive to negative magnetoresistance in graphene with increasing disorder. *Applied Physics Letters*, 98(22):222502, May 2011.

[103] Wei Han, Roland K. Kawakami, Martin Gmitra, and Jaroslav Fabian. Graphene spintronics. *Nature Nanotechnology*, 9(10):794–807, October 2014.

[104] Zhenhua Qiao, Shengyuan A. Yang, Wanxiang Feng, Wang-Kong Tse, Jun Ding, Yugui Yao, Jian Wang, and Qian Niu. Quantum anomalous Hall effect in graphene from Rashba and exchange effects. *Physical Review B*, 82(16):161414, October 2010.

[105] Seongshik Oh. The Complete Quantum Hall Trio. *Science*, 340(6129):153–154, April 2013.

[106] Cui-Zu Chang, Jinsong Zhang, Xiao Feng, Jie Shen, Zuocheng Zhang, Minghua Guo, Kang Li, Yunbo Ou, Pang Wei, Li-Li Wang, Zhong-Qing Ji, Yang Feng, Shuaihua Ji, Xi Chen, Jinfeng Jia, Xi Dai, Zhong Fang, Shou-Cheng Zhang, Ke He, Yayu Wang, Li Lu, Xu-Cun Ma, and Qi-Kun Xue. Experimental Observation of the Quantum Anomalous Hall Effect in a Magnetic Topological Insulator. *Science*, 340(6129):167–170, April 2013.

[107] Cui-Zu Chang, Weiwei Zhao, Duk Y. Kim, Haijun Zhang, Badih A. Assaf, Don Heiman, Shou-Cheng Zhang, Chaoxing Liu, Moses H. W. Chan, and Jagadeesh S. Moodera. High-precision realization of robust quantum anomalous Hall state in a hard ferromagnetic topological insulator. *Nature Materials*, 14(5):473–477, May 2015.

[108] C. L. Kane and E. J. Mele. Quantum Spin Hall Effect in Graphene. *Physical Review Letters*, 95(22):226801, November 2005.

[109] Jiayong Zhang, Bao Zhao, Yugui Yao, and Zhongqin Yang. Robust quantum anomalous Hall effect in graphene-based van der Waals heterostructures. *Physical Review B*, 92(16):165418, October 2015.

[110] Zhenhua Qiao, Wei Ren, Hua Chen, L. Bellaiche, Zhenyu Zhang, A.H. MacDonald, and Qian Niu. Quantum Anomalous Hall Effect in Graphene Proximity Coupled to an Antiferromagnetic Insulator. *Physical Review Letters*, 112(11):116404, March 2014.

[111] Jiayong Zhang, Bao Zhao, Yugui Yao, and Zhongqin Yang. Quantum Anomalous Hall Effect in Graphene-based Heterostructure. *Scientific Reports*, 5:10629, May 2015.

[112] D. A. Abanin, S. V. Morozov, L. A. Ponomarenko, R. V. Gorbachev, A. S. Mayorov, M. I. Katsnelson, K. Watanabe, T. Taniguchi, K. S. Novoselov, L. S. Levitov, and A. K. Geim. Giant Nonlocality Near the Dirac Point in Graphene. *Science*, 332(6027):328–330, April 2011.

[113] Alexei Kitaev. Anyons in an exactly solved model and beyond. *Annals of Physics*, 321(1):2–111, January 2006.

[114] Arnab Banerjee, Jiaqiang Yan, Johannes Knolle, Craig A. Bridges, Matthew B. Stone, Mark D. Lumsden, David G. Mandrus, David A. Tennant, Roderich Moessner, and Stephen E. Nagler. Neutron scattering in the proximate quantum spin liquid α-$RuCl_3$. *Science*, 356(6342):1055–1059, June 2017.

[115] Luke J. Sandilands, Yao Tian, Kemp W. Plumb, Young-June Kim, and Kenneth S. Burch. Scattering Continuum and Possible Fractionalized Excitations in α-$RuCl_3$. *Physical Review Letters*, 114(14):147201, April 2015.

[116] S.-H. Do K.-Y. Choi Y.S. Kwon A.U.B. Wolter S. Nishimoto Jeroen van den Brink Baek, S.-H. and B. Büchner. Evidence for a Field-Induced Quantum Spin Liquid in α-$RuCl_3$. *Physical Review Letters*, 119(3), 2017.

[117] Soudabeh Mashhadi, Youngwook Kim, Jeongwoo Kim, Daniel Weber, Takashi Taniguchi, Kenji Watanabe, Noejung Park, Bettina Lotsch, Jurgen H. Smet, Marko Burghard, and Klaus Kern. Spin-Split Band Hybridization in Graphene Proximitized with α-$RuCl_3$ Nanosheets. *Nano Letters*, 19(7):4659–4665, July 2019.

[118] Boyi Zhou, J. Balgley, P. Lampen-Kelley, J.-Q. Yan, D. G. Mandrus, and E. A. Henriksen. Gate-tuned charge-doping and magnetism in graphene/α-$RuCl_3$ heterostructures. *arXiv:1811.04838 [cond-mat]*, November 2018. arXiv: 1811.04838.

[119] Dmitry Shcherbakov, Petr Stepanov, Daniel Weber, Yaxian Wang, Jin Hu, Yanglin Zhu, Kenji Watanabe, Takashi Taniguchi, Zhiqiang Mao, Wolfgang Windl, Joshua Goldberger, Marc Bockrath, and Chun Ning Lau. Raman Spectroscopy, Photocatalytic Degradation, and Stabilization of Atomically Thin Chromium Tri-iodide. *Nano Letters*, 18(7):4214–4219, July 2018.

[120] P. Blake, E. W. Hill, A. H. Castro Neto, K. S. Novoselov, D. Jiang, R. Yang, T. J. Booth, and A. K. Geim. Making graphene visible. *Applied Physics Letters*, 91(6):063124, August 2007.

[121] L. Wang, I. Meric, P. Y. Huang, Q. Gao, Y. Gao, H. Tran, T. Taniguchi, K. Watanabe, L. M. Campos, D. A. Muller, J. Guo, P. Kim, J. Hone, K. L. Shepard, and C. R. Dean. One-Dimensional Electrical Contact to a Two-Dimensional Material. *Science*, 342(6158):614–617, November 2013.

[122] Niclas Lindvall, Alexey Kalabukhov, and August Yurgens. Cleaning graphene using atomic force microscope. *Journal of Applied Physics*, 111(6):064904, March 2012.

[123] K. S. Novoselov, E. McCann, S. V. Morozov, V. I. Fal'ko, M. I. Katsnelson, U. Zeitler, D. Jiang, F. Schedin, and A. K. Geim. Unconventional quantum Hall effect and Berry's phase of 2π in bilayer graphene. *Nature Physics*, 2(3):177–180, March 2006.

[124] A. F. Young, C. R. Dean, L. Wang, H. Ren, P. Cadden-Zimansky, K. Watanabe, T. Taniguchi, J. Hone, K. L. Shepard, and P. Kim. Spin and valley quantum Hall ferromagnetism in graphene. *Nature Physics*, 8(7):550–556, July 2012.

[125] Mengqiao Sui, Guorui Chen, Liguo Ma, Wen-Yu Shan, Dai Tian, Kenji Watanabe, Takashi Taniguchi, Xiaofeng Jin, Wang Yao, Di Xiao, and Yuanbo Zhang. Gate-tunable topological valley transport in bilayer graphene. *Nature Physics*, 11(12):1027–1031, December 2015.

[126] Katsuaki Sato. Measurement of Magneto-Optical Kerr Effect Using Piezo-Birefringent Modulator. *Japanese Journal of Applied Physics*, 20(12):2403, December 1981.

[127] Jian-Hao Chen, Chaun Jang, Shudong Xiao, Masa Ishigami, and Michael S. Fuhrer. Intrinsic and extrinsic performance limits of graphene devices on SiO_2. *Nature Nanotechnology*, 3(4):206–209, April 2008.

[128] Yukio Suezaki and Hazime Mori. Dynamic Critical Phenomena in Magnetic Systems. II Electrical Resistivity near the Néel Point. *Progress of Theoretical Physics*, 41(5):1177–1189, May 1969.

[129] S. Alexander, J. S. Helman, and I. Balberg. Critical behavior of the electrical resistivity in magnetic systems. *Physical Review B*, 13(1):304–315, January 1976.

[130] Ö. Rapp, G. Benediktsson, H. U. Åström, S. Arajs, and K. V. Rao. Electrical resistivity of antiferromagnetic chromium near the Néel temperature. *Physical Review B*, 18(7):3665–3673, October 1978.

[131] Dennis Wang. *Optical and Electronic Studies of Air-Sensitive van der Waals Materials Encapsulated by Hexagonal Boron Nitride*. PhD thesis, Columbia University, 2018.

[132] Evan J. Telford, Avishai Benyamini, Daniel Rhodes, Da Wang, Younghun Jung, Amirali Zangiabadi, Kenji Watanabe, Takashi Taniguchi, Shuang Jia, Katayun Barmak, Abhay N. Pasupathy, Cory R. Dean, and James Hone. Via Method for Lithography Free Contact and Preservation of 2d Materials. *Nano Letters*, 18(2):1416–1420, February 2018.

[133] Zhe Wang, Ignacio Gutiérrez-Lezama, Nicolas Ubrig, Martin Kroner, Marco Gibertini, Takashi Taniguchi, Kenji Watanabe, Ataç Imamoğlu, Enrico Giannini, and Alberto F. Morpurgo. Very large tunneling magnetoresistance in layered magnetic semiconductor CrI 3. *Nature Communications*, 9(1):1–8, June 2018.

[134] Tiancheng Song, Xinghan Cai, Matisse Wei-Yuan Tu, Xiaoou Zhang, Bevin Huang, Nathan P. Wilson, Kyle L. Seyler, Lin Zhu, Takashi Taniguchi, Kenji Watanabe, Michael A. McGuire, David H. Cobden, Di Xiao, Wang Yao, and Xiaodong Xu. Giant tunneling magnetoresistance in spin-filter van der Waals heterostructures. *Science*, 360(6394):1214–1218, June 2018.

[135] D. R. Klein, D. MacNeill, J. L. Lado, D. Soriano, E. Navarro-Moratalla, K. Watanabe, T. Taniguchi, S. Manni, P. Canfield, J. Fernández-Rossier, and P. Jarillo-Herrero. Probing magnetism in 2D van der Waals crystalline insulators via electron tunneling. *Science*, 360(6394):1218–1222, June 2018.

[136] Hyun Ho Kim, Bowen Yang, Tarun Patel, Francois Sfigakis, Chenghe Li, Shangjie Tian, Hechang Lei, and Adam W. Tsen. One Million Percent Tunnel Magnetoresistance in a Magnetic van der Waals Heterostructure. *Nano Letters*, 18(8):4885–4890, August 2018.

[137] Matthew Yankowitz, Jeil Jung, Evan Laksono, Nicolas Leconte, Bheema L. Chittari, K. Watanabe, T. Taniguchi, Shaffique Adam, David Graf, and Cory R. Dean. Dynamic band-structure tuning of graphene moiré superlattices with pressure. *Nature*, 557(7705):404–408, May 2018.

[138] Matthew Yankowitz, Shaowen Chen, Hryhoriy Polshyn, Yuxuan Zhang, K. Watanabe, T. Taniguchi, David Graf, Andrea F. Young, and Cory R. Dean. Tuning superconductivity in twisted bilayer graphene. *Science*, 363(6431):1059–1064, March 2019.

[139] Dante J. O'Hara, Tiancong Zhu, Amanda H. Trout, Adam S. Ahmed, Yunqiu Kelly Luo, Choong Hee Lee, Mark R. Brenner, Siddharth Rajan, Jay A. Gupta, David W. McComb, and Roland K. Kawakami. Room Temperature Intrinsic Ferromagnetism in Epitaxial Manganese Selenide Films in the Monolayer Limit. *Nano Letters*, 18(5):3125–3131, May 2018.